NAVAL POSTGRADUATE SCHOOL

MONTEREY, CALIFORNIA

DISSERTATION

OPTIMAL SENSOR-BASED MOTION PLANNING FOR AUTONOMOUS VEHICLE TEAMS

by

Sean P. Kragelund

March 2017

Dissertation Supervisor: Isaac I. Kaminer

Approved for public release. Distribution is unlimited.

Reissued 30 May 2017 with correction to student's affiliation on title page.

THIS PAGE INTENTIONALLY LEFT BLANK

REPORT DOCUMENTATION PAGE

Form Approved OMB No. 0704–0188

1. AGENCY USE ONLY *(Leave Blank)*	2. REPORT DATE	3. REPORT TYPE AND DATES COVERED
	March 2017	Dissertation 09-29-2009 to 03-31-2017

4. TITLE AND SUBTITLE

OPTIMAL SENSOR-BASED MOTION PLANNING FOR AUTONOMOUS VEHICLE TEAMS

5. FUNDING NUMBERS

6. AUTHOR(S)

Sean P. Kragelund

7. PERFORMING ORGANIZATION NAME(S) AND ADDRESS(ES)

Naval Postgraduate School
Monterey, CA 93943

8. PERFORMING ORGANIZATION REPORT NUMBER

9. SPONSORING / MONITORING AGENCY NAME(S) AND ADDRESS(ES)

Department of the Navy

10. SPONSORING / MONITORING AGENCY REPORT NUMBER

11. SUPPLEMENTARY NOTES

The views expressed in this document are those of the author and do not reflect the official policy or position of the Department of Defense or the U.S. Government. IRB Protocol Number: N/A.

12a. DISTRIBUTION / AVAILABILITY STATEMENT

Approved for public release. Distribution is unlimited.

12b. DISTRIBUTION CODE

13. ABSTRACT *(maximum 200 words)*

Autonomous vehicle teams have great potential in a wide range of maritime sensing applications, including mine countermeasures (MCM). A key enabler for successfully employing autonomous vehicles in MCM missions is motion planning, a collection of algorithms for designing trajectories that vehicles must follow. For maximum utility, these algorithms must consider the capabilities and limitations of each team member. At a minimum, they should incorporate dynamic and operational constraints to ensure trajectories are feasible. Another goal is maximizing sensor performance in the presence of uncertainty. Optimal control provides a useful framework for solving these types of motion planning problems with dynamic constraints and different performance objectives, but they usually require numerical solutions. Recent advances in numerical methods have produced a general mathematical and computational framework for numerically solving optimal control problems with parameter uncertainty—generalized optimal control (GenOC)—thus making it possible to numerically solve optimal search problems with multiple searcher, sensor, and target models.

In this dissertation, we use the GenOC framework to solve motion planning problems for different MCM search missions conducted by autonomous surface and underwater vehicles. Physics-based sonar detection models are developed for operationally relevant MCM sensors, and the resulting optimal search trajectories improve mine detection performance over conventional lawnmower survey patterns—especially under time or resource constraints. Simulation results highlight the flexibility of this approach for optimal motion planning and pre-mission analysis. Finally, a novel application of this framework is presented to address inverse problems relating search performance to sensor design, team composition, and mission planning for MCM CONOPS development.

14. SUBJECT TERMS

optimal control, optimal search, mine countermeasures, motion planning, autonomous vehicles, unmanned vehicles, unmanned surface vessel, autonomous underwater vehicle, sonar, detection models, mission planning

15. NUMBER OF PAGES 199

16. PRICE CODE

17. SECURITY CLASSIFICATION OF REPORT	18. SECURITY CLASSIFICATION OF THIS PAGE	19. SECURITY CLASSIFICATION OF ABSTRACT	20. LIMITATION OF ABSTRACT
Unclassified	Unclassified	Unclassified	UU

NSN 7540-01-280-5500

Standard Form 298 (Rev. 2–89)
Prescribed by ANSI Std. 239–18

THIS PAGE INTENTIONALLY LEFT BLANK

Approved for public release. Distribution is unlimited.

OPTIMAL SENSOR-BASED MOTION PLANNING FOR AUTONOMOUS VEHICLE TEAMS

Sean P. Kragelund, Civilian, Department of the Navy
B.S., Santa Clara University, 1995
M.S., University of Washington, 2002

Submitted in partial fulfillment of the
requirements for the degree of

DOCTOR OF PHILOSOPHY IN MECHANICAL ENGINEERING

from the

NAVAL POSTGRADUATE SCHOOL
March 2017

Approved by: Isaac I. Kaminer
Professor of Mechanical and Aerospace Engineering
Dissertation Supervisor and Committee Chair

I. Michael Ross
Distinguished Professor of
Mechanical and Aerospace
Engineering

Anthony J. Healey
Distinguished Professor of
Mechanical and Aerospace
Engineering

Xiaoping Yun
Distinguished Professor of
Electrical and Computer
Engineering

Vladimir N. Dobrokhodov
Research Associate Professor of
Mechanical and Aerospace
Engineering

Approved by: Garth V. Hobson
Chair, Department of Mechanical and Aerospace Engineering

Approved by: Douglas Moses
Vice Provost for Academic Affairs

THIS PAGE INTENTIONALLY LEFT BLANK

ABSTRACT

Autonomous vehicle teams have great potential in a wide range of maritime sensing applications, including mine countermeasures (MCM). A key enabler for successfully employing autonomous vehicles in MCM missions is motion planning, a collection of algorithms for designing trajectories that vehicles must follow. For maximum utility, these algorithms must consider the capabilities and limitations of each team member. At a minimum, they should incorporate dynamic and operational constraints to ensure trajectories are feasible. Another goal is maximizing sensor performance in the presence of uncertainty. Optimal control provides a useful framework for solving these types of motion planning problems with dynamic constraints and different performance objectives, but they usually require numerical solutions. Recent advances in numerical methods have produced a general mathematical and computational framework for numerically solving optimal control problems with parameter uncertainty—generalized optimal control (GenOC)—thus making it possible to numerically solve optimal search problems with multiple searcher, sensor, and target models.

In this dissertation, we use the GenOC framework to solve motion planning problems for different MCM search missions conducted by autonomous surface and underwater vehicles. Physics-based sonar detection models are developed for operationally relevant MCM sensors, and the resulting optimal search trajectories improve mine detection performance over conventional lawnmower survey patterns—especially under time or resource constraints. Simulation results highlight the flexibility of this approach for optimal motion planning and pre-mission analysis. Finally, a novel application of this framework is presented to address inverse problems relating search performance to sensor design, team composition, and mission planning for MCM CONOPS development.

THIS PAGE INTENTIONALLY LEFT BLANK

Table of Contents

List of Figures

List of Tables

THIS PAGE INTENTIONALLY LEFT BLANK

List of Acronyms and Abbreviations

AG	array gain
ATLAS	Autonomous Topographic Large Area Sonar
AUV	autonomous underwater vehicle
CASS	Comprehensive Acoustic System Simulation
CAVR	Center for Autonomous Vehicle Research
CONOPS	concept of operations
CW	continuous wave
DI	directivity index
DOF	degrees of freedom
DT	detection threshold
EOD	explosive ordnance disposal
EOM	equations of motion
ESPRESSO	Extensible Performance and Evaluation Suite for Sonar
FLS	forward-looking sonar
FM	frequency modulated
FOM	figure of merit
FOV	field of view
HPC	High Performance Computing
GenOC	generalized optimal control

GRAB	Gaussian Ray Bundle
IAMSAR	International Aeronautical and Maritime Search and Rescue
ISR	intelligence, surveillance, reconnaissance
MCM	mine countermeasures
MIO	maritime interdiction operations
MLO	mine-like object
MOS	model operating system
NATO	North Atlantic Treaty Organization
NURC	North Atlantic Treaty Organization (NATO) Undersea Research Centre
NOMBO	non-mine/mine-like bottom object
NPS	Naval Postgraduate School
OAML	Ocean and Atmospheric Master Library
ODE	ordinary differential equation
ONR	Office of Naval Research
PATHA	Planning Aid for Tasking Heterogeneous Assets
PDF	probability density function
PL	propagation loss
REMUS	Remote Environmental Monitoring UnitS
RHIB	rigid hull inflatable boat
RID	reacquire-identify
RMS	root mean square
ROC	receiver operating characteristics

SAR search and rescue

SAROPS Search and Rescue Optimal Planning System

SAS synthetic aperture sonar

SE signal excess

SL source level

SLURM Simple Linux Utility for Resource Management

SNR signal-to-noise ratio

SPOC Software for Parameter-uncertainty Optimal Control

SS-DTE Single Sortie Detect to Engage

SSS sidescan sonar

TDA tactical decision aid

TS target strength

UAV unmanned aerial vehicle

USCG U.S. Coast Guard

USN U.S. Navy

USV unmanned surface vessel

THIS PAGE INTENTIONALLY LEFT BLANK

Acknowledgments

First, I would like to thank the members of my dissertation committee. At numerous points along this journey, you provided me with needed encouragement, valuable advice, and the occasional urgent signature to help me reach the finish line. I have been consistently impressed by the depth and breadth of your expertise. I am especially grateful to Tony Healey, for giving me my start in this arena and always believing that I could reach this goal. To Isaac and Vlad, for suggesting new ideas whenever I reached a dead end, and for supporting me during crunch time. And to Mike and Xiaoping, for seeing my work through a different lens and providing valuable feedback that improved the final product.

Second, I am indebted to Claire Walton, whose software I relied on to solve the problems in this dissertation. She was always willing to explain the intricacies of a numerical method, help debug my shoddy code, or provide a handy script for plotting my results.

I am also grateful to everyone at the SMART Scholarship Program for funding this degree, and for being flexible through all of the twists and turns of my research. To Martin Renken at NUWC-Keyport, thank you for your mentorship and the philosophical conversations we've had over the years. I look forward to many interesting collaborations down the road.

I would also like to thank my colleagues at the Center for Autonomous Vehicle Research. To Doug and Noel, for giving me the time and space I needed to make progress on this dissertation, and for dragging me off to the Arctic Ocean or Florida Keys when I needed a break to play with robots. Knowing that you survived this ordeal yourselves gave me hope and allowed me to endure. And to Aurelio, for his support during long days and nights in the field, and his help fixing all of the things that break.

Finally, I wish to thank my wonderful family for all of their love, understanding, and encouragement. To my parents, Keith and Kathy Kragelund, for the sacrifices they made for my education, and for providing role models to look up to. To my in-laws, Maurice and Patricia Gillespie, for their incredible willingness to help—always—and for raising an amazing daughter. Most of all, I am thankful each day for Lynn, Ryan, Maura, and Liliana. You are the greatest joys in my life, and nothing makes me more proud than being your husband and father. I love you all. And I can't wait for what life brings next!

THIS PAGE INTENTIONALLY LEFT BLANK

CHAPTER 1:
Introduction

Over the last two decades, unmanned vehicle systems have grown steadily more capable, reliable, and ubiquitous. Most systems, however, are still designed to conduct specific mission sets in a particular domain, with capabilities largely dependent on sensor payloads. As system designers increasingly turn to commercial technologies and open architectures, it is easier than ever for robotic systems to inter-operate. As a result, multiple dissimilar vehicles can be combined into a collaborative team to overcome individual vehicle limitations and deliver advanced capabilities—even across operating domains. Autonomous vehicle teams have great potential in a wide range of scientific, commercial and defense applications, and they are especially well-suited for remote sensing in maritime domains.

To maximize the utility of a heterogeneous vehicle team for a given sensing mission, motion planning algorithms must consider the capabilities and limitations of each team member. At a minimum, they should incorporate dynamic and operational constraints to produce feasible trajectories. Optimization techniques can be used to allocate effort according to individual vehicles' sensor performance. Such techniques can produce motion plans which are superior to conventional "lawnmower" survey patterns, which may be sub-optimal for certain sensors and infeasible for under-actuated vehicles to follow exactly.

Autonomous systems must also operate with imperfect information about their environment. This is particularly true in the maritime domain, where sensor accuracy usually depends on acoustic conditions and vehicle motion is subject to unknown disturbances at the water surface. In underwater search applications, the ability to detect and localize a target with sonar is impacted by several factors including acoustic noise, ambiguous geometry, and aspect-dependence. Consequently, the performance of an autonomous system may depend greatly on its ability to cope with uncertainty. Motion planning algorithms which consider uncertainty, therefore, can increase a system's overall robustness.

Optimal control provides a useful mathematical framework for solving motion planning problems with nonlinear dynamic constraints and different performance criteria [1], [2], but these problems are extremely difficult to solve analytically. Pseudospectral computa-

tional methods are a powerful tool for solving these problems numerically [3], [4]. Recent developments in numerical methods have made it possible to explicitly incorporate parameter uncertainty into the objective function of an optimal control problem [5]–[10]. Moreover, these *generalized optimal control (GenOC) problems* can incorporate sensor performance models to produce optimal vehicle trajectories for a given sensor configuration. Researchers have successfully applied these methods to solve motion planning problems with complex, multi-agent interactions in a variety of scenarios including optimal search, path coverage, and force protection [11].

This dissertation employs the GenOC framework as a mission planning tool for different autonomous vehicles conducting sensing missions for mine countermeasures (MCM). In this chapter, we first describe the motivation for developing motion planning algorithms for heterogeneous autonomous vehicle teams. Next, we provide context for our technical approach by reviewing relevant literature in the areas of MCM, search theory and sensor modeling, coverage planning, and optimal control. Finally, we highlight specific contributions developed during our investigation.

1.1 Motivation

There are a number of complex sensing missions which could utilize autonomous vehicle teams to deliver a mix of different capabilities. RIVERWATCH, for example, is a riverine environmental monitoring system comprised of an unmanned surface vessel (USV) which can launch and recover an unmanned aerial vehicle (UAV) to provide far-field sensing and improve the USV's perceptual map of the environment for safe navigation [12]. Autonomous vehicle teams will play an even bigger role in missions and environments where safety is paramount. The U.S. Navy has embraced this vision, and has invested heavily in vehicle and sensor technologies for mine countermeasures (MCM). In general, MCM operations are conducted in a sequence of phases, each performed by various types of vehicles and sensors [13]. Presently, these assets require dedicated support from manned platforms, but a current thrust of naval research is aimed at enabling autonomous systems to support other unmanned vehicles during MCM operations [14]. Since 2012, the Office of Naval Research (ONR) has developed a concept of operations (CONOPS) for autonomous mine hunting called Single Sortie Detect to Engage (SS-DTE). Figure 1.1 provides an artist's rendering of this future system in action. Under the SS-DTE concept, a USV host will

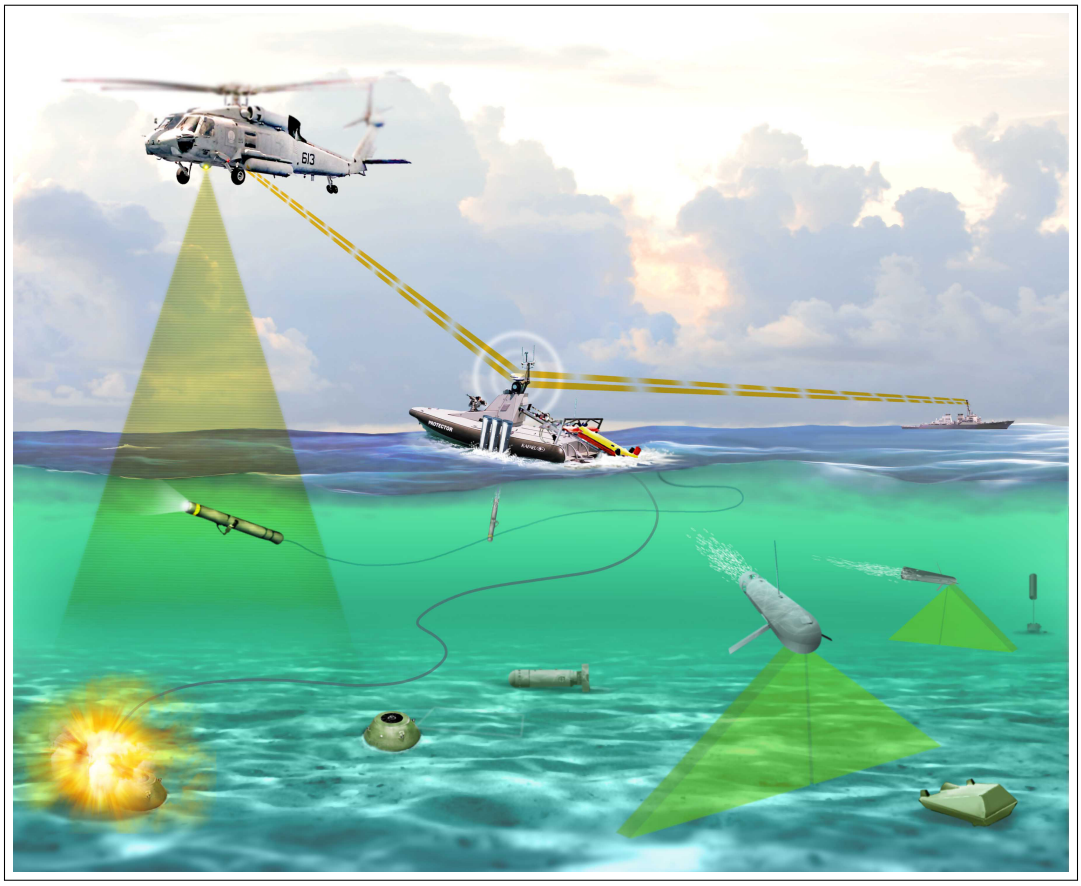

Figure 1.1. Concept for Single Sortie Detect to Engage for MCM operations. Source: [16].

deploy, recover, and sustain (i.e., recharge batteries, extract and process collected data, update mission objectives, etc.) multiple classes of autonomous underwater vehicles (AUVs) conducting different phases of a mine hunting operation [15].

Other concepts for using collaborative autonomous vehicles in MCM operations have been proposed. Researchers at the North Atlantic Treaty Organization (NATO) Undersea Research Centre (NURC), for example, have developed autonomous maneuvers for keeping a human-selected target in the sonar field of view of a USV to demonstrate a nascent target reacquisition behavior [17]. NURC researchers subsequently tested a concept whereby a highly capable USV detects and localizes a target in sonar imagery in order to guide an expendable neutralizer into the target [18]. The Naval Postgraduate School (NPS) Center

Figure 1.2. NPS CAVR Autonomous Surface and Underwater Vehicles.

for Autonomous Vehicle Research (CAVR) regularly deploys fleet-representative vehicles and sensors in support of naval research objectives. Figure 1.2 shows two such vehicles, a SeaFox USV and a Remote Environmental Monitoring UnitS (REMUS) 100 AUV in Monterey Harbor. Motivated by their untapped potential for collaboration in MCM sensing missions, this dissertation develops sensor-based motion planning strategies for a heterogeneous team comprised of these types of vehicles.

1.2 Background

Sensor-based motion planning means different things to different people. Choset and Burdick define this term as an algorithm that "incorporates sensor information, reflecting the current state of the environment, into a robot's planning process" [19]. The authors distinguish this approach from *classical planning*, which has the luxury of full knowledge about the world before planning begins. In this context, "sensor-based" can refer to any online planning algorithm. Another definition for *sensor planning*, or *sensor path planning* used in the literature "refers to the problem of determining a strategy for gathering sensor measurements to support a sensing objective" [20]–[22]. In this dissertation, we extend this definition to develop motion plans which explicitly optimize the performance

of a given sensor on a given platform for a given mission. This work is motivated by naval underwater MCM missions, which are fundamentally sensing problems conducted to detect and classify mine targets. In this context, sensor performance refers to the probability of detecting a target in the available mission time. An optimal motion plan maximizes this performance objective. We achieve this in our formulation by minimizing its complement, the probability of failing to detect a target.

1.2.1 Mine Countermeasures

Washburn and Kress describe three methods for clearing a minefield: destruction, hunting, and sweeping. Destruction refers to the application of "sufficient lethal force" to destroy all the mines in an area. The monetary cost and severe impact to the environment of this approach usually make destruction a method of last resort. Therefore, MCM operations traditionally comprise both mine hunting and minesweeping tasks. The authors provide the following definitions:

> One *sweeps* for mines by attempting to cause the mine's sensors to detonate the mine in circumstances where the detonation is harmless. If the mine is located by some means not involving its own sensors, and then either destroyed or avoided, one is instead *hunting* ... Sweeping and hunting are both essentially search problems. [23]

The U.S. Navy (USN)'s MCM capabilities and practices are summarized in *21st Century U.S. Navy Mine Warfare*, published by the Program Executive Office for Littoral and Mine Warfare. The authors state that since "minesweeping is more risky to the sweeping platform than mine hunting and, when completed, generally leaves behind a higher residual risk to vessels that transit the swept area" most MCM operational plans minimize risk by including both mine hunting and mine sweeping [24]. This dissertation considers only mine hunting operations, which are further described as follows:

> Mine hunting provides a relatively high degree of certainty that an area of concern is mine-free or the risk of a mine strike has been minimized. It comprises five steps: detection, classification, localization, identification, and neutralization. Sonars are the primary means to detect and classify mine-like contacts.

> Identifying each contact as a mine or a "NOMBO" (Non-Mine/Mine-Like Bottom Object) can also be carried out by EOD divers and the Navy's marine mammal systems, video cameras on mine neutralization vehicles, and laser systems. In this regard, advanced sonars on unmanned underwater vehicles offer good promise to enhance mine-hunting capabilities. [24]

Our approach concerns the latter, since the performance of mine hunting sonars are directly related to the capabilities of the vehicles that deploy them. Optimizing sensor performance through vehicle motion is the objective of this dissertation, hence the title: *Optimal Sensor-Based Motion Planning for Autonomous Vehicle Teams*. We do not address the neutralization task, but this is often considered a special case of an identification mission whereby an autonomous neutralizer vehicle reacquires (and destroys) a previously-identified target. Mine hunting operations face several challenges due to uncertainty, namely:

> A contact that is classified as mine-like must be identified as a mine or NOMBO and, if a mine, rendered safe before the Navy mine countermeasures commander . . . can declare a route or area cleared. Depending on the accuracy of the location of the contact, the characteristics of the bottom (e.g., smooth or rough), sediment type, amount of clutter, and the depth of the water, among other factors, the process of reacquisition and identification of each mine-like contact can take several hours. [24]

We note that while the SS-DTE concept "gets the man out of the minefield" by replacing manned AUV support vessels with a special-purpose USV, it otherwise follows the same operational paradigm employed today to carry out the five steps of detection, classification, localization, identification, and neutralization. This represents a bottleneck in MCM operations. In fact, a Naval Research Advisory Committee report from 2000 states:

> While time lines have shortened, current sensors require repeated acquisition of contacts to determine whether they are mine-like or NOMBOs to make positive identification . . . The critical issue here is that this process is presently done serially—one goes through the detection/classification processes by having to reacquire the detected objects in order to classify them, and to do so again if

> there is a decision to neutralize. This is not only very time consuming, but it also puts the MCM forces at risk, since little of the required action can be carried out clandestinely at present. [25]

Since the publication of this report, AUVs have improved the Navy's ability to conduct clandestine actions at greatly reduced risk to MCM personnel, but this serialized process is still time-consuming. We suggest that outfitting a host USV with wide-area mine detection sonar has potential to reduce current operational timelines by conducting the first four steps in parallel. This dissertation develops sensor-based motion planning strategies that investigate these new CONOPS.

Mine hunting tasks are often conducted in three distinct phases: 1) wide area detection and localization of mine-like objects (MLOs) with long-range, low-resolution sensors; 2) identification with short-range, high-resolution sensors; and 3) neutralization [26]. Phases one and two are increasingly conducted with autonomous vehicles, while phase three is still conducted primarily with explosive ordnance disposal (EOD) divers and/or remotely-operated vehicles. Therefore, in this dissertation, we focus on sensor-based motion planning for phases one and two. The literature provides examples of planning methods applicable to both phases. Phase one is typically treated as a coverage problem [26]–[28], especially when there is no prior information about mine locations. Large search areas are usually subdivided into smaller regions which can be covered by a typical AUV mission duration [27], or subdivided by bottom type [29], so that different sensors, track spacing, etc. can be tailored to the local environment. Several coverage path planning methods may be used, but vehicle paths for phase one are usually based on a deterministic coverage pattern like the popular lawnmower pattern.

Phase two can be thought of as a targeted coverage problem, guided by prior information about the expected target locations. When a vehicle must visit multiple MLOs during a reacquire-identify (RID) mission, this is akin to solving a traveling salesman problem [28] to visit each target location. Typically, a "standard" multiple aspect coverage pattern comprised of parallel tracks at different headings is then executed above each target. This method ensures that high-resolution imagery is collected from several different aspect angles in order to aid the identification effort. Often, the choice of sensor dictates the type of vehicle paths considered for RID missions. Sidescan sonar, for example, does not produce

good imagery when the search platform does not follow level, straight line paths. Therefore, these planning methods do not consider vehicle dynamics beyond speed, minimum turning radius and/or the time required to make a turn. Some methods account for the distance required to stabilize on the next track line after making a U-turn [30]. When planning lawnmower-type coverage patterns for sidescan sonar (SSS), some algorithms optimize over the space of track line headings [22], [31].

Johannsson et al. propose an algorithm for conducting both mine detection and RID missions from a single AUV [32]. The planning algorithm considers the benefit of altering the plan to inspect a detected object immediately, or postpone identification until later, i.e., if the current plan will already revisit the area where the detection occurred. This approach is an exception to the current MCM practice of conducting phase two tasks with different vehicles and sensors than the ones utilized for phase one.

The literature contains a few examples which conduct MCM tasks via heterogeneous vehicle teams. Sariel et al. proposes a multi-vehicle architecture in which AUVs detect MLOs and crawler robots revisit these locations to identify the targets with cameras. This implementation provides a mechanism for resource management; the available AUVs negotiate amongst themselves to select from all possible waypoint locations, effectively dividing the search area by construction of their search paths [33]. This example does not incorporate realistic vehicle dynamics or sensor models, however. Bays et al. describe an automated scheduling system for the Navy's SS-DTE program, which schedules a sequence of operations for the team to complete, including USV transit operations to rapidly carry AUVs to and from their search areas [34].

Shafer et al. describe a developmental system comprised of USVs and AUVs that can carry different sonar to cooperatively conduct phases one and two. The authors employ a behavior-based architecture that "performs multi-objective optimization to reconcile behavior output" from a set of desired behaviors [35]. In this approach, each vehicle stores a gridded representation of the environment. When a vehicle's sensor footprint passes over a cell, the "clearance level" for that cell is updated and communicated to the other vehicles in the team. In this manner, the authors successfully demonstrate various cooperative search strategies. We note that the ideas expressed by these authors are fundamentally similar to those presented in this dissertation. *The main distinction of our approach, therefore, is the*

direct optimization of sensor performance through vehicle motion, rather than maximizing sensor coverage through cooperative, emergent behaviors.

1.2.2 Search Theory

Search theory as a discipline in operations research grew out of work by the Antisubmarine Warfare Operations Research Group in World War II, first published by Koopman in 1946 [36] and reprinted in expanded form in 1980 [37]. These principles are still widely used today, and are the foundation for many practical search planning methods defined in the International Aeronautical and Maritime Search and Rescue (IAMSAR) manual, as well as computer-based methods like Search and Rescue Optimal Planning System (SAROPS) [38]. Many of these ideas have been summarized in a report developed for the search and rescue (SAR) community by [39]. Stone extended these concepts to address the optimal allocation of search effort in [40]. In [41], Stone lists three basic elements of an optimal search problem:

1. A probability distribution to quantify information about the target's location.
2. A detection function that relates search effort to the probability of detection.
3. Constraints on the search effort.

Chapter 3 of this dissertation formulates different MCM missions using various combinations of these elements. Stone illustrates the application of optimal search techniques for finding a drifting vessel lost at sea in [42], and this example problem has many of the hallmarks of MCM mission planning. Specifically, it involves sub-dividing a large search area into discrete cells, each with an assumed prior target distribution model, and specifying parallel search paths according to the sensor sweep width. Detection probability as a function of time (for random and ideal search strategies) and as a function of parallel path spacing are both presented. Although searching for stationary targets (e.g., mines) is simpler than searching for moving targets, MCM missions are complicated by sea floor characteristics and clutter which can appear as mines in sonar imagery.

Stone and Stanshine consider optimal search problems in the presence of these false targets in [43], with additional theorems and solution strategies presented in [40]. In short, this approach assumes that search is conducted in two phases: 1) *broad search* with a broad-search sensor to detect *contacts*, and 2) *contact investigation* by a sensor with a

much smaller sweep width to identify which contacts are actual targets. The question, then, is how to optimally allocate search effort between these two phases, depending on the *contact investigation policy*. Results are provided for *conclusive* contact investigation policies, which, once begun, must continue until a contact is identified as a true or false target. While searchers are not required to initiate a contact investigation upon each detection event, search strategies which implement so-called *immediate* contact investigation policies outperform those that delay this operation [40]. A recent example of this approach, applied to a military surveillance operation, utilizes a *verification team* to investigate contacts reported by an imperfect sensor in order to find a target in minimum time [44].

Stone's solution strategies for problems with false targets mirror MCM search and RID missions. We remark, however, that current operational practice does not conduct these missions concurrently. Nevertheless, Stone's results suggest that efficiencies can be realized by cooperative, heterogeneous vehicle teams that can implement immediate contact investigation. Since autonomous systems are reaching a level of maturity that makes such cooperation possible, this is an area worthy of future development. While this dissertation describes a method for generating optimal sensor-based search trajectories for a team of dissimilar vehicles and sensors, the method does not yet accommodate motion plans to conduct MCM search and RID missions *concurrently*. This capability would allow mission planners to address false targets through *immediate* contact investigation in the manner of [40]. At present, however, we operate under the prevailing operational assumption that separate RID missions are required to positively identify mine targets from a list of MLOs detected by an initial survey. We then utilize the GenOC solution framework to generate motion plans for both types of MCM missions.

The field of search theory is vast and continuously evolving. Benkoski provides a "comprehensive review of the existing published search theory literature," with specific applications divided according to "one-sided search" for non-evading targets, and "search games" whereby targets may work to thwart the search operation [45]. More recently, Chung et al. surveyed the results in this field with particular relevance to search operations by mobile robots. These authors generate a "partial taxonomy of the parameter space for search and pursuit-evasion models" [46]. This taxonomy includes branches for searcher, target, and environment models. The searcher branch incorporates models that quantify searcher motion, sensor detection, and the number and type of search agents available. The target

branch categorizes applications by the number and type of targets being hunted, whether targets are stationary or mobile, and if mobile, whether their motion is adversarial. Environmental models, meanwhile, are subdivided into continuous and discrete representations. Under this taxonomy, the search problems considered in this dissertation include:

- one or more heterogeneous vehicles and sensors, conducting a one-sided search for
- one or more stationary targets, with known or unknown (uniform) prior distributions,
- in continuous time and space.

Historically, these problems derive from Koopman's probabilistic search results and define measures of performance based on expected value [46]. This dissertation uses the same theoretical approach, developing an objective function in Chapter 3 to quantify the expected probability of failing to detect a target. Optimal search trajectories that minimize this objective function in continuous time and space can be generated via numerical approximation techniques in the GenOC framework. In fact, Stone et al. refer to "optimal search in continuous time and space subject to constraints" as *uncertain optimal control problems* [47]. *These techniques distinguish our approach from optimal search strategies which rely on discrete representations of the environment, searchers, and/or sensors.*

Hollinger et al. propose methods for distributed, multi-vehicle search planning that allow searchers to share and fuse data about a target's position and improve team performance [48], [49]. Realistic communications constraints are enforced by a physics-based model of the acoustic communications channel, but no motion constraints are imposed on searcher motion, detection is simulated by ideal sensor models, and search plans consist of transitions between discrete grid cells. Another information-based, discrete search formulation is presented by Baylog and Wettergren in [50]. The authors model the intake of sensor information during a search operation as an information flow through a communications channel. This approach replaces traditional sensor models with information measures that determine how much information can be gained from visiting discrete cells in the search space. The resulting optimal search plan comprises an optimal *cell visitation sequence*. While this framework can incorporate true target detections and false positives as a function of the channel characteristics in each cell, this approach does not address searcher dynamics.

1.2.3 Sensor Performance Modeling

Our definition for *sensor-based motion planning* requires a model of the sensor whose performance we seek to optimize. For underwater applications, sonar is the sensor of choice. The MCM missions discussed thus far employ several different types of sonar, and measures of performance might therefore depend upon a specific mission objective. Operators planning a wide area survey with a long-range sonar may be concerned only with *detecting* MLOs. Meanwhile, operators planning a RID mission with high-resolution SSS or multibeam sonar may be concerned only with achieving *complete coverage* of a designated area of the sea floor. Even though several algorithms have been proposed that guarantee complete coverage, this objective might not ensure *even* coverage, e.g., due to localized environmental conditions. Therefore, we seek an objective function that can be applied to different sensing objectives, yet still model realistic performance. In this dissertation, we address phase one and two MCM missions as optimal search problems, and these problems typically require some type of detection model. Therefore, we make the following assumptions with regard to mission performance:

1. Phase one succeeds if we detect a target with a long-range sensor.
2. Phase two succeeds if we detect a previously detected target with a high-resolution sensor.

Many of the detection models developed for search theory by Koopman [36] are still in wide use today. Washburn provides an excellent overview in [51], including models based on definite range, lateral range curves, and the inverse cube law, as well as detection rates based on "glimpses" with a physical sonar or radar model. The models derived in Chapter 2 of this disseration are based on signal excess and utilize the latter approach. Hansen provides a useful introduction to the principles of underwater sound for different sonar applications in [52]. This information is helpful in understanding the concept of signal excess. For the interested reader, a number of detailed texts on this subject are available, including [53]–[56], to name a few.

The sonar detection models developed in this dissertation were designed to rapidly calculate signal excess within a trajectory optimization routine, so complex environmental and reverberation effects are neglected. Other sonar performance models, including the U.S. Navy's Comprehensive Acoustic System Simulation (CASS), can model these effects via

different mathematical models tailored to a given operational environment. It has been used to analyze the effects of uncertain environmental data on mine detection performance [57], [58], but this model is too computationally-intensive for our application.

There are a number of existing sonar perfomance models to choose from (Etter lists twenty six! [56]), but many do not lend themselves to motion planning, particularly if environmental effects are desired. Once exception is Planning Aid for Tasking Heterogeneous Assets (PATHA), which uses Extensible Performance and Evaluation Suite for Sonar (ESPRESSO), NATO's standard minehunting sonar performance prediction tool. This planning tool optimally assigns vehicles to straight line track segments according to their sensing capabilities and the local sea floor characteristics [59]. PATHA estimates detection probabilities by generating lateral range curves for a given sonar, target, seabed type, and vehicle platform; it does not generate optimal trajectories for these vehicles to follow, but simply specifies a location for their desired track lines.

Finally, some applications analyze sonar performance based on the imagery they produce, and have developed models that simulate image construction by SSS and high-resolution forward-looking sonar (FLS) [60], including modern imaging sonars like the BlueView P900 FLS [61], [62]. These methods can be useful for simulating the performance of computer-aided detection and classification algorithms on synthetic sonar imagery, accelerating the development of new capabilities when actual sonar data is scarce.

1.2.4 Coverage

For many robotic sensing applications, the stated objective is complete coverage of an operating area with a sensor. A typical example is conducting a survey with an AUV to map a region of the sea floor with high-resolution sonar imagery. In this dissertation, however, the objective of sensor-based motion planning is to optimize the detection performance of a given sensor. The difference is nuanced, but implies that a sensor's performance can vary along a path that was designed to obtain complete coverage. This is realistic, as we know that factors like vehicle motion or localized environmental conditions at points along the robot's path can adversely impact its sensor performance.

Cai and Ferrari propose a *sensor planning* algorithm for classifying multiple fixed targets by strict placement of a robotic sensor. The algorithm explicitly accounts for sensor place-

ment by defining a subset of the robot's configuration space from which the sensor's field of view (FOV), rigidly attached to the robot, will intersect each target. It then uses an approximate cell-decomposition method to find a path that maximizes an information-theoretic metric. The proposed application is similar to an MCM RID mission: a ground robot is tasked with revisiting targets previously detected by an aircraft's infrared sensor, and deploying a ground penetrating radar to positively identify each target [20]. A weakness of this algorithm is that near-perfect information about the robot and its environment are required. While this situation might be possible for ground robots, it is certainly not the case for underwater vehicles. Nevertheless, this algorithm is representative of motion planning based on a sensor's FOV, or footprint; but not necessarily on its performance. The sonar detection models developed in this dissertation incorporate three-dimensional FOVs based on realistic sonar design criteria, however these FOV limits are reflected primarily through the sonar's detection performance.

Coverage planning is another method which has historically focused more on sensor placement than sensor performance. A number of coverage planning algorithms for robotics exist. In his survey of this literature, Choset describes "applications such as floor cleaning, lawn mowing, mine hunting, harvesting, painting, etc. [that] require a *coverage path planning algorithm*, which as its name suggests, specifically emphasizes the space swept out by the robot's sensor" [63]. Historically, coverage planners first decompose a two-dimensional planar region into cells which are easy to cover individually, then achieve provably complete coverage by planning a path that visits each region. A famous example of this approach is the boustrophodon exact cellular decomposition by Choset and Pignon [64], which allows each cell to be covered by simple back-and-forth motions in an "ox-plowing" or lawnmower pattern. Latimer et al. have extended this approach to multiple vehicles [65]. Similar approaches have produced coverage path planners which optimize the robot's path length or minimize the number of turns, e.g., [66]. A recent survey of this literature in [67] reports on efforts to develop path planning approaches to cover three-dimensional surfaces such as urban structures and underwater bathymetry [68].

Coverage planning algorithms are used extensively to plan underwater surveys with imaging sonar. As Williams explains:

> The path-planning approach currently used in practice for underwater mine detection operations is to design a simple ladder survey with equidistant tracks over the mission area. The adherence to traversing *parallel* tracks in MCM operations is partly because the collected raw data is subsequently processed into imagery (e.g., synthetic aperture sonar (SAS) imagery), for which such data is preferable. Thus, the crux of the path-planning task becomes how to design the spacing of (parallel) tracks. [69]

Conceding that parallel survey tracks are often required to satisfy sonar imagery requirements, Williams stresses that historical coverage planning algorithms which produce *equal* track spacing are sub-optimal for MCM operations. Specifically, they do not account for sensor performance along a given track line. Mine detection performance is usually a function of highlight-to-shadow patterns in sonar images that indicate an object proud of the sea floor. As these patterns depend on range, geometry, and seabed type, Williams proposes an algorithm to determine the optimal track spacing based on these characteristics, in conjunction with SAS data. The algorithm outperforms uniform spacing, as measured by the proportion of search area with detection probability above a given threshold [69].

Paull et al. develop *sensor-driven* online coverage algorithms designed to optimize the information collected by a sensor. These algorithms utilize information gain from sidescan sonar, modeled by classification confidence [21] or detection probability [22] (both obtained from lateral range curves of the environment computed by ESPRESSO). While these algorithms incorporate sonar performance data in the manner of [69], they have the added advantage of adapting their patterns to align survey tracks on headings which maximize their objective function. Planning is accomplished on a discrete hexagonal decomposition. Another multi-objective coverage planning method which accounts for sensor detection performance via lateral range curves is described by Abreu and Matos [26]. The authors claim that this approach, which uses evolutionary algorithms to optimize the AUV's survey path, obtains higher detection probabilities than the optimal track spacing algorithm suggested by [69].

Yetkin et al. propose a method for estimating the number of targets in each cell of a discrete grid. This algorithm assumes that probabilistic sensor performance corresponds to the environment in each cell, and these environments are drawn stochastically from a finite set of possible environments. The authors propose a "decision-theoretic cost function for realistic search problems that include the effects of false alarms, missed detections, uncertainty in the environment, and any prior information" about the number of objects at a location [70]. As with the other algorithms described above, sidescan sonar motion constraints are imposed, so this algorithm determines the best rows to traverse in the time available. After sampling the first cell in its current plan, it adaptively plans the first N steps of a new optimal path in a receding horizon fashion. Simulations reveal that this adaptive approach outperforms a traditional lawnmower pattern. While no other MCM planning or coverage method I encountered in the literature incorporated all of these factors on search performance, the current implementation of this approach lacks realistic sensor models and vehicle dynamics.

All of these approaches implement an exhaustive area coverage pattern by a set of straight-line survey tracks. In de-mining applications, Acar et al. observe that "exhaustive coverage is the best strategy when the robot has unlimited time (less than what is required by a random strategy) and no a priori information" [71]. When time or resource constraints prevent complete coverage, however, these authors recommend a probabilistic planning method to discover and/or exploit any prior information about the minefield itself. The rationale for this approach is that minefields typically have a regular pattern arising from traditional mine-laying methods. Once this pattern is discovered, a robot can conduct an opportunistic search of expected mine locations. Kim and Healey reach a similar conclusion in [72], and provide detailed simulation results comparing random and deterministic search strategies for mine clearance operations by robots with different capabilities.

While the sensor-based motion planning algorithm in this dissertation has commonalities with coverage planning methods that attempt to maximize sonar performance, our approach does not rely on straight-line survey tracks. Indeed, the GenOC framework can accommodate complete six-degrees of freedom (DOF) models of search vehicle dynamics to generate feasible vehicle trajectories that optimize detection performance.

1.2.5 Motion Planning via Optimal Control

LaValle states that "a fundamental need in robotics is to have algorithms that convert high-level specifications of tasks from humans into low-level descriptions of how to move. The terms motion planning and trajectory planning are often used for these kinds of problems" [73]. Under this broad definition, the field of robot motion planning encompasses a number of widely different applications. Like search theory, the literature dedicated to this field is already immense. Unlike search theory, however, this field is growing at an exponentially faster rate. Many texts like [73] provide a good introductory overview of this subject, so we restrict our discussion to motion planning algorithms based on optimal control.

Hurni presents useful definitions that help distinguish between path planning, motion planning, and trajectory planning in [74]. Under these definitions, *path planning* finds feasible paths from one robot configuration to another; *motion planning* computes these paths, parameterized by time; and *trajectory planning* calculates the complete evolution of a robot's state and actuator control variables as a function of time. Therefore, the techniques described in this dissertation implement trajectory planning; they generate vehicle state and control trajectories that optimize a search objective. However, we continue to refer to the outputs of this process as motion plans in the context of MCM mission planning.

Hurni also compares several path/trajectory planning methods applied to the solution of a benchmark obstacle avoidance problem. Multiple bug algorithms are implemented, in addition to various artificial potential field, roadmap, cellular decomposition, and optimal control-based planning methods. When evaluated against several criteria including optimality, feasibility, computational complexity, and portability, Hurni suggests that optimal control trajectory planning methods (solved via numeric optimization) outperform all other methods tested against his benchmark problem [74].

A standard optimal control problem seeks a control trajectory $\vec{u}(t)$ that forces a dynamic system $\dot{\vec{x}}(t) = \vec{f}\left(\vec{x}(t),\vec{u}(t),t\right)$ from its initial state $\vec{x}(t_0) = \vec{x}_0$ to a desired final state $\vec{x}(t_f) = \vec{x}_f$ while minimizing some cost functional. A Bolza cost functional $J[\vec{x}(\cdot),\vec{u}(\cdot),t_0,t_f]$ comprises an end-point cost $E\left(\vec{x}(t_0),\vec{x}(t_f),t_0,t_f\right)$ and a running cost $R\left(\vec{x}(t),\vec{u}(t),t\right)$ accumulated over the time domain $t \in [t_0,t_f]$. In its most general form, this problem is [75]:

Standard Optimal Control Problem

$$
\begin{aligned}
\underset{\vec{u}(t)}{\text{minimize}} \qquad & J[\vec{x}(\cdot),\vec{u}(\cdot),t_0,t_f] = E\left(\vec{x}(t_0),\vec{x}(t_f),t_0,t_f\right) + \int_{t_0}^{t_f} R\left(\vec{x}(\tau),\vec{u}(\tau),\tau\right) \\
& \vec{f}\left(\vec{x}(t),\vec{u}(t),t\right) = \dot{\vec{x}}(t) \quad \text{(the state dynamics)} \\
\text{subject to} \qquad & \vec{e}\left(\vec{x}(t_0),\vec{x}(t_f),t_0,t_f\right) = \vec{0} \quad \text{(the end-point conditions)} \\
& \vec{h}\left(\vec{x}(t),\vec{u}(t)\right) \leq \vec{0} \quad \text{(the state-control path constraints)}
\end{aligned} \tag{1.1}
$$

For all but the simplest optimal control problems, solutions must be obtained by computational methods. "Pseudospectral optimal control theory, a term coined by Ross, is a joint theoretical-computational framework" for solving constrained, nonlinear optimal control problems [4]. Ross and Karpenko review the theoretical foundations for this framework, discuss the ramifications for selecting a pseudospectral method, and describe practical implementations which utilize this approach [4]. At its heart, this solution framework transforms an optimal control problem from the physical domain to a computational domain where it can be approximated by a grid of interpolation nodes (and weighting functions) that have been carefully selected for convergence. Additional theoretical results are provided in [3], [75]–[77].

Recent advances in numerical methods have made it possible to explicitly incorporate parameter uncertainty into the objective function of an optimal control problem. This situation arises when conducting an optimal search for stationary targets at unknown locations, or mobile targets whose motion can be conditionally-determined by an uncertain parameter. Foraker develops a framework for solving such problems in continuous time and space as "generalized optimal control problems," and proves that his proposed "discretization schemes are consistent approximations" to the original problem [78]. Foraker et al. expand upon these results in [6], [7]. The objective functional for this optimal search problem "involves an expectation of a Bolza-type cost functional over a space of stochastic parameters" $\vec{\omega} \in \Omega \subset \mathbb{R}^{N_\omega}$ described by the continuous probability density function (PDF) $\phi(\vec{\omega}) : \Omega \mapsto \mathbb{R}$. This yields the generalized optimal control (GenOC) problem [5]:

Generalized Optimal Control (GenOC) Problem

$$
\begin{aligned}
\underset{\vec{u}(t)}{\text{minimize}} \quad & J[\vec{x}(\cdot),\vec{u}(\cdot),T_f] = \int_{\Omega} E\left(\vec{x}(T_f),\vec{\omega}\right) + G\left(\int_0^{T_f} R\left(\vec{x}(\tau),\vec{u}(\tau),\tau,\vec{\omega}\right) d\tau\right)\phi(\vec{\omega})d\vec{\omega} \\
& \vec{f}\left(\vec{x}(t),\vec{u}(t)\right) = \dot{\vec{x}}(t) \qquad \text{(the state dynamics)} \\
\text{subject to} \quad & \vec{x}(0) - \vec{x}_0 = \vec{0} \qquad \text{(the initial condition)} \\
& \vec{h}\left(\vec{u}(t)\right) \leq \vec{0} \qquad \text{(the control constraint)}
\end{aligned} \tag{1.2}
$$

The time domain $t \in [0,T_f]$ is used to indicate a specified mission duration T_f, and $G(\cdot)$ is a single-valued function of the integrated running cost $R\left(\vec{x}(t),\vec{u}(t),t\right)$. Subsequent work by Phelps et al. have produced a computational algorithm (with consistency proofs) for discretizing the parameter space to produce a family of *standard* optimal control problems that can be "solved using pseudospectral discretization in the time domain" [5]. Theoretical foundations for this solution approach are summarized in [47]. Walton further generalizes this framework to problems "with parameter uncertainty in both the cost and dynamics of optimal control problems," and analyzes the consistency of states and costates propagated by control trajectories [79]. To support these efforts, Walton developed a flexible software package for specifying and solving these problems via MATLAB. This software allows users to specify different discretization methods, e.g., Euler or pseudospectral, in the time and parameter domains, and "automates the creation of features which are crucial to efficient implementation such as gradient information and sparsity patterns" [79]. All of the simulation results in this dissertation were produced using Walton's software package.

Finally, we note that Ross et al. define a similar framework for solving optimal control problems with uncertain, or "tychastic" parameters. The authors refer to these problems as Riemann-Stieltjes optimal control problems, because their cost functional is given by a Riemann-Stieltjes "functional of functionals" [80]. When applied to an optimal search problem, this formulation produces the same objective function as Equation (1.2), which can be solved via the same computational methods described in [5]. A recent implementation of this framework to solve a problem with uncertain dynamic constraints is described in [9].

1.3 Contributions

Recent theoretical results in [5], [78], [81] have produced a general mathematical and computational framework for solving optimal control problems with parameter uncertainty—generalized optimal control (GenOC). Leveraging a numerical toolbox developed in [79], we formulate and solve several motion planning problems for MCM operations by autonomous vehicles. The application of GenOC to this important naval mission set is a novel contribution of this dissertation. In addition, this dissertation:

1. Develops physics-based sonar detection models to make the GenOC solution framework operationally relevant to the vehicles and sensors currently employed for MCM.
2. Demonstrates, through specific examples, the utility of this method for both optimal trajectory planning and pre-operational mission analysis.
3. Highlights how the proposed approach improves mine detection performance vs. conventional planning methods, especially under time and resource constraints.
4. Illustrates how optimal solutions obtained from this framework can be used to solve inverse problems related to a specific sonar design or vehicle team configuration.

These features make GenOC an attractive technique for investigating new MCM concepts of operations (CONOPS). Each contribution is presented sequentially by chapter[1], as summarized below.

Chapter 2 derives probabilistic detection models for various mine detection and identification sonars carried by MCM vehicles such as the Mk 18 Mod 2 Kingfish and Mk 18 Mod 1 Swordfish AUVs. These models utilize existing techniques from sonar engineering and operations research for predicting sonar performance based on signal excess (computed from the physics-based sonar equations for a given sonar design) and detection rate. Foraker implemented simple models of this form to solve optimal search problems in the GenOC framework [78]. Walton extended this approach to applications beyond optimal search by replacing detection rates with attrition rate functions, deliberately shaped to model desired multi-agent interactions [79]. We present a method for shaping each sonar's detection rate to accurately reflect its physical field of view in three dimensions. This contribution explicitly relates a sonar's performance to the trajectory executed by its search vehicle. Long

[1]Portions of Chapters 2 through 4 were presented at OCEANS 2016 MTS/IEEE Monterey on September 21, 2016 and will be published in ISBN 978-1-5090-1527-6 (IEEE Catalog Number CFP16OCE-POD).

acknowledged in the literature as an important aspect of MCM mission planning, this fact has historically been addressed only by heuristic search patterns.

Chapter 3 presents a flexible method for formulating different MCM operations as optimal search problems readily solved by the GenOC framework. The method's flexibility derives from its modular approach. Depending on the prior information available, different target distribution models can be constructed to produce motion plans ranging from wide area mine detection surveys to target identification missions. Similarly, models for different search vehicles and sensors can be combined to identify the most effective multi-vehicle team for a given MCM scenario. Chapter 4 demonstrates the ability of the GenOC framework to solve sensor-based motion planning problems for different single- and multi-vehicle MCM missions. A single-vehicle example illustrates how optimal trajectories outperform conventional coverage patterns when the time available for conducting a search is limited.

Finally, Chapter 5 proposes a novel use of the GenOC framework to investigate inverse problems concerning the best vehicle or sensor configuration to use in a given MCM scenario. The ability to rapidly solve multiple optimal search problems makes Monte Carlo analysis possible, providing engineering insights about the search assets themselves. This capability stems from the choice of sonar models derived in Chapter 2, which reflect specific sonar design parameters. Hence, it is possible to analyze the impact of parameter changes on optimal search performance and recommend improvements that yield the biggest potential payoff. This dissertation provides examples of several inverse problems and highlights an added benefit of this approach. Namely, since each simulation produces a set of optimal search trajectories for the system under test, inverse problem analyses can be used to construct a library of optimal motion plans for a wide array of MCM missions.

THIS PAGE INTENTIONALLY LEFT BLANK

CHAPTER 2:
Sonar Detection Models

In this chapter, we develop probabilistic models for two types of sensors routinely deployed during mine countermeasures (MCM) operations: forward-looking sonar (FLS) and side-scan sonar (SSS). While these sonar systems can differ widely according to their intended application, they share several common characteristics. First, both FLS and SSS are examples of active sonar. That is, they transmit acoustic signals into the water and process the echoes reflected from objects in the environment to detect their presence. For a given sonar, this process occurs at an average rate, so detection performance depends on time. Second, active sonar systems employ transmit/receive arrays of transducers to improve detection performance in a desired direction and often add acoustic baffling to reject echoes from unwanted directions. A sonar design's array geometry therefore produces an effective field of view (FOV) within which targets can be reliably detected, so detection performance also depends on a sonar's orientation relative to targets in the environment. Last, since these sonar systems are rigidly-mounted onto a vehicle platform, the sonar's orientation ultimately depends on that vehicle's trajectory through the search area. This trajectory defines the position, orientation, and velocity of the vehicle as a function of time. Since these quantities are constrained by the vehicle's equations of motion, we note that a sonar's overall detection performance is a function not only of its design parameters but also its vehicle platform dynamics.

Assuming that detection performance defines a sonar's effectiveness for a given mission, this metric can be generalized to any sonar. That is, a mission to detect and localize mines with a long-range, low-resolution sonar has the same objective as a mission to reacquire and identify these mines with a high-resolution sonar. We assume that detection with such a sonar is sufficient for successful identification to occur. Under these assumptions, sensor-based motion planning algorithms for mine countermeasures (MCM) should employ sonar detection models with the following characteristics:

- Detection probability reflects an actual sonar's dependence on array design, vehicle dynamics, and three-dimensional search geometry. In this way simulation can serve as a powerful tool to evaluate the effectiveness of different sonar designs deployed

from various vehicle platforms.

- Simulated detection performance agrees with the expected/observed performance of actual sonar. This can be assessed by model verification and validation.
- Detection functions permit rapid calculations within numeric optimization routines. This requires trade-offs between accuracy and execution speed. Smooth, differentiable functions with analytic gradients, for example, significantly reduce solution times when using gradient-based optimization.

Many sensor models commonly used in search theory are chosen for their computational simplicity and do not satisfy all of these desired characteristics. Most ignore three-dimensional geometry, for example, but this can greatly impact detection performance when searching for mines on the sea floor with a surface craft's FLS (Figure 2.1) or an underwater vehicle's SSS. It is also well-known that SSS can not detect targets located directly beneath a vehicle's path of travel, in the so-called near-nadir region (Figure 2.2). For this reason, overlapping sensor swaths are required to obtain complete coverage with this sensor [82].

Definite range models, or "cookie cutter" sensors, simply assume that detection is certain within a fixed range of the sensor and impossible outside it. Washburn and Kress note the appeal of such a model for analysis, but acknowledge that "attempts to forecast fixed ranges in the real world are often disappointing," remarking that "forecast detection ranges for sonars are notoriously subject to error—it is not uncommon to be off by a factor of two or more" [23].

One alternative to definite range models are so-called lateral range curves. This approach graphs a sensor's detection probability as a function of lateral range, defined as the distance from a searcher's straight line track at its point of closest approach to a target. The area under a sensor's lateral range curve defines its sweep width, a measure of sensor effectiveness used when planning to search an area with evenly-spaced track lines, e.g., with a lawnmower coverage pattern [83]. Lateral range curves can be derived analytically, assuming detection rate is proportional to range via an inverse cube law, or derived empirically via repeated experiments [51], [84].

Figure 2.3 depicts the lateral range curve and corresponding sweep width for a typical sensor and for the special case of a definite range sensor with radius R overlaid in green.

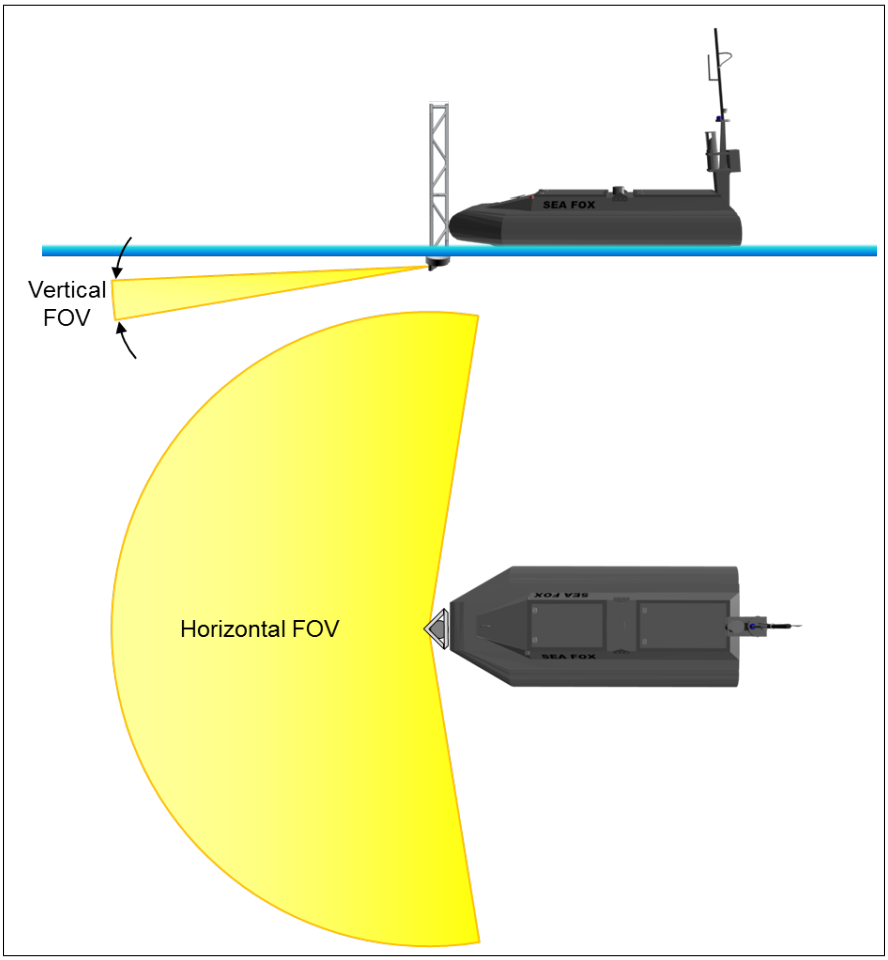

Figure 2.1. Problem geometry for a surface craft with bow-mounted forward-looking sonar.

We note that in general, both sensor models produce maximum detection probabilities at target ranges approaching zero. While appropriate for optical sensors (this was one of the original motivations for deriving the inverse cube law in World War II), these models usually require modifications to accurately simulate sensors like SSS.

One example of a sensor profile used to approximate the expected coverage pattern of SSS (Figure 2.4) is presented in [30]. This model modifies a "cookie cutter" sensor by adding a "blind zone" of zero detection probability in the near-nadir region below the vehicle. The resulting sensor profile is shown in Figure 2.5. This model is well-suited for this specific application, namely finding an optimal track line location that maximizes the probability

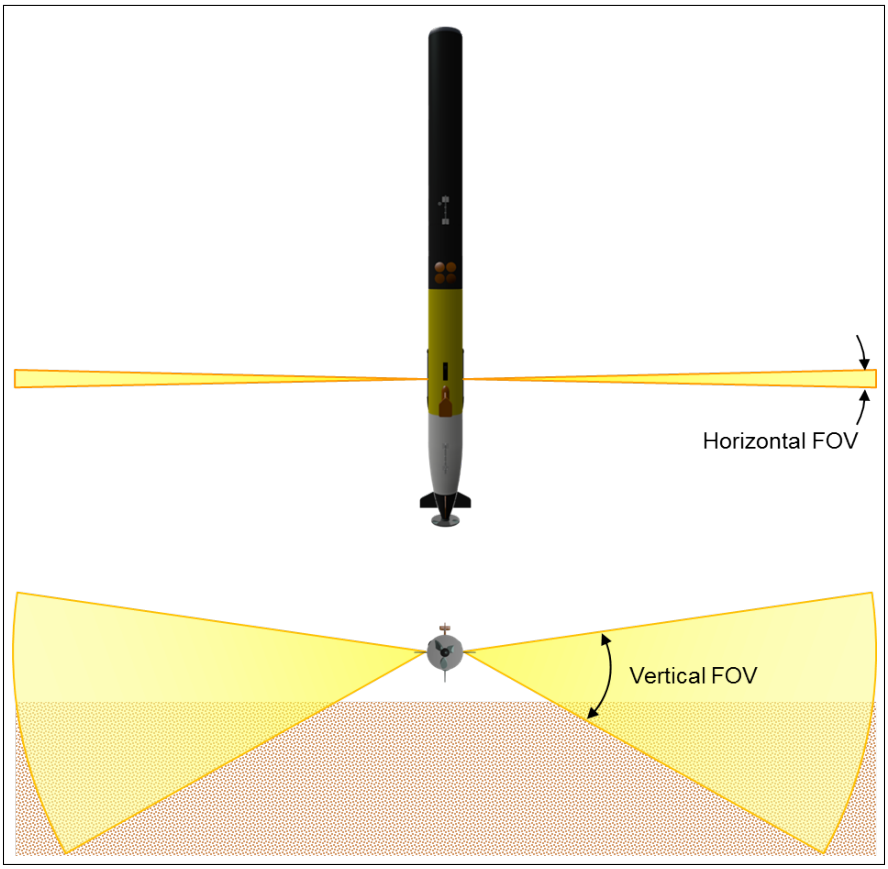

Figure 2.2. Problem geometry for an underwater vehicle with sidescan sonar, showing negligible sensor coverage directly below the vehicle.

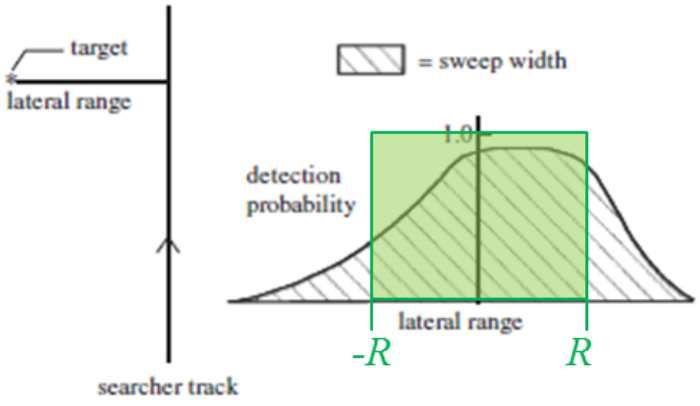

Figure 2.3. Lateral range curves and sweep widths for a typical sensor (black) and a definite range sensor (green). Adapted from [23].

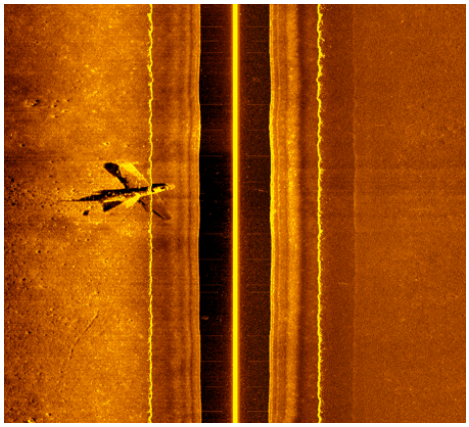

Figure 2.4. Sidescan sonar image showing near-nadir gap. Source: [85].

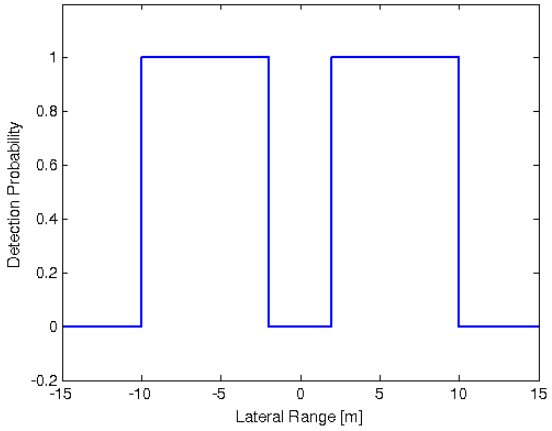

Figure 2.5. Sensor profile modified with near-nadir gap. Adapted from [30].

of detecting targets for a given track line direction, but it does not generalize well to other applications. Furthermore, this sensor model does not depend explicitly on vehicle dynamics; the knowledge that SSS performs better when its vehicle platform follows straight line tracks is implicit in the problem formulation, which considers only straight path segments.

An engineering-based approach to modeling sensors like radar and sonar calculates "signal excess" from physical models of the sensor and its operating environment to determine when detection is possible [51], [84]. Moreover, the Poisson Scan model described in [51] and [86] can be used to derive a sensor's detection rate. Sensor models of this form are used to solve optimal search problems in [7], [11], [78], although these models implement a much simpler approximation of an actual signal excess equation. Nevertheless, [79] describes how models based on rate functions can be calibrated to "shape" their performance and solve a wide variety of problems, highlighting the flexibility of this modeling approach. The following sections present a detailed derivation of the sonar detection models used in the remainder of this dissertation. The main technical contribution of this chapter is a signal excess model that incorporates sonar design parameters and three-dimensional geometery to compute detection probability as a function of a vehicle's trajectory.

2.1 Signal Excess

The signal excess model of sonar detection simulates the conditions under which an active or passive sonar system can detect an underwater object, based on well-known sonar equations. First proposed in [36], signal excess is still widely used in many sonar performance models today, including the U.S. Navy's CASS, a Navy Standard maintained by its Ocean and Atmospheric Master Library (OAML) [87], [88]. CASS is a modular software framework which can interact with multiple different mathematical models, e.g., the Navy's Gaussian Ray Bundle (GRAB) eigenray sound propagation model, to compute individual terms in the sonar equation. For this reason, CASS is an example of a model operating system (MOS), which can solve complex sonar performance modeling problems by decomposing them into smaller sub-problems, each tailored to a specific sonar configuration or operational environment. The flexibility of a MOS can be invaluable when designing a new sonar system or developing a tactical decision aid (TDA) to optimize a sonar's performance in a given environment [56]. Their complexity and large computational runtime, however, make these systems unsuitable for sensor-based motion planning algorithms. Anecdotally, when CASS "is used as the acoustic calculation engine ... computation of signal excess in support of a complex multistatic active sonar analysis task can take days," with the "vast majority of runtime" devoted to computing eigenrays connecting a sonar transmitter, sound-scattering features, and a sonar receiver [89].

Our implementation, therefore, makes simplifying assumptions in order to rapidly compute signal excess for an active sonar attached to a moving vehicle platform:

- We assume detection performance is limited only by acoustic background noise and neglect reverberation due to the sonar's backscattered acoustic energy. Reverberation is a complex function of time, range, and the environment itself (e.g., the roughness of the sea bed) [54]. By using the noise-limited form of the active sonar equation, a constant parameter called the figure of merit (FOM) can be computed for a given sonar design, facilitating qualitative comparisons of detection performance in a given environment.
- We assume that the environment is homogeneous, with a flat bottom type and constant water depth. We further assume a constant sound velocity profile, even though the speed of sound actually varies as a function of temperature, salinity, and depth. These assumptions allow us to forgo computationally expensive ray-tracing calcula-

tions.

- We ignore multipath propagation effects, as MCM sonars typically operate at higher frequencies and relatively short ranges, e.g., hundreds of meters as opposed to tens of kilometers for a submarine sonar system.

The signal excess model assumes that detections can only occur when the acoustic energy transmitted by a sonar is sufficient to overcome the two-way propagation losses in the environment, and the received signal reflected by a target exceeds a detection threshold relative to the prevailing background noise. This signal excess can be computed using well-known sonar equations, "simple algebraic expressions used to quantify various aspects of sonar performance" [84]. Because many terms in the sonar equations represent ratios of measured physical quantities to standard reference values, it is convenient to express them in units of decibels (dB), defined as $10 \log_{10} (Ratio)$. For example, the reference intensity (power per unit area) for sonar is defined as the intensity of a planar sound wave with root mean square (RMS) pressure of one micropascal (μPa). Table 11.1 in [56] defines several sonar parameters and their corresponding reference values. A typical signal excess equation for an active sonar operating against a noise background is given in [84]:

$$SE = SL - 2PL + TS - (N - AG) - DT \tag{2.1}$$

where SE = signal excess,
SL = source level,
PL = one-way propagation loss,
TS = target strength,
N = omni-directional sonar self-noise,
AG = array gain,
DT = detection threshold.

An equivalent expression that includes signal processing terms for computing the detection threshold with frequency modulated (FM) or continuous wave (CW) active pulse types can

be found in [54]:

$$SE = SL - 2PL + TS - (N - DI + 10\log_{10} B) - DT \tag{2.2}$$

where DI = directivity index,

$DT = 5\log_{10} d - 10\log_{10} BT - 5\log_{10} n$,

B = pulse bandwidth [Hz],

T = pulse duration [s],

d = detection index,

n = number of pings used in detection decisions.

Recall that each term in Equation (2.2) is expressed in dB units, unless otherwise specified. We will use this form of the sonar equation in the sections to follow, which derive the physics-based probabilistic sensor models at the heart of our motion planning algorithm. The first step combines terms related to a specific sonar design into a figure of merit (FOM). This metric simplifies performance calculations during trajectory optimization, but permits the direct comparison of different sonar models in a given scenario.

2.2 Figure of Merit

For sonar performance analysis, the terms of the signal excess equation are often combined into the following form:

$$SE(t) = FOM - PL\,(D(t)) \tag{2.3}$$

where FOM = figure of merit,

PL = one-way propagation loss,

$D(t)$ = distance to the target.

In this form, the one-way propagation loss is a function of the distance between a sonar and a target location $\vec{\omega}$ at each moment in time: $D(t) = \|\vec{\omega} - \vec{x}(t)\|$. In our MCM search problem, the target location $\vec{\omega}$ is uncertain but characterized by the probability density function $\phi(\vec{\omega}) : \Omega \mapsto \mathbb{R}$ (see Section 3.3). Figure of Merit (FOM), on the other hand, is a useful metric for comparing the performance of different passive or noise-limited active sonars. For these cases, FOM is constant and independent of both range and environmental

propagation characteristics. It therefore captures all of the sonar design-related parameters for a given sonar operating in a specified noise environment against a defined target.

Physically, FOM represents the maximum allowable one-way propagation loss resulting in zero signal excess. Wagner et al. note that the FOM metric for active sonar "today has fallen into disuse in both shipboard detection range prediction [and] in sonar system design," since the benefit of a constant metric is lost in the reverberation-limited case when FOM must vary with range and environment. "Instead, the individual components of active sonar equations ... are each considered separately in arriving at a performance prediction" [84]. Since analysis of this type often requires a sophisticated MOS like CASS, however, we have elected to continue using FOM and limit our analysis to the noise-limited case.

Assuming target detection is possible when $SE \geq 0$, we compute FOM by substituting Equation (2.2) into Equation (2.3) when $SE = 0$. Combining terms yields an expression for FOM as a function of the relevant design parameters [54]:

$$\begin{aligned} 0 &= SL - 2FOM + TS - (N - DI + 10\log_{10} B) - (5\log_{10} d - 10\log_{10} BT - 5\log_{10} n) \\ FOM &= \frac{1}{2}\left(SL + TS - N + DI + 10\log_{10} T - 5\log_{10} d + 5\log_{10} n\right). \end{aligned} \tag{2.4}$$

We briefly describe each of these parameters, and provide sample calculations for the values used in our simulations. Parameter values specific to the models corresponding to individual sonar designs are derived in Section 2.6.1, Section 2.6.2, and Section 2.7.

- *Directivity index (DI)* of a transducer array describes its ability to "concentrate transmitted sound in a given direction" (DI_t), and improve the signal-to-noise ratio (SNR) received from a given direction (DI_r). The *DI* is "a special case of the *array gain (AG)*, where the signal is coherent and the noise is incoherent. This parameter is simpler to calculate and will normally be a satisfactory measure of the increase in SNR due to the array" [54]. This parameter is a function of the sonar's design frequency and array geometry.

- *Source level (SL)* of a projector array is a function of its acoustic power, P. If the array is directional, *SL* also depends upon the DI_t.

- *Pulse duration (T)* determines a sonar's range resolution, with shorter pulses providing better resolution due to smaller echo separation. A CW "pulse of constant frequency and duration T seconds" will have a bandwidth, $B = 1/T$ Hz. For FM pulses, "the frequency of the pulse changes during the T seconds duration of the pulse [and] the bandwidth, B, is *not* now the inverse of the pulse length" [54].

- *Detection index (d)* is used to determine a sonar receiving system's detection threshold (DT), expressed as the SNR corresponding to preset values for probability of detection (P_d) and probability of false alarm (P_{fa}). Here, P_d is the probability that amplitudes measured at the receiver which exceed DT consist of signal plus noise; and P_{fa} is the probability they consist of noise only. This relationship is typically plotted as a function of $5 \log_{10} d$ on a curve of receiver operating characteristics (ROC). The sonar models derived below assume $5 \log_{10} d = 10$ dB, corresponding to $P_d = 0.5$ and $P_{fa} = 10^{-5}$ as given by Table 7.8 in [54] and used in the sonar design examples included in this reference.

- The *number of pings (n)* contributing to a detection decision effectively reduces a sonar's DT as more information is considered. The sonar models derived below assume $5 \log_{10} n = 3$ dB, equivalent to processing four pings per decision; this value is used for all sonar design examples in [54].

- *Target strength (TS)* is the ratio of the intensity of the sound wave reflected by an underwater target, relative to the intensity of the incident sound wave from an active sonar pulse. This quantity, expressed in dB, is a function of sonar frequency, target size, geometry, and the angle of incidence between the sonar pulse and target. The goal of our MCM search problem is to detect small mines on the sea floor with geometry approximated by finite cylinders of radius 0.1 meter and length 1.0 meter, with hemispherical ends. For incident angles normal to the mine, TS is computed for a cylinder with radius a, length L, and wavelength λ using the formula $TS = \log_{10}\left(\frac{aL^2}{2\lambda}\right)$. The worst case TS, however, for incident angles striking one of the two ends, is computed for a sphere with radius a using the formula $TS = \log_{10}\left(\frac{a^2}{4}\right) = -26$ dB. Therefore, we use the conservative value of $TS = -30$ dB [54].

- *Noise (N)* refers to the intensity level of the background noise that a desired signal must overcome to be detectable at the sonar receiver. Ambient noise in the ocean is due to three main sources: 1) noise in the sonar receiving system induced by thermal agitation of water molecules against the face of the hydrophone; 2) ambient sea noise from wind and waves, rain, distant shipping, and biological activity; and 3) vessel self-noise due to machinery, propellers, electrical interference, and fluid flow [54]. All of these sources contribute to the ambient noise level in different frequency bands, as illustrated by Figure **??**. The average spectral level for thermal noise is depicted by the straight line in the bottom right corner of the plot. This line dominates other noise sources at the high frequencies used for mine hunting sonar, i.e., above 100 kHz, and can be computed for a given sonar frequency f Hz by the equation [53]:

$$N_{therm} = -75 + 20 \log_{10} f \text{ dB}. \tag{2.5}$$

Even though exact design parameters for Navy sonars are difficult to obtain (and potentially classified) [84], a figure of merit (FOM) suitable for relative performance analysis can still be estimated from sonar design reference manuals [54] or commercial sonar specifications [91]–[93]. Furthermore, once the FOM for a given sonar problem is known, it is easy to compute the signal excess along a moving vehicle's trajectory $\vec{x}(t)$, since it depends only on the propagation loss due to distance between vehicle and target. Consequently, calculating detection probability based on signal excess is especially attractive for sensor-based motion planning algorithms.

2.3 Propagation Loss

An acoustic pulse loses intensity as it propagates through the water, as the radiated power spreads throughout a larger and larger area. This can be modeled as spherical spreading, in which power is radiated in all directions, or as cylindrical spreading, in which power spreads outward between two planar boundaries. The pulse is also attenuated by absorption losses due to fluid viscosity and molecular relaxation of dissolved salts in seawater. Both spreading and absorption are functions of distance. For our signal excess calculations, we assume that propagation losses are due only to spherical spreading and absorption, "a useful working rule for initial design and performance comparisons" [54]. In fact, this same

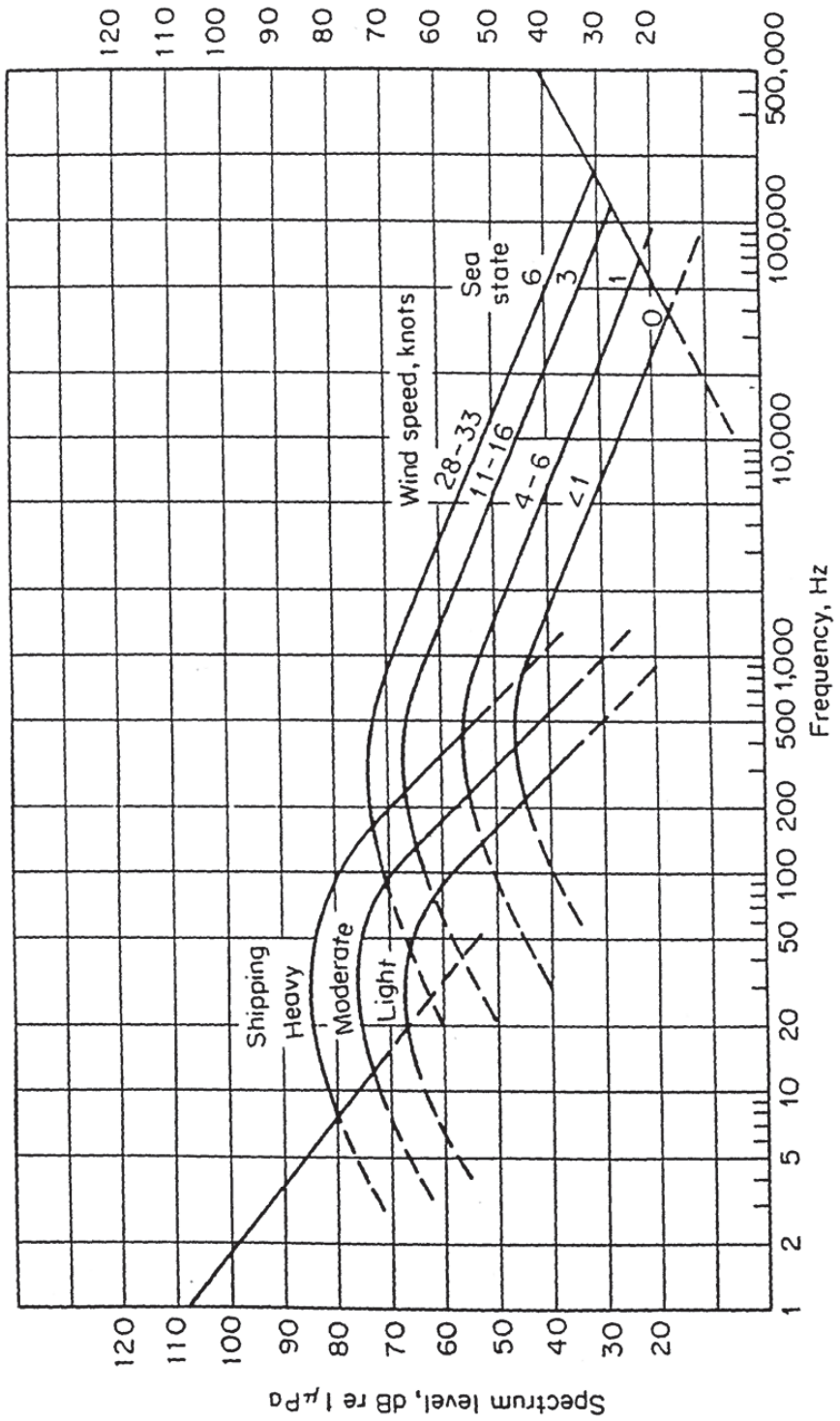

Figure 2.6. Average ambient noise spectra. Source: [90], from [53].

assumption is often required "in order to make reverberation models feasible" [56]. Neglecting other loss sources (e.g., scattering and refraction) via the simplifying assumptions listed in Section 2.1, propagation loss is

$$PL(\vec{x}(t),\vec{\omega}) = 20\log_{10}\left(\|\vec{\omega} - \vec{x}(t)\|\right) + a\,\|\vec{\omega} - \vec{x}(t)\|\,, \tag{2.6}$$

where a is the frequency-dependent attenuation coefficient of seawater. Tabulated values of a can be found in sonar design references such as [54] and [55]. While a varies with depth, salinity, and temperature, it depends most strongly on the sound frequency. We therefore compute this parameter using an equation in [53], which estimates a as a function of frequency in kHz:

$$a = \frac{0.11f^2}{1+f^2} + \frac{44f^2}{4100+f^2} + 0.0003f^2 + 0.003 \text{ dB/km}. \tag{2.7}$$

2.4 Instantaneous Detection Rate

In search theory, "the detection rate approach to computation of detection probabilities has proved to be more robust than the geometric models" used by "cookie cutter" sensor models [51]. Originally developed in [36], this method assumes that a sensor has a detection rate $\gamma(t)$ called the "*instantaneous probability density* (of detection)." This rate may vary with time due to the motion of searchers and targets, or to reflect changing environmental conditions, for example. Continuously searching over a small time interval Δt constitutes a single glimpse or scan with the sensor. Each glimpse provides a detection opportunity with the instantaneous probability of detecting a target given by $\gamma(t)\Delta t$. This leads to the well-known exponential detection model, discussed in Section 3.4, which quantifies detection probability as a function of time.

In order to use the exponential detection model, we must first compute detection rates for our sonar models. Detection rates based on our noise-limited signal excess model vary with distance between a target location $\vec{\omega}$ and a search vehicle following the trajectory $\vec{x}(t)$. If we also assume that the signal excess in Equation (2.3) is a normally-distributed random variable with mean SE and variance σ^2, the instantaneous probability of detection for a

single glimpse with a sonar can be written using its cumulative normal distribution Φ [51]:

$$p(\vec{x}(t),\vec{\omega}) = \Phi\left(\frac{SE\left(\vec{x}\left(t\right),\vec{\omega}\right)}{\sigma}\right). \tag{2.8}$$

Based on our selection of the detection index d in Section 2.2, the instantaneous detection probability $p(t) = 0.5$ when $SE(t) = 0$, meaning the sonar has an equal probability of detecting or missing a mine. Regarding the selection of σ, Washburn notes that "most practitioners use a value of σ somewhere between 3 and 9 dB for sonar detection in the ocean" [51]. A value of $\sigma = 5.6$, computed by adding typical variance values for each term in the sonar equation, is provided in [84]. Moreover, a study which used the Navy's CASS/GRAB software to simulate acoustic mine detections under varying environmental conditions, including seasonal sound speed profiles, unknown wind speeds, and imprecise bottom types, observed signal excess variations of 3 dB, 6 dB, or 9 dB in most cases [57], [58]. Figure 2.7 plots the instantaneous probability of detection vs. signal excess for these three values of σ.

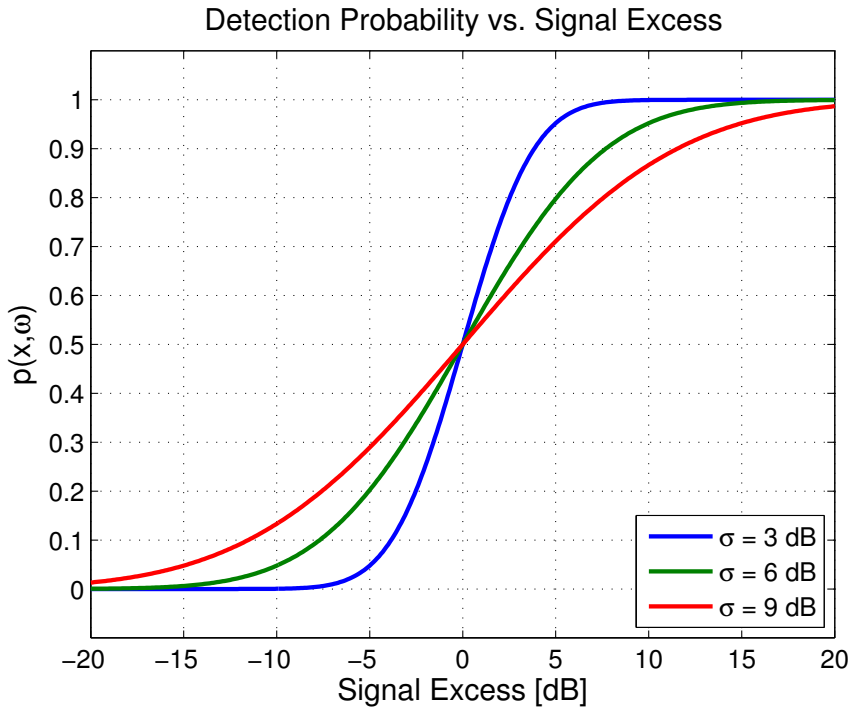

Figure 2.7. Instantaneous detection probability vs. signal excess and σ.

To compute a sonar's detection rate $\gamma(t)$ from its instantaneous detection probability $p(t)$, we further assume that detection opportunities (glimpses) can be modeled as a Poisson process and occur with mean rate λ. The so-called Poisson Scan model produces the detection rate $\gamma(\vec{x}(t),\vec{\omega}) = \lambda p(\vec{x}(t),\vec{\omega})$ [51].

2.5 Detection Performance Modifiers

The sonar detection model developed thus far, based on signal excess remaining after subtracting propagation losses from a given sonar's figure of merit, is omni-directional. It depends only on the distance between the sonar and a MLO. This function could be used to construct a lateral range curve and corresponding sweep width for use in standard coverage planning algorithms [23]. Most actual sonar systems, however, are designed to transmit and receive with a specific beam pattern (see, e.g., Figure 2.1 and Figure 2.2) and do not perform equally well in all directions. Actual detection performance depends not only on a sonar's distance from a target, but also whether (and how long) it is pointed in the proper direction, at the proper place and time, to ensonify the target. The vehicle platform must maneuver to accomplish this. Conversely, high-resolution imaging sonars which rely on platform motion to methodically scan the sea floor (e.g., sidescan sonar) or construct long virtual hydrophone arrays (e.g., synthetic aperture sonar), require precise navigation along straight line trajectories to generate accurate imagery [13], [94]. Excessive platform motion can often yield poor performance for these systems. It is clear that sonar performance is tightly coupled to a vehicle's motion. In the following sections, we derive simple shaping functions to model a sonar's three-dimensional beam geometry as well as its dependence on platform motion.

2.5.1 Field of View Considerations

To more accurately estimate a sonar's true detection performance when mounted on a vehicle, we must enforce its actual beam geometry in three dimensions. First, we define angular limits for the sonar's horizontal and vertical fields of view (FOV). These FOV boundaries exist in the sonar reference frame, but we will assume without loss of generality that this frame is identical to the vehicle's body-fixed reference frame. Next, we calculate the vectors between the sonar and each potential target, and resolve them in the body-fixed reference frame to compute the angle to each target relative to the sonar's FOV. Finally, we

apply a shaping function to degrade detection performance for targets that fall outside of the angular FOV limits.

The horizontal plane geometry at an instant in time is shown in Figure 2.8 for a SeaFox USV and forward-looking sonar with horizontal FOV, α_{FOV}, of 200 degrees. Parameters defined or resolved in the body-fixed frame are denoted with a superscript b. The positions of the USV $[x, y]^T$ and potential mine target locations $\left[\omega_x, \omega_y\right]^T$ are defined in the inertial reference frame $\{n\}$. We compute the lower and upper limits on azimuth angle for a sonar's horizontal FOV by the expressions

$$\begin{aligned} {}^b\alpha_L &= -\frac{\alpha_{FOV}}{2}, \text{ and} \\ {}^b\alpha_U &= +\frac{\alpha_{FOV}}{2}. \end{aligned} \tag{2.9}$$

The vector between the sonar and a target of interest in the inertial frame is then defined as $\Delta\vec{x} = \left[\omega_x - x,\ \omega_y - y\right]^T = [dx,\ dy]^T$. To determine the azimuth angle to this target in the sonar's FOV, the vector $\Delta\vec{x}$ must be resolved in the body-fixed reference frame using the vehicle's heading angle ψ, producing the body-fixed components:

$${}^b dx = {}^n dx \cos(\psi) + {}^n dy \sin(\psi), \text{ and} \tag{2.10}$$

$${}^b dy = -{}^n dx \sin(\psi) + {}^n dy \cos(\psi). \tag{2.11}$$

Then, using the four-quadrant inverse tangent, we compute

$${}^b\alpha = \text{atan2}({}^b dy,\ {}^b dx). \tag{2.12}$$

In the same manner, we compute the lower and upper limits on elevation angle for the sonar's vertical FOV as:

$$\begin{aligned} {}^b\varepsilon_L &= \varepsilon_{DE} - \frac{\varepsilon_{FOV}}{2}, \text{ and} \\ {}^b\varepsilon_U &= \varepsilon_{DE} + \frac{\varepsilon_{FOV}}{2}. \end{aligned} \tag{2.13}$$

Here, ε_{DE} is a fixed downward elevation angle selected to ensure that the sonar can ensonify the sea floor. Some sonar systems are capable of electronically steering their beams

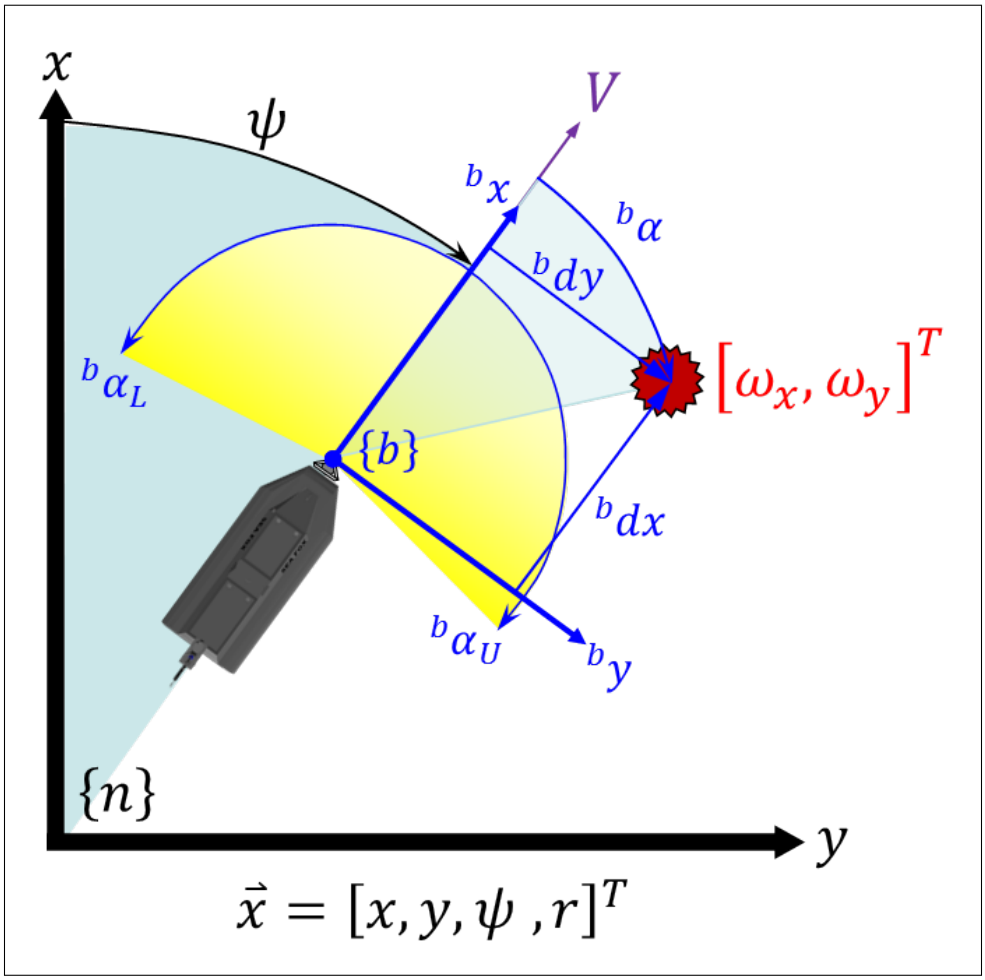

Figure 2.8. Instantaneous geometry for a forward-looking sonar's horizontal field of view.

to a specified ε_{DE}, but this angle is frequently determined by a fixed mechanical mounting angle. For a vehicle traveling in the horizontal plane at constant altitude h above the bottom, the elevation angle between the sonar and a mine on the sea floor is identical in both reference frames, computed by

$$\varepsilon = {}^{b}\varepsilon = {}^{n}\varepsilon = \arctan\left(\frac{-h}{\sqrt{(\omega_x - x)^2 + (\omega_y - y)^2}}\right) = \arctan\left(\frac{-h}{\sqrt{dx^2 + dy^2}}\right). \quad (2.14)$$

We now define scalar shaping functions which degrade sonar detection performance for

mines outside the sonar's horizontal (or vertical) FOV. Each shaping function is constructed from two logistic functions [95]. These S-shaped sigmoidal curves [96] are calibrated to smoothly transition a scalar value from 1 to 0 at the angular limits of the sonar's FOV. This value modifies the probability of detecting a mine at a given location based on signal excess only, thereby preventing detection if the mine location lies beyond these angular limits. The azimuth and elevation shaping functions are

$$^{FLS}F_{\alpha}(\vec{x}(t),\vec{\omega}) = \frac{1}{1+e^{p_{\alpha}({}^{b}\alpha_{L}-{}^{b}\alpha)}} + \frac{1}{1+e^{p_{\alpha}({}^{b}\alpha-{}^{b}\alpha_{U})}} - 1, \text{ and} \tag{2.15}$$

$$F_{\varepsilon}(\vec{x}(t),\vec{\omega}) = \frac{1}{1+e^{p_{\varepsilon}({}^{b}\varepsilon_{L}-{}^{b}\varepsilon)}} + \frac{1}{1+e^{p_{\varepsilon}({}^{b}\varepsilon-\alpha_{U})}} - 1, \text{ respectively.} \tag{2.16}$$

The p_{α} and p_{ε} parameters can be tuned to adjust the slope of their respective sigmoidal curves, as discussed in Section 2.5.3. Figure 2.9 plots the azimuth scale factor vs. target azimuth angle and several values of p_{α} for an FLS with a 120-degree horizontal FOV.

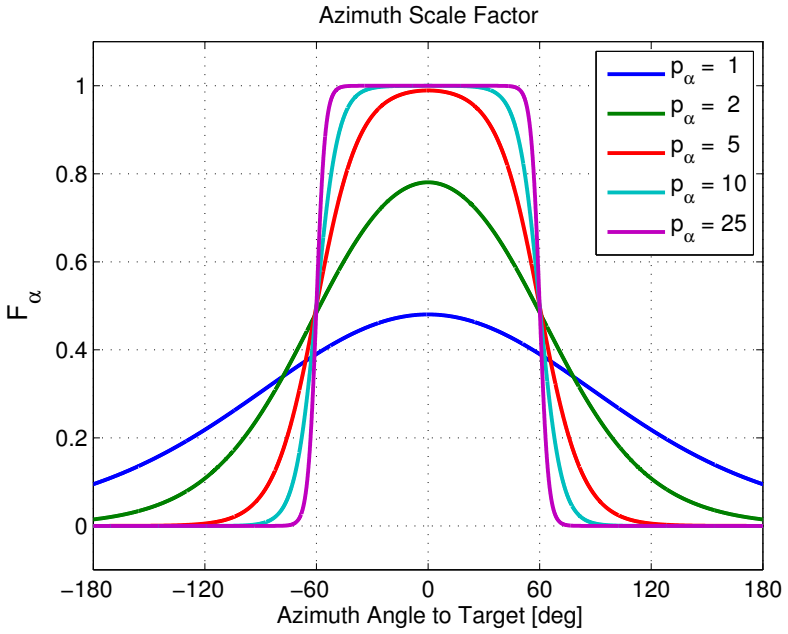

Figure 2.9. F_{α} vs. azimuth angle and p_{α} for a forward-looking sonar with 120-degree horizontal field of view.

Similarly, Figure 2.10 plots the elevation scale factor vs. target elevation angle and several values of p_ε for a sonar with a 30-degree vertical FOV mounted at $\varepsilon_{DE} = -15$ degrees. Although the x-axes of Figure 2.9 and Figure 2.10 are labeled in degrees, both functions are actually computed for azimuth (or elevation) angles given in radians.

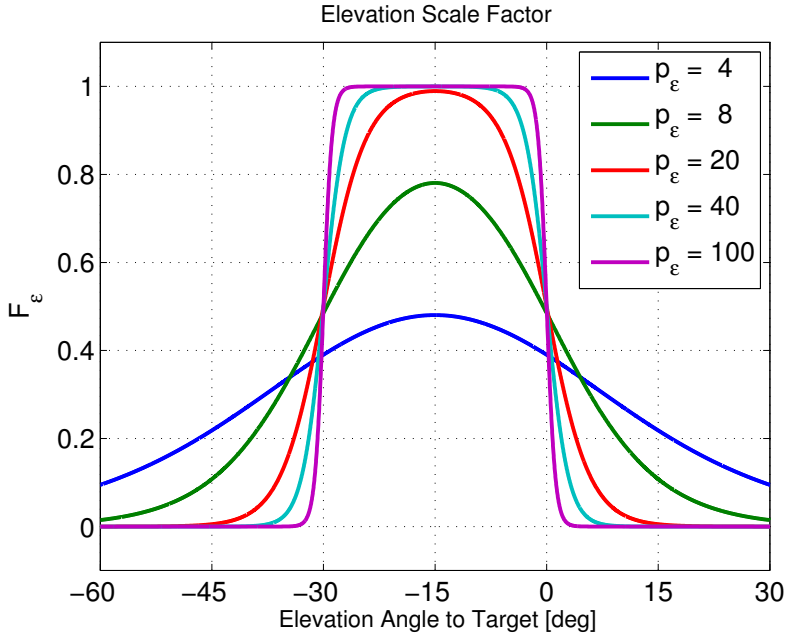

Figure 2.10. F_ε vs. elevation angle and p_ε for a forward-looking sonar with 30-degree vertical field of view mounted at -15 degrees.

The plots in Figure 2.11 and Figure 2.12 illustrate how detection probability based on signal-excess can be shaped using a sonar's FOV. The color map indicates the probability of detecting a mine relative to the sonar's reference frame. Figure 2.11 shows the horizontal plane geometry. The left plot shows the omni-directional detection probability, based on signal excess, for a forward-looking sonar with $FOM = 72$ dB and $\sigma = 9$ dB. The right plot shows the modified detection probability after applying an azimuth scale factor F_α corresponding to a horizontal FOV of 120 degrees with $p_\alpha = 10$. Similarly, Figure 2.12 shows the vertical plane geometry. The left plot shows the modified detection probability after applying an elevation scale factor F_ε corresponding to a vertical FOV of 30 degrees with $p_\varepsilon = 40$. The sonar head is mounted on a surface craft with $\varepsilon_{DE} = -15$ degrees. Note that the different scales used for distance (x-axis) and depth (z-axis) distort the apparent

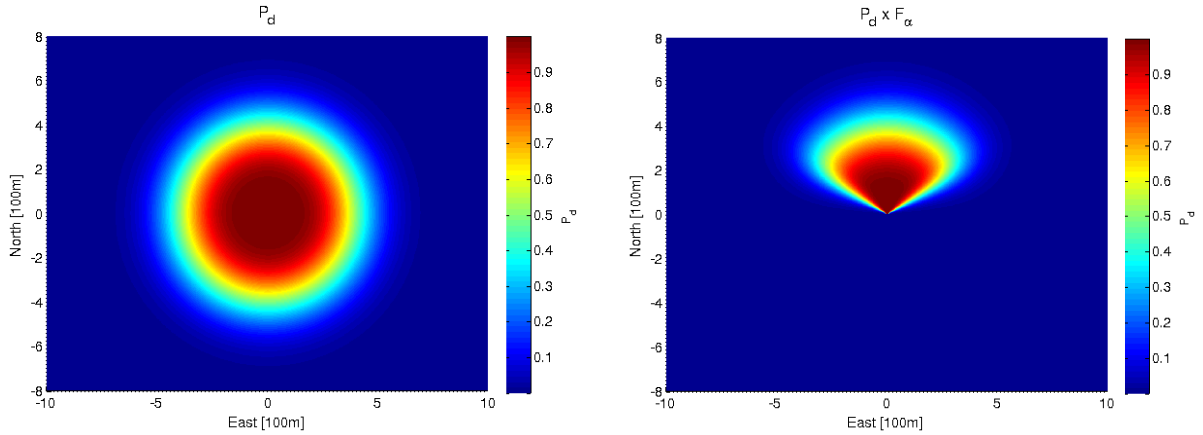

Figure 2.11. Omni-directional detection probability before (left) and after modification by F_α (right) for a 120-degree horizontal field of view.

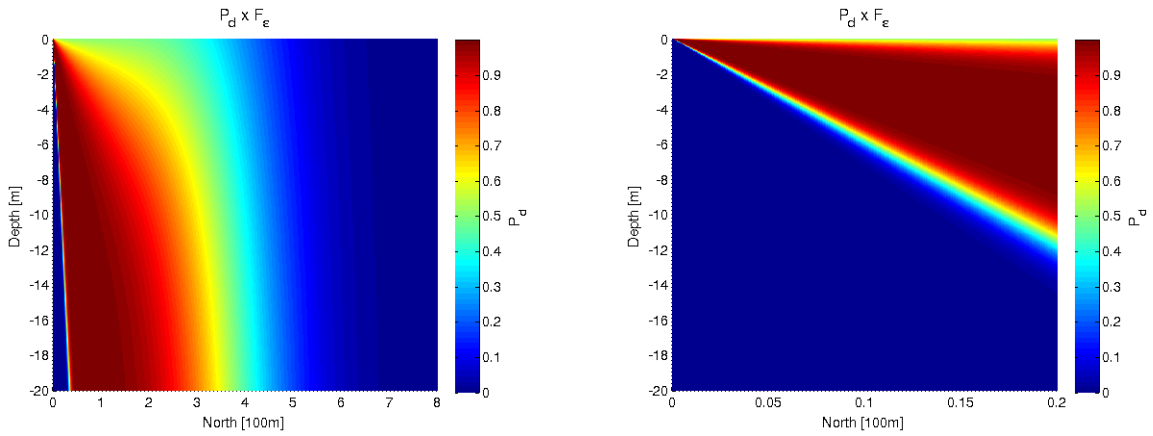

Figure 2.12. Detection probability after modification by F_ε for a 30-degree vertical field of view mounted at -15 degrees (left) and close up (right).

beam angle in this plot, but a close up version shown at right, plotted with equal axis scaling, reflects the expected vertical FOV.

For a sidescan sonar comprised of dedicated port and starboard arrays, it is still possible to construct a continuous shaping function that describes both fields of view over the entire range of azimuth angles ${}^b\alpha \in [-\pi, \pi]$. In this case, we define the lower and upper azimuth limits relative to the center of the starboard array's FOV, $\alpha_{mid} = \pi/2$ as

$$ {}^b\alpha_L = \alpha_{mid} - \frac{\alpha_{FOV}}{2} \quad \text{and} \quad {}^b\alpha_U = \alpha_{mid} + \frac{\alpha_{FOV}}{2}. \tag{2.17} $$

The shaping function for the starboard array is calculated as before, i.e., ${}^{stbd}F_\alpha(\vec{x}(t),\vec{\omega}) = {}^{FLS}F_\alpha(\vec{x}(t),\vec{\omega})$, using Equation (2.15) and these new angular limits. Next, the shaping function for the port side array is calculated as

$$ {}^{port}F_\alpha(\vec{x}(t),\vec{\omega}) = \frac{1}{1+e^{-p_\alpha({}^b\alpha_L + {}^b\alpha)}} + \frac{1}{1+e^{p_\alpha({}^b\alpha + {}^b\alpha_U)}} - 1. \tag{2.18} $$

Combining these shaping functions yields

$$ {}^{SSS}F_\alpha(\vec{x}(t),\vec{\omega}) = {}^{stbd}F_\alpha(\vec{x}(t),\vec{\omega}) - {}^{port}F_\alpha(\vec{x}(t),\vec{\omega}). \tag{2.19} $$

Figure 2.13 plots the azimuth scale factor vs. target azimuth angle and several values of p_α for a SSS with a 10-degree horizontal FOV.

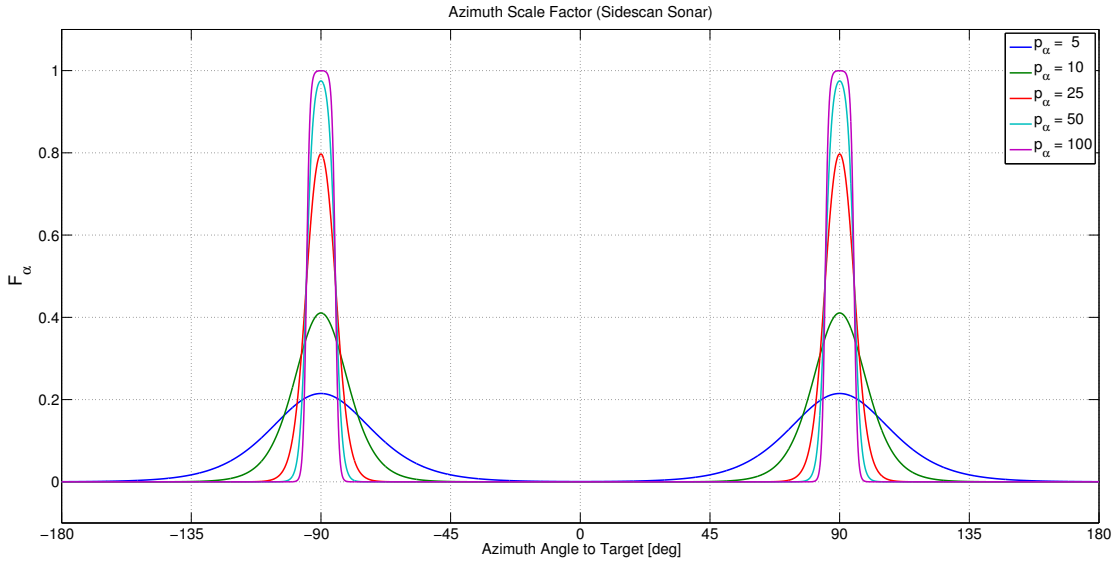

Figure 2.13. F_α vs. azimuth angle and p_α for a sidescan sonar with 10-degree horizontal field of view.

Using the Poisson Scan model, we can now compute the instantaneous detection rate for a given sonar by combining the effects of signal excess, three-dimensional FOV geometry, and average scan rate in the expression

$$ \gamma(\vec{x}(t),\vec{\omega}) = \lambda p(\vec{x}(t),\vec{\omega}) F_\alpha(\vec{x}(t),\vec{\omega}) F_\varepsilon(\vec{x}(t),\vec{\omega}). \tag{2.20} $$

2.5.2 Turn Rate Considerations

As already mentioned, some types of sonar require stable, straight line motion of a vehicle platform to produce high-resolution imagery. Sidescan sonar (SSS), for example, stacks the backscattered signals received from successive pings to produce an image of the sea floor. The across-track dimension of the resulting image corresponds to the two-way travel time of each ping, while the along-track dimension is formed by the vehicle's forward motion. Turning maneuvers, therefore, have a direct impact on SSS performance [97]. In fact, "yawing motions ... are considered to have potentially the most serious degrading effects on sidescan images, because yaw causes the beam footprint to move along-track a distance proportional to the distance across-track" [98]. We model this behavior by applying another scale factor to degrade detection probability as a function of the vehicle turn rate, $r(t)$. We select the Gaussian-like expression

$$F_r(\vec{x}(t)) = e^{-\frac{1}{2}[r(t)/\sigma_r]^2}. \tag{2.21}$$

This function reaches a maximum value of one for straight line motion, e.g., when $r(t) = 0$, but falls off smoothly for non-zero turn rates. The slope of this curve can be adjusted via the tuning parameter σ_r, as shown in Figure 2.14. Using this scale factor, we compute the instantaneous detection rate for a sidescan sonar by the expression

$$\gamma(\vec{x}(t),\vec{\omega}) = \lambda p(\vec{x}(t),\vec{\omega}) F_\alpha(\vec{x}(t),\vec{\omega}) F_\varepsilon(\vec{x}(t),\vec{\omega}) F_r(\vec{x}(t)). \tag{2.22}$$

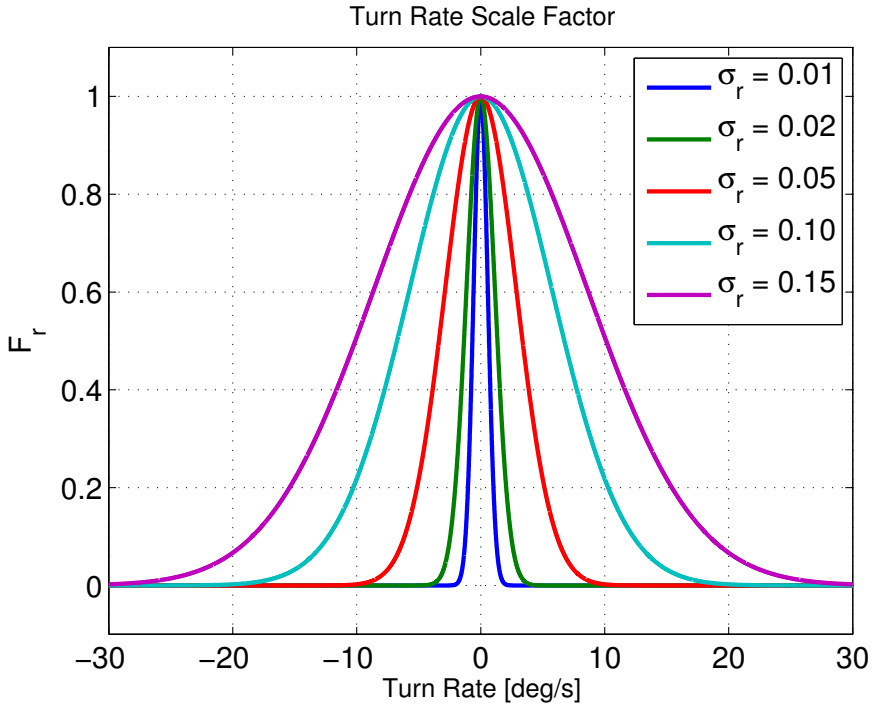

Figure 2.14. F_r vs. turn rate $r(t)$ and σ_r.

2.5.3 Numeric Considerations

A primary consideration when selecting the shaping functions described in Section 2.5.1 and Section 2.5.2 is their numerical smoothness. We shall see in Chapter 3 how instantaneous detection rate can be used to create an objective function for our optimal search problem. Having a smooth (i.e., differentiable) objective function is extremely helpful when performing numeric optimization. Another consideration is the ability to derive and encode analytic expressions for the objective function gradients. The SNOPT software package used to solve our optimal search problem, for example, "is able to estimate gradients by finite differences ... for each variable whose partial derivatives need to be estimated. *However*, this reduces the reliability of the optimization algorithms, and it can be very [computationally] expensive if there are many such variables" [99].

These shaping functions were also designed to be flexible, as the logistic functions can be calibrated to reflect most sonar FOV geometries by setting the azimuth and elevation

angular limits and tuning a single growth rate parameter: p_α for azimuth angle, or p_ε for elevation angle. Each parameter multiplies the exponents in Equation (2.15) and Equation (2.16), respectively, to control the slope of its sigmoidal curve. This defines the "crispness" of a sonar's FOV boundary between regions of high and low detection probability. Low parameter values result in a gradual transition. As values increase, however, this transition tends toward a discontinuous step function, which presents numerical difficulties. Therefore, we have derived a heuristic to guide the selection of an appropriate growth rate value based on two qualitative metrics:

- *Scale Factor Threshold (SFT)*: the value the scale factor should attain within the sonar's field of view (FOV).
- *Fraction Below Threshold (FBT)*: the portion of the nominal FOV that is below the desired *SFT*.

The logistic function, evaluated at a FOV boundary, can be rearranged to calculate growth rates that satisfy these metrics for the azimuth and elevation shaping functions via the expressions

$$p_\alpha = -\frac{2\ln(1-SFT)}{FBT\cdot H_{FOV}}, \text{ and } p_\varepsilon = -\frac{2\ln(1-SFT)}{FBT\cdot V_{FOV}}, \text{ respectively.} \tag{2.23}$$

One can experiment with these metrics to arrive at a growth rate value that achieves a balance between realistic FOV boundaries and a smooth objective function for numeric optimization.

Finally, we acknowledge that for distances less than one meter, the spherical spreading term $20\log_{10}(\|\vec{\omega}-\vec{x}(t)\|)$ in Equation (2.6) will contribute a negative propagation loss, since spreading losses are defined relative to an intensity measured one meter away from the source. Even more concerning is the fact that this term is undefined when the distance equals zero. However, since our MCM search problem is focused on finding bottom mines, the distance to any mine target is guaranteed to exceed one meter as long as our search vehicle travels at an altitude of one meter or greater.

2.6 Forward-Looking Sonar Models

This section derives figure of merit (FOM) values for the forward-looking sonar models used in this dissertation. We consider two different designs:

1. A long-range, low-resolution sonar designed with a cylindrical transducer array to provide a wide horizontal FOV. This type of sonar is typically used for wide-area surveys to detect MLOs during the first phase of an MCM operation.
2. High-resolution, blazed array imaging sonar suitable for reacquisition and identification of previously detected targets during follow-on MCM missions.

Both FLS designs are examples of "sectorscan sonar," which generate two-dimensional images from each pulse [94]. Examples of this imagery are shown in Figure 2.15.

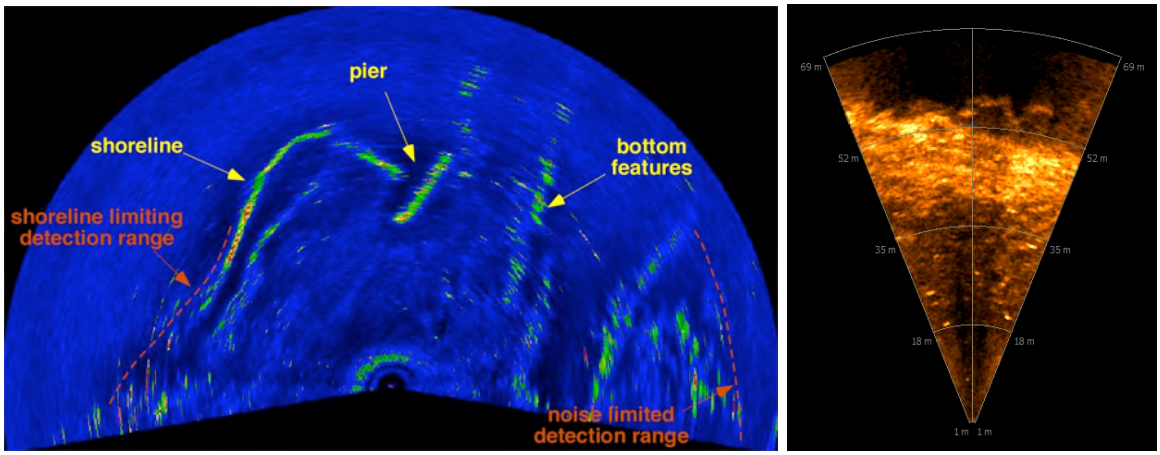

Figure 2.15. Sample images from a cylindrical array (left) and blazed array (right) FLS. Image at left is courtesy of Thunder Bay 2010 Expedition, NOAA-OER. Source: [100].

2.6.1 Cylindrical Array Model

A cylindrical array of transducer elements is a common, practical sonar design. Individual elements are grouped in vertical lines, or staves, to obtain a desired vertical beamwidth, and multiple staves are arranged in a ring to provide the required azimuth coverage [54]. Arrays of this type can be found on submarines, as pictured in [58] and [101], and in systems like the Autonomous Topographic Large Area Sonar (ATLAS), shown mounted on the NPS SeaFox USV in Figure 2.16. A FOM for a long-range detection sonar similar to ATLAS

Figure 2.16. An ATLAS forward-looking sonar mounted on the NPS SeaFox USV.

can be computed using the design example for a mine-hunting sonar described in Chapter 11 of [54].

We specify a 200 kHz sonar with 120-degree horizontal field of view, 5-degree vertical field of view, and a nominal operating range of 400 meters. We assume this sonar transmits an FM pulse with bandwidth $B = 80$ kHz and duration $T = 10$ ms, which yields better noise-limited performance than a CW pulse for the values used in [54]. We further assume that the sonar's projector array is comprised of multiple transducer elements so it can steer its beam in the vertical plane. From the expression in Table 2.3 of [54], the number of elements required for a sonar stave to achieve a beamwidth of 5 degrees is $n = 100/BW = 100/5 = 20$. Assuming the horizontal transmit beamwidth is 120 degrees, the projector array requires only $m = 1$ vertical stave, and the transmit directivity index for this baffled, cylindrical array can be calculated from Table 2.5 in [54] by the expression

$$DI_t = 3 + 10\log_{10} mn = 3 + 10\log_{10}(1 \cdot 20) = 16 \text{ dB}. \tag{2.24}$$

If we assume that the total acoustic power radiated by this projector is $P = 10$ Watts, we can compute the source level (SL) for the sonar as described in [54] by the expression

$$SL = 10 \log_{10} P + 170.8 + DI_t = 197 \text{ dB}. \tag{2.25}$$

Turning attention to the sonar's receive array, we specify narrow, 2-degree horizontal and vertical beam widths so the sonar can resolve small MLOs in its field of view. Table 2.5 in [54] provides a formula for calculating the receive directivity index of a baffled, cylindrical array based on its height h in meters, diameter d in meters, and design frequency f in kHz. For this sonar, the receive directivity index is

$$DI_r = 10 \log_{10} 5hdf^2. \tag{2.26}$$

Assuming half-wavelength spacing of its transducer elements (a function of the design frequency), the array's height is $h = 76/(BW_v \cdot f) = 76/(2 \cdot 200) = 0.19$ m, while its diameter is $h = 88/(BW_h \cdot f) = 88/(2 \cdot 200) = 0.22$ m [54]. Substituting these values into Equation (2.26), we compute $DI_r = 39$ dB for this receive array.

Next, we compute the attenuation coefficient using Equation (2.7), and the noise background due to thermal agitation using Equation (2.5), both functions of the sonar's 200 kHz design frequency. The attenuation coefficient is $a = 52$ dB/km and the noise due to thermal agitation is $N_{therm} = 31$ dB. However, we use a more conservative value of $N = 34$ dB to compute figure of merit in Equation (2.4). This 3 dB increase can accommodate additional self-noise from the vehicle platform at levels comparable to the calculated N_{therm} value [54], e.g., for loud vehicles like the NPS SeaFox USV.

Finally, we estimate the Poisson Scan rate for this sonar model using the concept of "ping-to-ping overlap" illustrated in Figure 2.17. This capability generates multiple looks, from different viewpoints, at MLOs on the sea floor, providing better detection and mapping performance [100]. It also makes sectorscan sonar more robust to turning maneuvers than SSS, provided the vehicle platform has sufficiently accurate navigation. To ensure 95% ping-to-ping overlap from a sonar with 400-meter swath width, mounted on an AUV traveling 1.5 m/s, the sonar must ping about every 10 seconds. Therefore, To accommodate faster USV platforms, we assume that our sonar model pings every 5 seconds, which corresponds to a

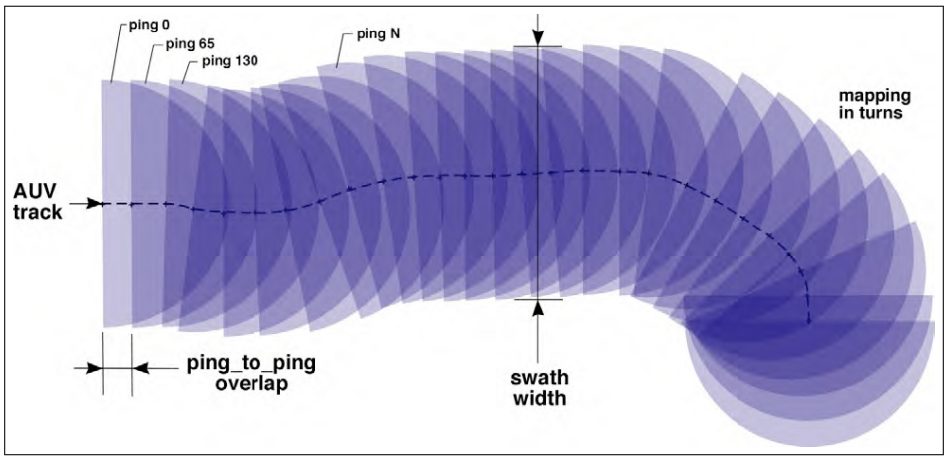

Figure 2.17. Ping-to-ping overlap for a wide-sector FLS. Image courtesy of Thunder Bay 2010 Expedition, NOAA-OER. Source: [100].

Poisson Scan rate $\lambda = 0.2$ scans per second.

The parameters used to model this sonar are listed in Table 2.1. All specified (or assumed) values are *italicicized*, while calculated values are listed in plain text. The operating frequency, projector source level, cylindrical array geometry, and pulse characteristics chosen for this design yield a FOM of 72 dB.

2.6.2 Blazed Array Models

A relatively recent sonar design technique, based on "blazed" acoustic arrays, has led to a class of smaller, lighter, lower power imaging sonars which are well-suited for deployment from small autonomous underwater vehicles. Leveraging techniques from the fields of radar and optics, a blazed array can "map angular image information into the frequency domain" [102]. In principle, these acoustic arrays are analogous to optical diffraction gratings which can separate a broad spectrum signal (white light) into individual, angularly-separated frequencies (colors) [103]. Blazed sonar arrays separate a broadband acoustic pulse into a "frequency-dispersed sound field" in which each frequency corresponds to a separate sonar beam. Unlike traditional sonar designs that use dedicated electronics to form and steer the beams generated by each stave in the aray, e.g., [104], "this approach allows multiple independent beams to be simultaneously formed from a single hardware channel" [102].

Table 2.1. Sonar design parameters used to calculate noise-limited FOM.

	Sonar Design Parameters	Forward-Looking Sonar			Sidescan Sonar
		Cylindrical Array	Blazed Array		
Specified or Assumed	*Frequency*	200 kHz	450 kHz	900 kHz	900 kHz
	NominalRange	400 m	200 m	100 m	40 m
	Transmit Beam Widths				
	Horizontal	120°	90°	90°	0.4°
	Vertical	5°	10°	20°	40°
	Receive Beam Widths				
	Horizontal	2°	1°	1°	0.4°
	Vertical	2°	10°	20°	40°
	Pulse Length, T				
	FM	10 ms	10 ms	10 ms	—
	CW	—	—	—	6.67 μs
	Pulse Bandwidth, B				
	FM	80 kHz	80 kHz	80 kHz	—
	CW	—	—	—	150 kHz
	Detection Index, $5\log_{10} d$	10 dB	10 dB	10 dB	10 dB
	Detection Pings, $5\log_{10} n$	3 dB	3 dB	3 dB	3 dB
	Poisson Scan Rate, λ	0.2 scan/s	0.5 scan/s	1.0 scan/s	25 scan/s
Calculated	Attenuation Coefficient, a	52 dB/km	104 dB/km	287 dB/km	287 dB
	Directivity Index, DI				
	Transmit	16 dB	24 dB	24 dB	27 dB
	Receive	39 dB	24 dB	24 dB	27 dB
	Source Level, SL	197 dB	207 dB	206 dB	204 dB
	Ambient or Self-Noise, N	34 dB	41 dB	45 dB	44 dB
	Target Strength, TS	-30 dB	-30 dB	-30 dB	-30 dB
	Figure of Merit, *FOM*	**72 dB**	**66 dB**	**64 dB**	**49 dB**

In this section, we apply the procedure described in Section 2.6.1 to compute FOM values for two blazed array multibeam imaging sonars. Teledyne BlueView's P450 Series and

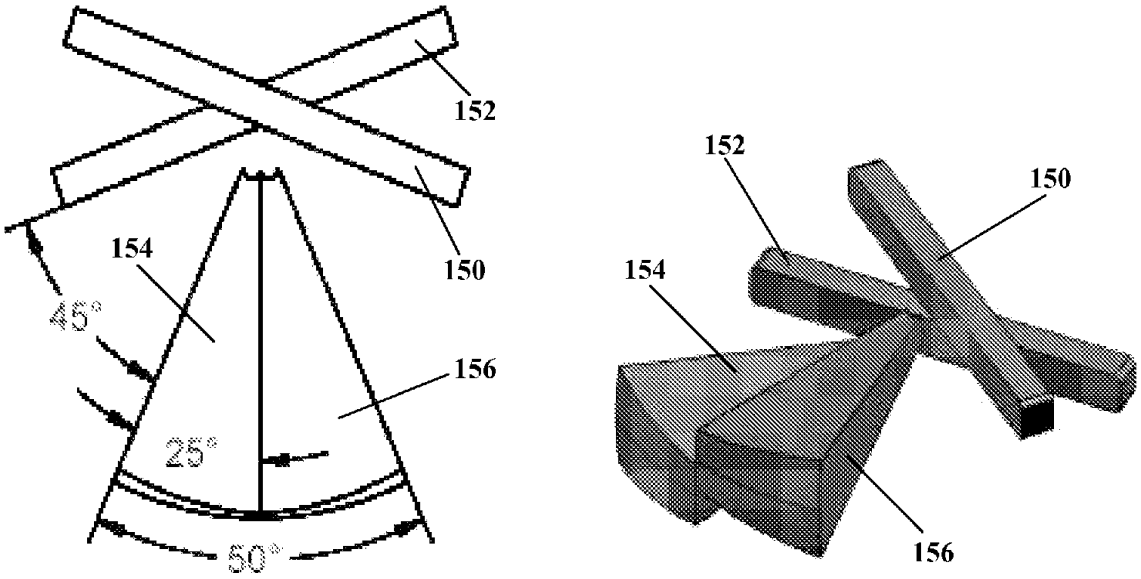

Figure 2.18. Combined beam pattern for a 50-degree horizontal field of view FLS constructed from two individual blazed arrays. Source: [105].

P900 Series systems are modular designs comprised of multiple blazed arrays that operate at 450 kHz and 900 kHz center frequencies, respectively. Figure 2.18 illustrates how individual staves can be combined to form a larger FOV. We will model the P450-90 and P900-90 sonars which utilize four staves to produce a 90-degree horizontal FOV.

An individual stave produces a 25-degree fan of beams in the image-plane, each with a distinct frequency and angle relative to the face of the stave. The lowest frequency beam angle is 45 degrees, and the highest frequency beam angle is 70 degrees, as shown in Figure 2.18 (left). The combined FOV for a two-stave system is depicted as a three-dimensional solid in Figure 2.18 (right), illustrating how the beam widths vary with frequency in both the image- and cross-image planes. Although beam pattern geometries for multi-stave systems like those depicted in [105] are complex, we assume that image processing algorithms allow us to model these sonars as conventional line arrays operating at the center frequency of their broadband pulse. Under this assumption, we can use manufacturer specifications for operating frequency, field of view, beam width (in the image- and cross-image planes), number of beams, and update rate to calculate a FOM for the P450-90 and P900-90 sonars [91]. We further assume that the these sonars use an FM pulse duration $T = 10$ ms.

Note that the manufacturer's specifications list the total number of beams in a given sonar. Since these sonars are constructed using modular staves, each with 128 individual beams, we compute the directivity index for a single stave using the expression for a baffled line array with $n = 128$ elements from Table 2.5 in [54]. For this sonar, the directivity index is

$$DI_t = DI_r = 3 + 10\log_{10} n = 3 + 10\log_{10}(128) = 24 \text{ dB}. \tag{2.27}$$

The transmit source levels for the P450-130 and P900-45 sonars are given in [106] as 207 dB and 206 dB, respectively. Using Equation (2.25) and the calculated value for $DI_t = 24$ dB, we can solve for a total acoustic power level P between 13 and 17 Watts, which is reasonable given that the stated electrical power consumption for these models is between 15 and 30 Watts.

Next, we use Equation (2.7) to compute attenuation coefficients for the 450 kHz and 900 kHz operating frequencies of $a = 104$ dB/km and $a = 287$ dB/km, respectively. From Equation (2.5) we estimate that the noise due to thermal agitation is $N_{therm} = 38$ dB and $N_{therm} = 44$ dB, respectively. After accommodating additional self-noise noise due to the vehicle platform (which has lesser impact at higher frequencies) we use conservative values of $N = 41$ dB and $N = 45$ dB, respectively.

Finally, we estimate the Poisson Scan rate for both sonar models by scaling the maximum update rate specified by the manufacturer. Assuming that these listed values apply to a sonar operating at its minimum optimal range, we scale the listed values by the nominal operating ranges used in our problem. For the P450-90 and P900-90 sonars, we estimate scan rates of $\lambda = 0.5$ and $\lambda = 1.0$ scans per second, respectively, based on nominal operating ranges of 200 and 100 meters. These values agree with practical update rates observed when deploying these sensors on a REMUS AUV. The parameters used to model the P450-90 and P900-90 blazed array sonars are listed in Table 2.1 alongside the parameters for the cylindrical FLS. The resulting FOM values calculated for these models are 66 dB and 64 dB, respectively.

2.7 Sidescan Sonar Model

Next, we estimate a figure of merit for a short-range, side-looking sonar similar to the sidescan sonar used on the NPS REMUS 100 AUV. This type of sensor is representative

of high-resolution sonars used to reacquire previously-detected MLOs and identify them for subsequent neutralization [13]. Following the design example for a SSS in Chapter 10 of [54], we use manufacturer specifications to derive a model for a 900 kHz sidescan sonar [92]. In contrast with the forward-looking sonars considered in Section 2.6, this sonar transmits a CW pulse with duration $T = 6.67$ μs and bandwidth $B = 1/T = 150$ kHz. It also has a very narrow horizontal FOV and a wide vertical FOV. As before, we can use the expression in Table 2.3 of [54] to compute the number of elements in a line array from its beamwidth $n = 100/BW = 100/0.4 = 250$. Substituting n into Equation (2.27), we calculate the directivity indices for the SSS's transmit/receive arrays: $DI_t = D_r = 27$ dB.

Assuming the sonar radiates 4 Watts of acoustic power, the source level for this sonar is $SL = 204$ dB, using Equation (2.25). The attenuation coefficient and thermal agitation noise are computed from the 900 kHz operating frequency as $a = 287$ dB/km and $N_{therm} = N = 44$ dB, respectively, since underwater platforms have much lower self-noise than surface craft. Because the ping rate of sidescan sonar is usually determined by the vehicle platform's speed and the sonar's range setting [107], we estimate a Poisson Scan rate for this sonar based on the two-way travel time of sound for a nominal operating range of 30 meters: $\lambda = \frac{1500 \text{ m/s}}{2(30 \text{ m})} = 25$ scans per second. The parameters used to model this 900 kHz SSS are listed in Table 2.1 and yield a FOM of 49 dB.

2.8 Model Verification and Validation

The sonar models developed in Section 2.6 and Section 2.7 were tested in simulation to verify their detection performance. The primary objective was to confirm whether a given sensor model's signal excess, FOV geometry, and Poisson Scan rate are accurately represented. For example, Figure 2.19 illustrates the sensor coverage obtained by a USV with 200 kHz FLS as it traveled through a square search area along the open loop trajectory shown. In this plot, the color map represents the probability that the searcher failed to detect a mine at each map location before the end of the mission. This probability of non-detection, $P_{ND}(T_f)$, conditioned over the entire search area, is our measure of MCM risk.

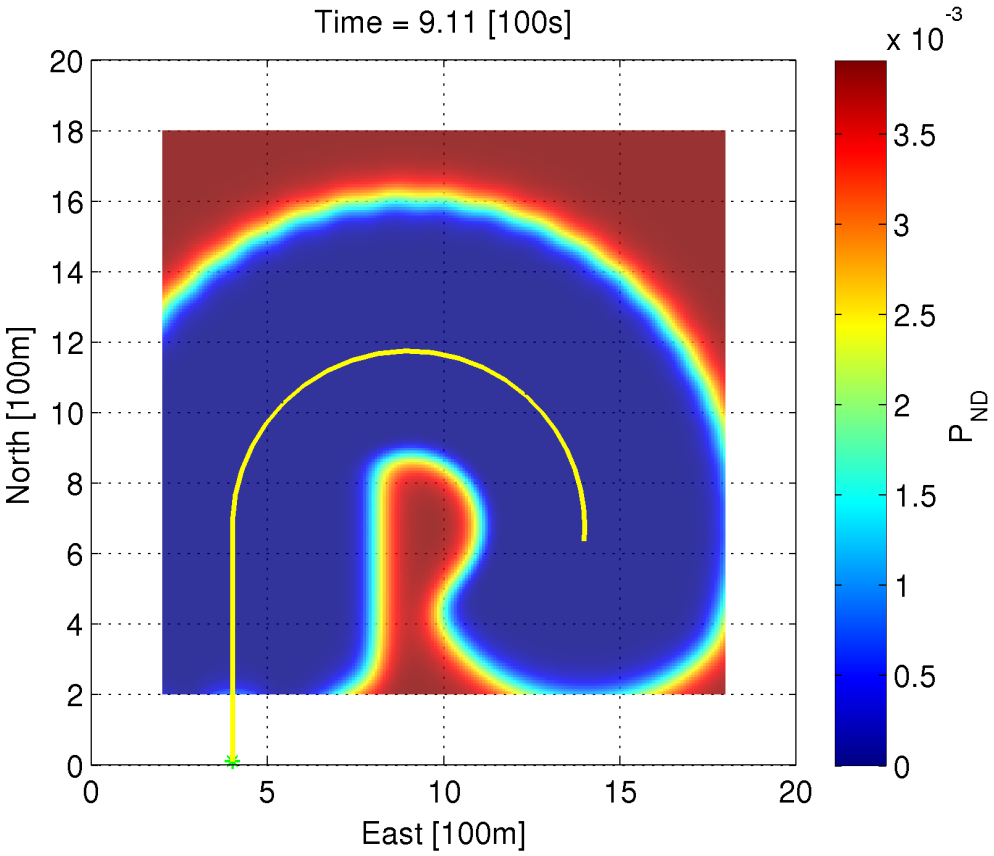

Figure 2.19. Simulated search with USV and forward-looking sonar.

Assuming that we have no prior information and that a mine can be uniformly placed anywhere within the search area, the maximum $P_{ND}(T_f)$ value (dark red) is a function of the search area size. In areas covered by the USV's sonar, $P_{ND}(T_f)$ approaches zero (blue), indicating a high probability of detecting a mine in those areas. We note the swath width produced by the sensor model is approximately equal to twice the nominal range, as expected.

A similar trajectory is shown for an AUV with sidescan sonar in Figure 2.20. To accommodate the slower AUV and shorter range sonar, the designated search area is much smaller than the FLS search area in Figure 2.19.

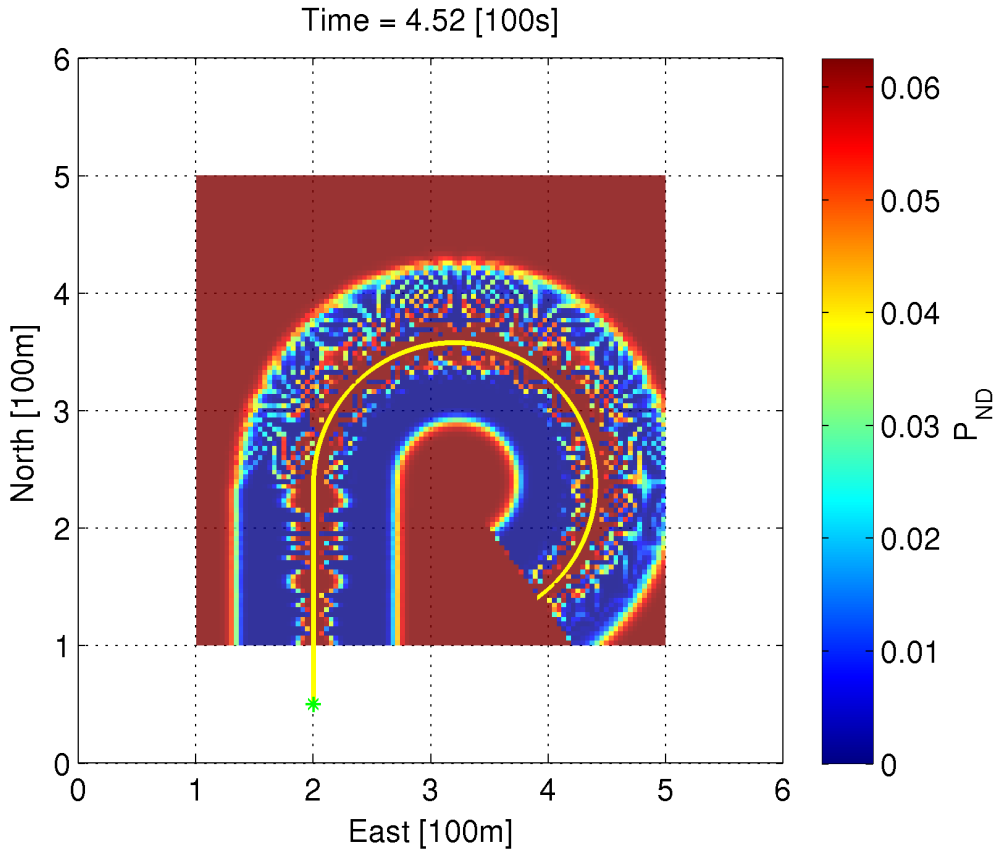

Figure 2.20. Simulated search with AUV and sidescan sonar.

As a result, the maximum values for $P_{ND}(T_f)$ are higher in a given area, a function of the uniform probability being spread over a smaller area. Nevertheless, the relative color scale indicates that our sidescan detection model is consistent with observed sidescan performance, namely it provides little to no coverage in the near-nadir region beneath the vehicle and performance is severely degraded when the vehicle turns.

In this chapter, we have defined detection models for several different active sonars, based on noise-limited signal excess. These models provide the instantaneous probability of detecting a target as a function of sonar design parameters, the figure of merit (FOM), and the range to the target, which determines propagation losses due to acoustic spreading and absorption. We then defined shaping functions which enforce a sonar's three dimensional geometry based on its horizontal and vertical FOV. After applying the azimuth and

elevation angle shaping functions, the Poisson Scan model is used to convert the instantaneous detection probability into a detection rate. Chapter 3 will formulate the optimal search problem as a GenOC problem, and utilize these sonar detection models to generate sensor-based motion plans to accomplish various MCM missions with different vehicles and sensors.

THIS PAGE INTENTIONALLY LEFT BLANK

CHAPTER 3:
Optimal Search Problem Formulation

In this chapter, we cast different mine countermeasures (MCM) operations as optimal search problems whose solutions yield motion plans for a team of autonomous vehicles. We specifically consider two MCM missions: 1) an initial wide area survey with long-range, low-resolution sonar to detect and locate MLOs, and 2) a subsequent mission to revisit these locations with high-resolution sonar for positive target identification. We formulate an objective function which can incorporate different searcher, sensor, and target distribution models to solve different MCM search problems in the GenOC framework, demonstrating its flexibility. The benefits of this approach are two-fold: solutions not only specify trajectories that each vehicle should execute for a given sensor payload, but also establish performance benchmarks for a given problem. The former can determine the most effective search pattern for a given vehicle or sensor, as discussed in Chapter 4. The latter provides a quantitative baseline for comparing different system configurations, which we explore in Chapter 5.

A number of vehicles and sensors are capable of performing the search tasks described above, but mission planners must consider which combinations are most effective for a given MCM operation. Often, the available vehicle platform dictates which sensors can be utilized, while a sensor may dictate the type of trajectory a vehicle must follow. We assume in this work that each vehicle deploys only one type of sonar, but acknowledge that some developmental systems can carry multiple sophisticated sonars at once [13], [108]. Another characteristic of search operations is that prior information (or the lack thereof) about potential target locations influences how the search is planned and executed. The GenOC framework includes all of these characteristics: multi-vehicle operations, sensor-based motion planning, and prior information. It can be customized to explore a wide variety of MCM scenarios simply by swapping different models of vehicle/sensor performance and initial target distribution.

The optimal search problem defined in this chapter assumes that:

- Targets are bottom mines with known target strength.
- Sea floor is flat.
- Water depth is constant.
- Search effort is confined to a rectangular area.
- Available mission time is fixed.

The following sections describe the mathematical models and the objective function used to solve MCM search scenarios within the GenOC framework.

3.1 Searcher Models

The search vehicles selected for a given mission place constraints on the admissible solutions to an optimal control problem. Specifically, we define a mathematical model for a vehicle's dynamic equations of motion. This model relates the vehicle's state variables $\vec{x}(t) \in \mathbb{R}^{N_x}$ and control inputs $\vec{u}(t) \in \mathbb{R}^{N_u}$ through a set of ordinary differential equations (ODEs) expressed in state-space form: $\dot{\vec{x}}(t) = \vec{f}(\vec{x}(t), \vec{u}(t))$. This model places dynamic constraints on how the states may evolve with time. Similarly, there may be algebraic constraints placed on the control inputs due to physical actuator limitations: $\vec{u}_{MIN} \leq \vec{u}(t) \leq \vec{u}_{MAX}$ for all $t \in [0, T_f]$. Additional constraints can be specified in order to bound the region of state space explored during optimization: $\vec{x}_{MIN} \leq \vec{x}(t) \leq \vec{x}_{MAX}$ for all $t \in [0, T_f]$. We note that for multi-vehicle problems with N_v searchers, the state and control vectors are simply expanded to include the states and controls of each vehicle, $\vec{x}(t) \in \mathbb{R}^{N_v N_x}$ and $\vec{u}(t) \in \mathbb{R}^{N_v N_u}$, respectively. The following sections describe models of two autonomous vehicles which are representative of naval platforms used for MCM.

3.1.1 SeaFox Unmanned Surface Vessel

The NPS SeaFox USVs are small, 5-meter rigid hull inflatable boats (RHIBs) originally designed for remote-controlled intelligence, surveillance, reconnaissance (ISR), force protection, and maritime interdiction operations (MIO) conducted by the USN and U.S. Coast Guard (USCG) [109], [110]. CAVR has converted these vessels into fully autonomous surface craft in support of various research programs, including sonar-based path planning for riverine navigation [111], [112] and precise speed control [113]. More recently,

CAVR modified its SeaFox Mk II USV to deploy an ATLAS minehunting FLS for MCM research [114].

To develop a model for these vehicles, we assume that USVs conduct MCM search missions at constant velocity, without aggressive maneuvers, and therefore exhibit simple planar motion at the sea surface (i.e., pitch, roll, and heave motions are zero). If we further assume that sway motions are negligible (i.e., sideslip is zero) the equations of motion can be adequately modeled by kinematics only. Using the state vector $\vec{x}(t) \equiv [x(t), y(t), \psi(t), r(t)]^T$, the state-space equations of motion (EOM) are:

$$\begin{aligned} \dot{x}(t) &= V\cos(\psi(t)) \\ \dot{y}(t) &= V\sin(\psi(t)) \\ \dot{\psi}(t) &= r(t) \\ \dot{r}(t) &= \frac{1}{T}\left(Ku(t) - r(t)\right). \end{aligned} \tag{3.1}$$

The state variable pair $[x(t), y(t)]$ defines the vehicle's position in meters along the north and east axes of the inertial reference frame; $\psi(t)$ describes the vehicle's heading angle in radians measured clockwise from the North axis; and $r(t)$ is the vehicle's turn rate in radians per second. The vehicle travels with constant forward velocity V meters per second, measured along the body-fixed x-axis. Equation (3.1) implements a first-order approximation to the well-known Nomoto model for ship steering equations, a simple transfer function between rudder angle $u(t) = \delta_r(t)$ and turn rate $r(t)$ that "is widely used for ship autopilot design due to its simplicity and accuracy" [115], [116]. The Nomoto gain constant K in inverse seconds, and time constant T in seconds can be identified from sea trial maneuvers as described in [117]–[119]. Table 3.1 lists the values of V, K, and T used in our SeaFox USV model.

Table 3.1. Design parameters for unmanned surface vessel model.

Design Parameter	SeaFox Value
Nomoto Gain Constant, K	0.5 1/s
Nomoto Time Constant, T	5.0 s
Velocity, V	2.5 m/s

3.1.2 REMUS 100 Autonomous Underwater Vehicle

The REMUS 100 AUV is a small, rapidly deployable unmanned underwater vehicle for collecting environmental data in the ocean [120]. Its modular design accommodates a number of different sensors for hydrographic survey missions, and its SSS system can make detailed maps of the ocean floor. One of the first AUVs adopted for naval MCM operations [82], [121], REMUS vehicles were used during Operation Iraqi Freedom in 2003 [122]. The REMUS family of vehicles includes two MCM variants in use by the Navy today: the MK 18 Mod 1 Swordfish, based on the 7.5-inch diameter REMUS 100, and the MK 18 Mod 2 Kingfish, based on the 12.75-inch diameter REMUS 600 [123]. CAVR operates three REMUS 100 AUVs in support of its research programs, and has been developing sensor-based navigation algorithms that utilize blazed array forward-looking sonar since 2004 [124]–[126].

Autonomous underwater vehicles can move in all three dimensions, and six degrees of freedom (DOF) are required to describe this motion completely. An example of a full 6-DOF model for simulating the nonlinear dynamics of a REMUS 100 is presented in [127]. In practice, however, these EOM are usually decoupled into separate, linearized equations in the horizontal and vertical planes so that designers can develop controllers for steering and diving, respectively. For our search problem, since AUVs typically conduct constant-velocity SSS surveys at a fixed altitude above the bottom, we consider only two-dimensional planar motion. Finally, as a matter of convenience when implementing multi-vehicle problems in software, we prefer a motion model with the same form as the SeaFox USV model in Section 3.1.1. This provides easier state vector indexing when AUVs and USVs operate in a heterogeneous vehicle team.

Under the same assumptions of zero pitch, roll, and heave motion, we can derive a Nomoto steering model for the REMUS 100 AUV from the linearized, decoupled, lateral steering

equations in Equation (118) of [127], repeated here:

$$\begin{bmatrix} m - Y_{\dot{v}} & -Y_{\dot{r}} & 0 \\ -N_{\dot{v}} & I_{zz} - N_{\dot{r}} & 0 \\ 0 & 0 & 1 \end{bmatrix} \begin{bmatrix} \dot{v}(t) \\ \dot{r}(t) \\ \dot{\psi}(t) \end{bmatrix} + \begin{bmatrix} -Y_v & mu_0 - Y_r & 0 \\ -N_v & -N_r & 0 \\ 0 & -1 & 0 \end{bmatrix} \begin{bmatrix} v(t) \\ r(t) \\ \psi(t) \end{bmatrix} = \begin{bmatrix} Y_{\delta_r} \\ N_{\delta_r} \\ 0 \end{bmatrix} \delta_r(t) \tag{3.2}$$

where $u_0 =$ steady-state surge velocity in the x-direction,

$v(t) =$ sway velocity in the y-direction,

$m =$ vehicle's mass,

$I_{ZZ} =$ vehicle's yaw moment of inertia about the z-axis,

$Y =$ linear hydrodynamic coefficients producing sway forces, and

$N =$ linear hydrodynamic coefficients producing yaw moments.

In general, control inputs and state variables (and their derivatives) produce nonlinear hydrodynamic forces and moments. It is common practice, however, to approximate these effects by multiplying each contributing variable with a linearized hydrodynamic coefficient. In Equation (3.2), Y and N denote coefficients that produce sway forces and yaw moments, respectively, while subscripts denote their corresponding control input or state variable. Assuming that sway velocity is zero (no sideslip), we rearrange Equation (3.2) as

$$\begin{aligned} \begin{bmatrix} I_{zz} - N_{\dot{r}} & 0 \\ 0 & 1 \end{bmatrix} \begin{bmatrix} \dot{r}(t) \\ \dot{\psi}(t) \end{bmatrix} + \begin{bmatrix} -N_r & 0 \\ -1 & 0 \end{bmatrix} \begin{bmatrix} r(t) \\ \psi(t) \end{bmatrix} &= \begin{bmatrix} N_{\delta_r} \\ 0 \end{bmatrix} \delta_r(t) \\ \begin{bmatrix} (I_{zz} - N_{\dot{r}})\,\dot{r}(t) - N_r r(t) \\ \dot{\psi}(t) - r(t) \end{bmatrix} &= \begin{bmatrix} N_{\delta_r} \\ 0 \end{bmatrix} \delta_r(t) \\ \begin{bmatrix} (I_{zz} - N_{\dot{r}})\,\dot{r}(t) \\ \dot{\psi}(t) \end{bmatrix} &= \begin{bmatrix} N_r r(t) + N_{\delta_r} \delta_r(t) \\ r(t) \end{bmatrix}. \end{aligned} \tag{3.3}$$

Manipulating the $\dot{r}(t)$ expression from Equation (3.3) into the form of our first order Nomoto steering model (see Equation (3.1)), we have

$$\begin{aligned}
(I_{zz} - N_{\dot{r}})\,\dot{r}(t) &= N_r r(t) + N_{\delta_r}\delta_r(t) \\
\dot{r}(t) &= \frac{N_r}{(I_{zz} - N_{\dot{r}})} r(t) + \frac{N_{\delta_r}}{(I_{zz} - N_{\dot{r}})}\delta_r(t) \\
\dot{r}(t) &= \frac{1}{T}\left[Ku(t) - r(t)\right], \\
\text{where: } T &= \frac{N_{\dot{r}} - I_{zz}}{N_r}, \\
K &= -\frac{N_{\delta_r}}{N_r}, \text{ and} \\
u(t) &= \delta_r(t).
\end{aligned} \tag{3.4}$$

Substituting values from [127] for the yaw axis moment of inertia I_{zz} and the hydrodynamic coefficients $N_{\dot{r}}$, N_r, and N_{δ_r} (using the SeaFox sign convention), we calculate the parameters for our REMUS 100 model listed in Table 3.2.

Table 3.2. Design parameters for autonomous underwater vehicle model.

Design Parameter	REMUS 100 Value
Nomoto Gain Constant, K	2.0 1/s
Nomoto Time Constant, T	1.0 s
Velocity, V	1.5 m/s

Since our MCM scenario concerns the search for bottom mines, the altitude h must also be specified for a given vehicle's mission. For surface craft, altitude h equals the water depth under our flat bottom, constant depth assumptions.

3.2 Sensor Models

Physics-based models for different types of active sonar used in MCM were developed in Chapter 2. These models calculate the instantaneous probability p that a given sonar can detect an echo from a specific target against the expected ambient noise level. This quantity is a function of the sonar design, parameterized by its *FOM*, and the two-way

propagation losses PL between the sonar and target when a scan occurs. At these scan times, the instantaneous detection probability also depends on whether the target lies within the sonar's three dimensional FOV, a function of sonar geometry and vehicle trajectory $\vec{x}(t)$. Three scalar shaping functions were designed to characterize these relationships: F_α, F_ε, and F_r. For a given sonar, this process occurs at an average rate λ, producing the instantaneous detection rate γ defined in Equation (2.22). Including the terms described above yields

$$\begin{aligned}\gamma(\vec{x}(t),\vec{\omega}) &= \lambda F_\alpha(\vec{x}(t),\vec{\omega})F_\varepsilon(\vec{x}(t),\vec{\omega})F_r(\vec{x}(t))p(\vec{x}(t),\vec{\omega}) \\ &= \lambda F_\alpha(\vec{x}(t),\vec{\omega})F_\varepsilon(\vec{x}(t),\vec{\omega})F_r(\vec{x}(t))\Phi\left(\frac{SE\left(\vec{x}\left(t\right),\vec{\omega}\right)}{\sigma}\right) \\ &= \lambda F_\alpha(\vec{x}(t),\vec{\omega})F_\varepsilon(\vec{x}(t),\vec{\omega})F_r(\vec{x}(t))\Phi\left(\frac{FOM - PL\left(\vec{x}\left(t\right),\vec{\omega}\right)}{\sigma}\right). \end{aligned} \tag{3.5}$$

The expressions used to compute each term in Equation (3.5) are listed in Table 3.3.

Table 3.3. Terms used to compute instantaneous detection rate.

Symbol	Definition	Cross Reference
λ	Poisson Scan Rate	Section 2.4
SE	Signal Excess	Equation (2.3)
FOM	Figure of Merit	Equation (2.4)
PL	Propagation Loss	Equation (2.6)
p	Probability of Detection	Equation (2.8)
F_α	Azimuth Shaping Function	
	forward-looking sonar	Equation (2.15)
	sidescan sonar	Equation (2.19)
F_ε	Elevation Shaping Function	Equation (2.16)
F_r	Turn Rate Shaping Function	Equation (2.21)

3.3 Target Models

The GenOC framework was developed to address optimal control problems with parameter uncertainty [5], [10], [11]. For the MCM search problems considered in this disserta-

tion, the uncertain parameter is the location of a mine target on the sea floor. We assume, therefore, that target location is a stochastic parameter $\vec{\omega}$ distributed over a search area Ω according to a known continuous PDF: $\phi(\vec{\omega}) : \Omega \mapsto \mathbb{R}$. That is, $\vec{\omega} \in \Omega \subset \mathbb{R}^{N_\omega}$ [5], and $N_\omega = 2$. We can model a number of possible target distributions by specifying a different PDF, and this directly influences the solution of the optimal search problem.

We can use different target distribution models to simulate various MCM missions. In the initial phase of an MCM operation, for example, wide-area surveys are conducted to detect and localize MLOs in a given search area. We formulate this task as an optimal search problem where no prior target data is available. We therefore model the target distribution with a joint uniform PDF, bounded by the search area coordinates. This PDF contains no exploitable information, i.e., there is an equal probability of finding a target anywhere within the search area.

In subsequent phases of an MCM operation, additional sorties are conducted to reacquire previously detected MLOs and identify mines from non-mine/mine-like bottom objects (NOMBOs) using high-resolution sonar. We can formulate this RID task as another optimal search problem which not only incorporates different vehicle and sensor models, but also leverages MLO location data gathered during a prior survey. The accuracy of prior information is commensurate with the navigational performance of the survey vehicle, so we model this variation with a PDF. Any continuous PDF can be specified. Walton, however, suggests the use of joint normalized beta distributions for modeling purposes, due to their easy algebraic manipulation and customization (via the α, β shape parameters), as well as their finite radius of effectiveness [79]. The PDF for the beta distribution, defined for $x \in [0,1]$, $\alpha > 0$, and $\beta > 0$ [128] is

$$\phi(x;\alpha,\beta) = \frac{1}{B(\alpha,\beta)} x^{\alpha-1}(1-x)^{\beta} - 1, \tag{3.6}$$
$$\text{where } B(\alpha,\beta) = \frac{(\alpha-1)!(\beta-1)!}{(\alpha+\beta-1)!}.$$

3.4 Objective Function

In this section we present the exponential detection model, first described in [36], which is commonly used to quantify search performance in continuous time. Based on a sensor's instantaneous detection rate (see Section 2.4), this model provides a convenient objective function for optimal search problems, with recent examples provided in [5], [6], [11]. For our problem, we define *residual MCM risk* as the probability that a team of autonomous vehicles fails to detect the mines in a search area by the end of an MCM operation. This scalar quantity can be readily calculated for a given set of vehicle and sonar capabilities, and also reflects the time available for search. Therefore, we utilize MCM risk as the objective function for our optimal search problems; minimizing this quantity maximizes the mission's probability of success.

Given an instantaneous detection rate $\gamma(t)$, derivation of the exponential detection model proceeds from two key assumptions [36]:

1. The probability of detection in the short time interval $[t, t + \Delta t]$ is $\gamma(t)\Delta t$.
2. Detection events in all such non-overlapping time intervals are independent.

Washburn cautions that the independence assumption may not hold in all situations. For example, consecutive detection failures due to low signal excess could be caused by low target strength or poor acoustic conditions. Empirically, however, these assumptions "provide good approximations in a wide variety of circumstances" [51]. Koopman acknowledges the importance of recognizing when this assumption is legitimate or not, and justifies its use beyond cases of random search:

> The assumption is in fact legitimate—and important—when applied to *conditional probabilities* of detection: probabilities calculated on the basis of *postulated* positions and motions of the target. [37]

This is precisely the case described by our objective function for MCM risk in Equation (3.11), which we now derive using Koopman's "assumption of independence."

Let $p(t)$ be the probability of detection at time t. Then, by the complement, the probability of a detection *failure* is $q(t) = 1 - p(t)$. Under our stated assumptions, this probability becomes $q(t + \Delta t) = q(t)(1 - \gamma(t)\Delta t)$ at the end of the next scan interval, which can be

rearranged as the difference equation:

$$\frac{q(t+\Delta t)-q(t)}{\Delta t} = -q(t)\gamma(t). \tag{3.7}$$

In the limit as $\Delta t \to 0$, we obtain the differential equation

$$\dot{q}(t) = -q(t)\gamma(t), \tag{3.8}$$

which has the closed form solution

$$q(t) = e^{-\int_0^t \gamma(\tau)d\tau}, \tag{3.9}$$

and leads to the exponential detection model: $p(t) = 1 - q(t) = 1 - e^{-\int_0^t \gamma(\tau)d\tau}$.

Equation (3.9) represents the probability that a target was not detected by time t, so the residual MCM risk after completing an operation of mission duration T_F is:

$$q(T_F) = e^{-\int_0^{T_F} \gamma(\tau)d\tau}. \tag{3.10}$$

The objective of our optimal search problem is to minimize this risk. However, the instantaneous detection rate in Equation (3.5) depends on the vehicle trajectory $\vec{x}(t)$ and the uncertain target location $\vec{\omega}$, a random variable defined in Section 3.3. Consequently, Equation (3.10) is itself a random variable, which we cannot minimize explicitly. Instead, we must minimize its expected value, conditioned on the PDF of the target distribution. Hence, the objective function for a single vehicle becomes

$$J = \mathbb{E}\left\{q(T_F)\right\} = \int_\Omega e^{-\int_0^{T_F} \gamma\left(\vec{x}(\tau),\,\vec{\omega}\right)d\tau}\phi(\vec{\omega})d\vec{\omega}. \tag{3.11}$$

For missions with multiple searchers, we assume that instantaneous detection rates are additive, but vehicle- and sensor-specific. For example, the combined detection rate for a team comprised of N_v vehicles is

$$\Gamma(\vec{x}(t),\vec{\omega}) = \sum_{k=1}^{N_v} \lambda^k F_\alpha^k(\vec{x}(t),\vec{\omega}) F_\varepsilon^k(\vec{x}(t),\vec{\omega}) F_r^k(\vec{x}(t))\Phi\left(\frac{FOM^k - PL\left(\vec{x}\,(t)\,,\vec{\omega}\right)}{\sigma^k}\right). \tag{3.12}$$

The additive rate in Equation (3.12) makes the implicit assumption that multiple sonars do not acoustically interfere with one another. This assumption is rarely realistic, except when sonar systems have widely-separated design frequencies or when they are deployed in different locations, but this can be addressed during mission planning by imposing minimum separation distances. Interestingly, the exponential detection model often produces multi-vehicle motion plans which resemble manually-separated vehicle trajectories. Since this model yields diminishing returns when multiple vehicles search the same location [51], it tends to encourage multi-vehicle solutions which distribute search effort to explore new regions of the search space. Under our assumptions, the expected residual MCM risk after a multi-vehicle operation is

$$J^{N_v} = \int_{\Omega} e^{-\int_0^{T_F} \Gamma(\vec{x}(\tau),\, \vec{\omega}) d\tau} \phi(\vec{\omega}) d\vec{\omega}. \tag{3.13}$$

The objective functions in Equations (3.11) and (3.13) are differentiable, analytic expressions. Although somewhat tedious, it is possible to derive formulas for their gradients with respect to the state and control variables. This has benefits when using gradient-based numerical optimization algorithms. Encoding these formulas as user-defined functions supplied to the SNOPT optimization package, for example, significantly reduces the run time required to compute an optimal solution [99]. The objective function gradients for a single vehicle are derived in Appendix A.

We observe that our objective functional J, representing the expected residual MCM risk, has the same form as the running cost in Equation (1.2), the objective functional of the GenOC problem discussed in Chapter 1. This objective functional is repeated here for comparison with Equations (3.11) and (3.13):

$$J = \int_{\Omega} E\left(\vec{x}(T_f), \vec{\omega}\right) + G\left(\int_0^{T_f} R\left(\vec{x}(\tau), \vec{u}(\tau), \tau, \vec{\omega}\right) d\tau\right) \phi(\vec{\omega}) d\vec{\omega}. \tag{3.14}$$

The end-point cost $E\left(\vec{x}(T_f),\, \vec{\omega}\right)$ in Equation (3.14) has been omitted from our objective functions. Meanwhile, the function $G(\cdot)$ of the running cost derives from the exponential detection model, i.e., $G(\cdot) = e^{-(\cdot)}$, and $R(\cdot) = \gamma(\cdot)$. The objective functional in Equation (3.14) has been used to solve optimal search problems with multiple searchers and moving targets in cases where target motion can be conditionally-determined by uncertain

initial conditions [5], [7], [81]. Using similar objective functions in Equations (3.11) and (3.13) allows us to leverage the mathematical and computational framework previously developed to handle this class of parameter-distributed, nonlinear optimal control problems. A contribution of this dissertation, therefore, is the development of new physics-based sonar models which allow the GenOC solution framework to address real-world MCM mission planning and analysis problems.

3.5 Problem Scaling

We need to solve these optimal search problems numerically, but the domains of our state variables $x(t)$, control inputs $u(t)$, uncertain parameters $\vec{\omega}$, and objective function J all have different orders of magnitude. The search area, for example, may cover several square kilometers, while the objective function evaluates to a probability in the range $[0, 1]$. It is important, therefore, to properly scale the problem before unleashing a numeric solver. This can be achieved by defining canonical units for distance, time, etc. and transforming the original problem's variables into non-dimensional versions with similar domains [2]. Several examples which use variable scaling to numerically balance the equations of an optimal control problem are provided in [74].

For our search problems, the vehicle models from Section 3.1 can be scaled by canonical units of distance DU, time TU, and velocity $VU = DU/TU$ to produce dimensionless variables designated by overbar notation:

$$\begin{aligned}
\overline{x} &= \frac{x}{DU} \\
\overline{y} &= \frac{y}{DU} \\
\overline{\psi} &= \psi \\
\overline{r} &= \frac{r}{1/TU} = (TU)r \\
\overline{t} &= \frac{t}{TU} \\
\overline{u} &= u.
\end{aligned} \tag{3.15}$$

Note that angular variables for heading ψ and control input u (rudder angle) are already expressed in dimensionless units of radians. The chosen scaling must also be applied to

constant model parameters such as velocity V, as well as the gain K and time T constants of the Nomoto steering model:

$$\begin{aligned}\overline{V} &= \frac{V}{VU} \\ \overline{K} &= \frac{K}{1/TU} = (TU)K \\ \overline{T} &= \frac{T}{TU}.\end{aligned} \tag{3.16}$$

Substituting these expressions into our original expressions for x and y yields their state space equations in nondimensional units:

$$\begin{aligned}\dot{x} &= \frac{dx}{dt} = \frac{d(DU\overline{x})}{d(TU\overline{t})} = \frac{DU}{TU}\frac{d\overline{x}}{d\overline{t}} = VU\dot{\overline{x}} \\ \dot{\overline{x}} &= \frac{1}{VU}\dot{x} = \frac{1}{VU}V\cos(\psi) = \overline{V}\cos(\overline{\psi}).\end{aligned} \tag{3.17}$$

Similarly, we have

$$\dot{\overline{y}} = \overline{V}\sin(\overline{\psi}). \tag{3.18}$$

Likewise, scaling by canonical units for ψ and r yields the non-dimensional expressions

$$\begin{aligned}\dot{\psi} &= \frac{d\psi}{dt} = \frac{d\overline{\psi}}{d(TU\overline{t})} = \frac{1}{TU}\frac{d\overline{\psi}}{d\overline{t}} = \frac{1}{TU}\dot{\overline{\psi}} \\ \dot{\overline{\psi}} &= TU\dot{\psi} = (TU)r = \overline{r}, \text{ and} \\ \dot{r} &= \frac{dr}{dt} = \frac{d(1/TU)\overline{r}}{d(TU\overline{t})} = \frac{1}{TU^2}\frac{d\overline{r}}{d\overline{t}} = \frac{1}{TU^2}\dot{\overline{r}} \\ \dot{\overline{r}} &= (TU^2)\dot{r} = (TU^2)\frac{1}{T}\left(Ku - r\right)\end{aligned} \tag{3.19}$$

$$\begin{aligned}&= (TU^2)\frac{1}{TU\overline{T}}\left(\frac{\overline{K}}{TU}\overline{u} - \frac{\overline{r}}{TU}\right) \\ &= \frac{1}{\overline{T}}\left(\overline{K}\overline{u} - \overline{r}\right).\end{aligned} \tag{3.20}$$

Equations (3.17) through (3.19) confirm that our scaling has not changed the underlying dynamics of the problem. To ensure the objective function J is calculated properly, physical

units in the detection rate equation must also be scaled by the appropriate canonical units. The Poisson Scan rate λ is scaled using TU to yield the non-dimensional form

$$\overline{\lambda} = \frac{\lambda}{1/TU} = (TU)\lambda. \tag{3.21}$$

Recall from Equation (2.6) that our range-dependent propagation loss includes a spherical spreading term, $20\log_{10}(\|\vec{\omega} - \vec{x}(t)\|)$, and an acoustic absorption term $a\|\vec{\omega} - \vec{x}(t)\|$. At each time t we can compute the distance D between a vehicle and target. Scaling this distance yields:

$$\begin{aligned}
D &= \|\vec{\omega} - \vec{x}\| \\
D &= \sqrt{(\omega_x - x)^2 + (\omega_y - y)^2 + (\omega_z - z)^2} \\
D &= \sqrt{(dx)^2 + (dy)^2 + (dz)^2} \qquad (3.22) \\
D &= \sqrt{(DU\overline{dx})^2 + (DU\overline{dy})^2 + (DU\overline{dz})^2} \\
D &= DU\sqrt{\overline{dx}^2 + \overline{dy}^2 + \overline{dz}^2} \\
D &= DU\overline{D}. \qquad (3.23)
\end{aligned}$$

So $\overline{D} = D/DU$, as expected. The attenuation coefficient a has units of dB/m and must be scaled by canonical distance DU (dB represents a ratio and is dimensionless already) as

$$\overline{a} = \frac{a}{1/DU} = (DU)a. \tag{3.24}$$

Finally, the propagation loss calculated using these dimensionless quantities becomes

$$PL = 20\log_{10}(D) + a(D) \tag{3.25}$$

$$\begin{aligned}
PL &= 20\log_{10}\left(DU\overline{D}\right) + \frac{\overline{a}}{DU}\left(DU\overline{D}\right) \\
PL &= 20\log_{10}(DU) + 20\log_{10}\left(\overline{D}\right) + \overline{a}\left(\overline{D}\right), \qquad (3.26)
\end{aligned}$$

which has an additional term due to the distance scale factor. The level curves in Figure 3.1 verify that propagation loss calculated for non-dimensional ranges with Equation (3.26) and $DU = 100$ meters (shown at right) are equivalent to propagation loss calculated for

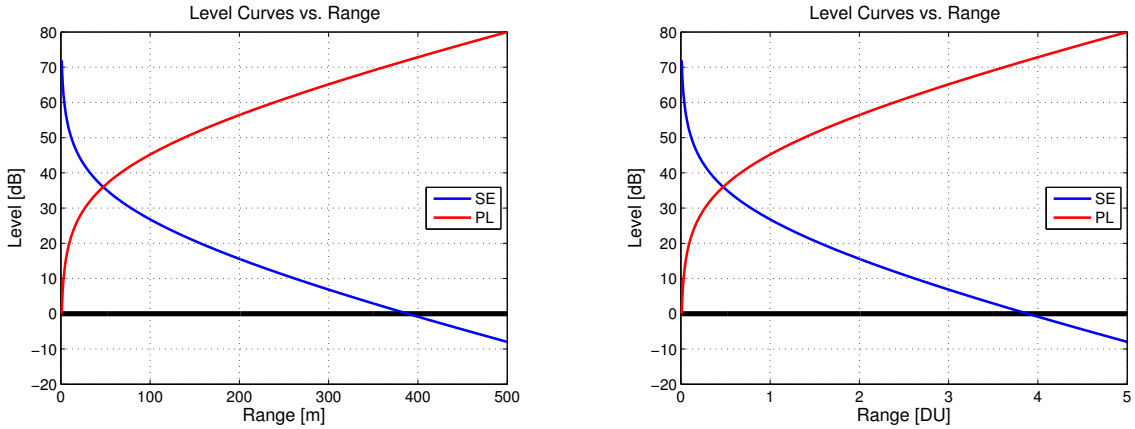

Figure 3.1. Propagation loss vs. physical range (left) and non-dimensional range (right) for 200 kHz FLS with figure of merit of 72 dB.

physical ranges with Equation (3.25) (shown at left). These curves also show the signal excess vs. range for the 200 kHz FLS with FOM = 72 dB, derived in Section 2.6.1. Note that signal excess is zero at a range of 400 meters. As an example, suppose we want to solve an MCM search problem for the SeaFox USV (see Section 3.1.1) conducting a mine detection survey with the 200 kHz FLS above. Typical bounds on the states, controls, search area, and constant parameters are defined in Table 3.4. This table includes their physical values (before scaling), and their non-dimensional values after scaling by the canonical units $DU = 100$ meters, $TU = 100$ seconds, and $VU = \frac{DU}{TU} = 1$ m/s.

3.6 Feasibility

Most optimal control problems cannot be solved analytically. Often, numerical methods are required to generate "optimal" trajectories of the state variables and control inputs that minimize a desired objective function, subject to constraints defined by the user. We must remember, however, that numeric solutions are calculated for a *discretized* version of the original problem. They meet the mathematical definition of feasibility as long as all of the problem constraints are satisfied at a finite number of nodes comprising the discrete problem [129]–[131].

Table 3.4. Example of physical and non-dimensional parameter domains.

Parameter	Physical Domain		Canonical Domain
Time	$0 \leq t \leq 1800$	s	$0 \leq \overline{t} \leq 18$
Search Area North Coordinate	$500 \leq \omega_x \leq 2500$	m	$5 \leq \overline{\omega}_x \leq 25$
Search Area East Coordinate	$500 \leq \omega_y \leq 2500$	m	$5 \leq \overline{\omega}_y \leq 25$
North Coordinate	$0 \leq x \leq 3000$	m	$0 \leq \overline{x} \leq 30$
East Coordinate	$0 \leq y \leq 3000$	m	$0 \leq \overline{y} \leq 30$
Heading	$-\infty \leq \psi \leq \infty$	rad	$-\infty \leq \overline{\psi} \leq \infty$
Turn Rate	$-0.3 \leq r \leq 0.3$	rad/s	$-30 \leq \overline{r} \leq 30$
Rudder Angle Input	$-0.5 \leq u \leq 0.5$	rad	$-0.5 \leq \overline{u} \leq 0.5$
Velocity	$V = 2.5$	m/s	$\overline{V} = 2.5$
Nomoto Gain Constant	$K = 0.5$	1/s	$\overline{K} = 50$
Nomoto Time Constant	$T = 5.0$	s	$\overline{T} = 0.05$
Poisson Scan Rate	$\lambda = 0.2$	1/s	$\overline{\lambda} = 20$
Attenuation Coefficient	$a = 0.052$	dB/m	$\overline{a} = 5.2$

It is important to verify that these constraints are, in fact, satisfied in the continuous domain as well. Moreover, we require optimal trajectories that can be implemented on autonomous vehicles. Therefore, as a practical consideration, we adopt the definition of feasibility used by Hurni:

> Showing the feasibility of the generated solution can be done by control trajectory interpolation and state propagation using a Runge-Kutta algorithm. If the initial conditions and system dynamics can be propagated using the optimal control solution and it matches the [solver's] generated trajectories, then the control solution is deemed feasible. [74]

In other words, solutions with discrete trajectories $\{\vec{x}(k),\ \vec{u}(k)\}$ are feasible if a vehicle can execute a smooth control trajectory $\vec{u}(t)$, interpolated through the solution's $\vec{u}(k)$ nodes, and produce a state trajectory $\vec{x}(t)$ sufficiently close to the solution's $\vec{x}(k)$ nodes. Planning algorithms can verify feasibility automatically, but the word "close" must be quantified first. Possible metrics for the similarity between two curves include the Frechet [132] or

Hausdorff [133] distance measures. The trajectory-planning algorithm proposed in [74], for example, performs automatic feasibility checks using a norm based on summing the Euclidean distances between the solution nodes and points along the propagated trajectory, evaluated at the solution nodes. In the following chapters, we will consider a solution to be feasible when its state-propagated trajectory a) does not violate problem constraints, and b) matches the solution trajectory when overlaid on a graphical plot. These criteria will verify that solutions obtained from a numeric solver are feasible, and also ensure that only feasible guesses are used to initialize the optimization. When necessary, e.g., for the automated analysis of inverse problems conducted in Chapter 5, we employ a numeric feasibility criteria similar to [74].

3.7 Initial Guess

Most numeric optimization routines are initialized with an initial guess. For an optimal control problem, the guess is a candidate solution, complete with state and control trajectories $\{\vec{x}(k), \vec{u}(k)\}$ at discrete time nodes. The solver evaluates the objective function using these trajectories. From there, it iteratively generates new candidate solutions that decrease the objective value, finally stopping its search when it reaches a local minimum. A good initial guess can influence the optimization by focusing the solver's effort in smaller regions of the search space. As a result, initial guesses can dramatically reduce solution times [74]. In some cases, e.g., when a problem has several local minima, the initial guess can determine whether a solver succeeds or fails at finding the correct solution.

The initial guess must be a valid candidate solution to the optimization problem, which implies that the initial guess should:

- have the same initial condition $\vec{x}(0) = \vec{x}_0$ as the problem of interest,
- have the same time node discretization as the problem of interest, and
- be feasible, i.e., obey state variable constraints and control limits.

The first two requirements are easy to address while encoding the problem of interest into the GenOC framework. Satisfying the feasibility requirement depends on the sophistication of the initial guess trajectory, which corresponds to the amount of prior information we wish to incorporate. Ideally, we would like to find an optimal solution without knowing beforehand what a "good" initial guess looks like. A trivial guess which satisfies the

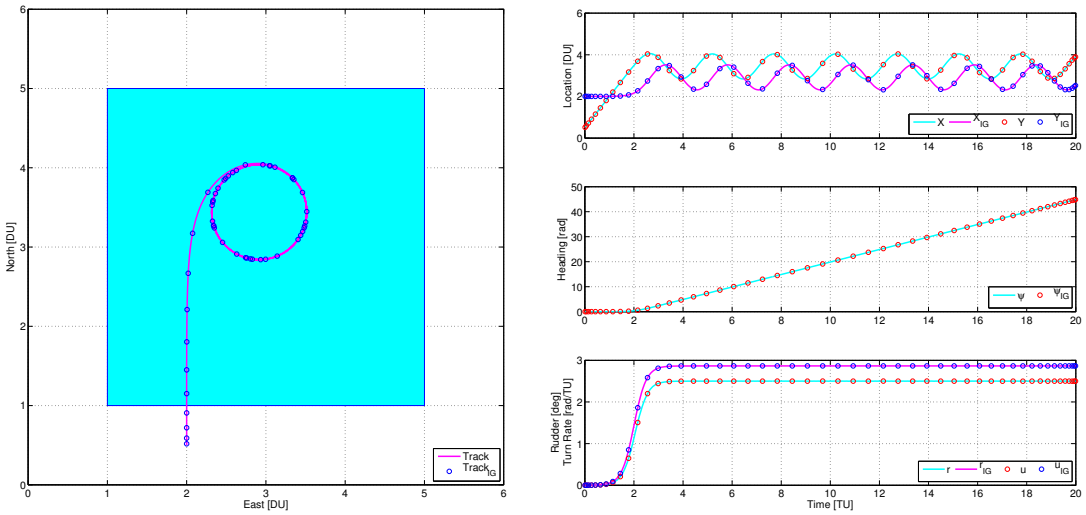

Figure 3.2. Initial guess trajectories for open loop rudder step.

first two requirements, for example, would be a zero velocity trajectory that remains at $\vec{x}_0$ for all time. Unfortunately, the constant velocity vehicle models defined in Section 3.1 do not permit acceleration, and the solver would be unable to find another solution trajectory. Similarly, a guess which specifies a trivial control trajectory $u(t) = 0$ for all time is infeasible under our definition, because the vehicle would travel at constant velocity and heading until it left the domain of its North or East coordinate.

A naive open-loop control trajectory is a good compromise between a trivial (no information provided) guess, and an expert (full information provided) guess. For example, a rudder angle step function, executed at the proper time, will cause a search vehicle to turn in a circle until the end of the simulation. This has the benefit of keeping the vehicle in the search area and ensures that state variable limits are not exceeded. In practice, we approximate a discrete step function with a smooth sigmoidal curve centered at the step time [96]. This simple control trajectory is then propagated through the motion model, using a Runge-Kutta algorithm (e.g., the MATLAB ode45 solver) to calculate the corresponding state variable trajectories, thereby guaranteeing feasibility (see Figure 3.2).

If there is sufficient time to exhaustively search an area, an expert initial guess can be provided that completely covers the area with a deterministic search pattern. A num-

ber of algorithms for "coverage path planning" exist [63], based on sensor sweep width. Deterministic search patterns include spirals for searching circular areas [72]; and box-spirals, lawnmower, or zamboni patterns for searching rectangular areas [134]. While these strategies may waste effort when the search area contains sub-regions with near-zero target probability distribution [135], it is usually possible to decompose the search area into smaller regions and avoid this situation. Moreover, for rectangular search areas, line sweeps conducted parallel to boundary edges are optimal for minimizing the number of turns required [66]. This fact, plus the ease of implementing these patterns with vehicle autopilots, likely explain the widespread use of lawnmower patterns for underwater search operations.

These rectangular coverage patterns require path-following controllers to execute them. Coverage path planners often take this for granted, assuming that the search area can be decomposed into smaller, "easy to cover" cells; the vehicle need only visit all such cells to achieve complete coverage [63]. Another approach is to extend the line sweep track length by a vehicle-specific distance, assuming all 180-degree turns occur outside the search area and the vehicle re-establishes straight-line motion before reentry on an adjacent track [136]. While these approaches determine the geometric length, spacing, and number of track lines for a given sweep width, they do not represent feasible trajectories, per se.

Before we can specify this type of coverage pattern as an initial guess for an optimal control problem, we need to convert a waypoint-based specification into a feasible trajectory. Haugen suggests an approach for constructing a feasible lawnmower path which uses clothoids as transition curves between waypoint segments. The clothoids are scaled such that a vehicle following this trajectory obeys feasibility constraints on its angular velocity and acceleration [137]. Depending on the track spacing and vehicle turning radius, one of three different U-turn paths are constructed to connect adjacent line sweep tracks. For our search problems, we assume that the lawnmower track spacing permits a piecewise U-turn comprised of two 90-degree clothoids and a straight line segment (Case A) [137]. This produces a feasible path in the horizontal plane, which we can convert to a control trajectory $u(k)$ by

inverting the searcher model of Section 3.1 as follows:

$$\begin{aligned}
\Delta x(k) &= x(k+1) - x(k) \\
\Delta y(k) &= y(k+1) - y(k) \\
\psi(k) &= \text{atan2}\left(\Delta y(k),\, \Delta x(k)\right) \\
\Delta t(k) &= \frac{\sqrt{\Delta x^2(k) + \Delta y^2(k)}}{V} \\
r(k) = \frac{d\psi}{dt}(k) &\approx \frac{\psi(k+1) - \psi(k)}{\Delta t(k)} \\
\dot{r}(k) = \frac{dr}{dt}(k) &\approx \frac{r(k+1) - r(k)}{\Delta t(k)} \\
u(k) &= \frac{1}{K}\left(r(k) + T\dot{r}(k)\right).
\end{aligned} \tag{3.27}$$

Figure 3.3 and Figure 3.4 illustrate lawnmower and box-spiral initial guesses, respectively, constructed using this clothoid method. Note that the inverse kinematic equations of Equation (3.27) differentiate state trajectories using the forward Euler method, which requires small, equally-spaced time steps to ensure accuracy and feasibility of the derivatives. Small step size translates into a large number of nodes, which can drastically increase solver run time. The latter makes a compelling argument *against* supplying a deterministic search pattern for the initial guess.

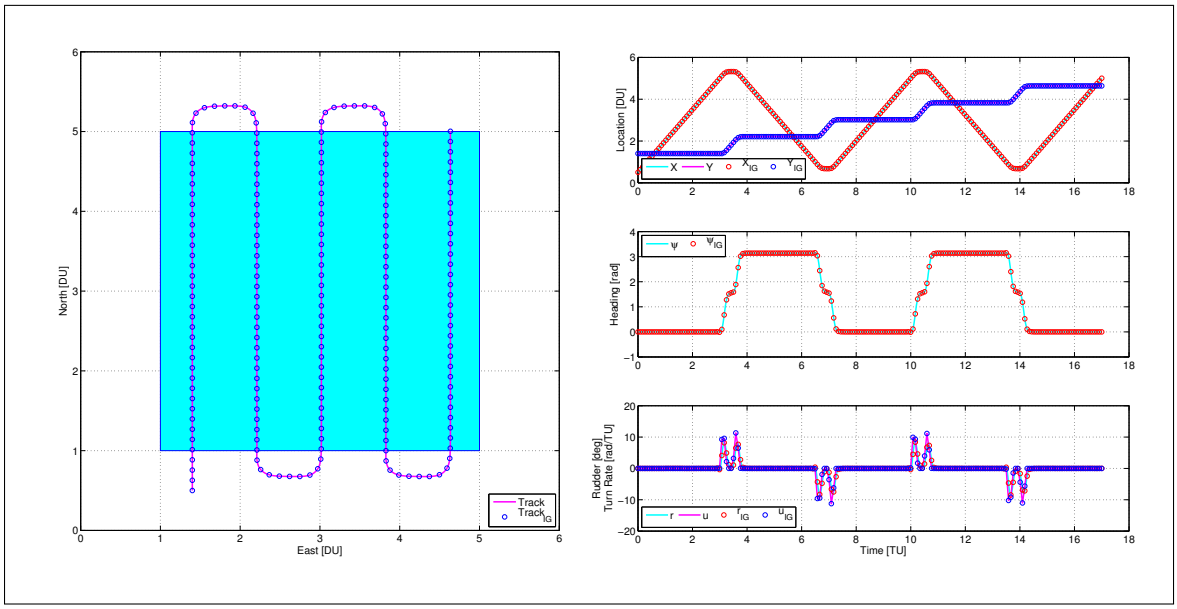

Figure 3.3. Initial guess trajectories for open loop lawnmower pattern.

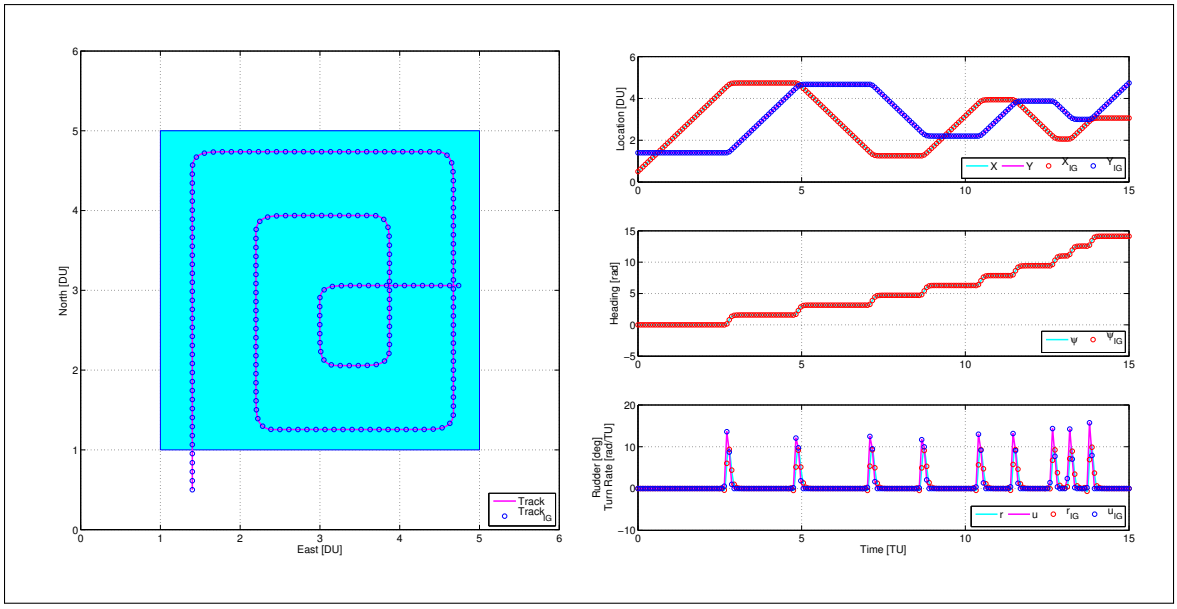

Figure 3.4. Initial guess trajectories for open loop box-spiral pattern.

THIS PAGE INTENTIONALLY LEFT BLANK

CHAPTER 4:
Application: Time-Limited Optimal Search

As we have seen in Chapter 3, computational optimal search can be tailored to model and solve many different MCM problems of interest. Optimal solutions, obtained through simulation, provide performance benchmarks that can inform mission planning under real-world resource limitations. These resources include the number and type of autonomous vehicles at the MCM commander's disposal, as well as the sensors these platforms can carry. Typically, however, the most important resource is time. As Washburn notes in [23]:

> The great questions in search all involve time. We ask, "How long will detection take?" or "What is the probability of detection in a fixed time?" Detection is inevitable, given sufficient time. The object of search planning is to speed things up. [23]

Indeed, while a number of planning algorithms have been developed to achieve complete coverage of a search area (see, e.g., [63], [138]), most do not explicitly consider the ramifications of time. Instead, time is a byproduct of the search vehicle's velocity and spatial trajectory. A common metric is the area coverage rate, computed by multiplying a sensor's nominal sweep width by platform velocity. One example described in [139] derives a lower bound for the time required by an aerial vehicle to follow a flight plan that achieves complete sensor coverage. This type of bound can be informative when there is sufficient time to execute a given motion plan, but provides no guidance for adjusting the plan if the bound exceeds the allowable mission duration.

When time is limited and complete coverage is impossible, deterministic search patterns (e.g., lawnmower or box-spiral trajectories) are faced with two choices: 1) execute the original motion plan as long as possible to achieve 100% sensor coverage in a subset of the entire search area; or 2) adjust the track spacing to survey the entire search area, but with incomplete coverage. For a perfect "cookie cutter" sensor and uniform target PDF, both choices are equivalent and the probability of non-detection equals the fraction of unsearched area. Time-limited MCM operations can only reduce this risk by leveraging prior

information about the target distribution. If it is known, for example, that mines have been deployed in an "evenly-spaced mine line," [140] proposes a track-spacing method that yields a probability of missed mines below the un-searched area ratio.

Mission time is a hard constraint in most MCM operations, motivating the fixed-time problem formulation described in Chapter 3. We seek time-limited optimal search trajectories that minimize MCM risk for a given vehicle, sensor, and mission duration—whether or not prior information is available. In this chapter, we demonstrate the flexibility of the GenOC framework by solving MCM search problems for both cases. First, we implement an RID mission in which a vehicle with high-resolution sonar must revisit a previously detected mine target whose location is given by a joint, normalized, beta distribution. Next, we implement a wide area survey to detect and localize MLOs, using the conservative assumption of a uniform target PDF to represent no prior information. Such missions are typically conducted during the initial phase of an MCM operation. For this mission, we compare time-limited search performance, i.e., the MCM risk vs. allotted mission time, for optimal trajectories and well-known deterministic search patterns. Finally, we discuss the impact of time discretization on numerical solutions.

4.1 Search with Prior Information—Mine Reacquisition

During the initial phase of an MCM operation, wide area surveys are conducted to detect mine-like objects (MLOs) in the environment that pose a threat to naval forces. These surveys can produce datasets with dozens of potential target locations, so it is critical to distinguish actual mines from harmless clutter before launching time-intensive neutralization missions. Successful target identification requires high-resolution sensors not typically carried on the initial survey vehicles, and these sensors are more effective at close range. As a result, follow-on missions are conducted to revisit the MLOs with AUVs carrying imaging sonars or video cameras. This type of reacquire-identify (RID) mission incorporates prior information about MLO locations provided by the survey, but this data is uncertain; its accuracy depends upon the sensing and navigational performance of the survey vehicle itself. The searcher should expect to search for the target once it arrives in the vicinity of the surveyed location. We therefore cast the motion planning problem for an RID mission as an optimal search for a target whose probability density is more informative than the uniform density assumed for the initial MCM search.

In this section, we apply the GenOC framework to solve problems of this type. We assume that a prior survey has detected and localized a MLO with probability density described by a joint normalized beta distribution in two dimensions (see Section 3.3). For a search area of 20 DU $\times$ 20 DU in size, we select (α, β) parameter values of [8 DU, 16 DU] in the north direction and [16 DU, 8 DU] in the east direction. Substituting these values into Equation (3.6) produces the two dimensional PDF shown in Figure 4.1, pictured prior to commencement of the RID mission. Our objective value, the residual risk of non detection, is plotted on a color scale in which high probabilities are shown in dark red, and low probabilities are shown in blue. This β distribution corresponds to a previously-detected target located at $[\omega_x, \omega_y]$ = [12 DU, 19 DU].

We wish to compute the time-limited optimal trajectory for a 40-minute RID mission by a REMUS 100 AUV equipped with high-resolution imaging sonar. For this problem, we assume that the search area shown in Figure 4.1 has a flat bottom and the AUV operates with constant velocity $V = 1.5$ m/s at altitude $h = 3$ meters above the sea floor. The AUV is programmed to launch from a start location at $[x, y]$ = [1 DU, 7 DU] on an initial heading of 45 degrees, utilizing prior information about the expected target location [12 DU, 19 DU]. The search vehicle's initial state vector is therefore given by $\vec{x}(0)$ = [1 DU, 7 DU, $\pi/4$ rad, 0 rad/TU]^T. A naive, yet feasible initial guess trajectory is provided to the solver using an open loop rudder step function to generate a wide right turn.

The search performance of the 450 kHz and 900 kHz blazed array FLS models from Table 2.1 are compared in Figure 4.2 and Figure 4.3, respectively, for different numbers of discrete time nodes. To compare optimal trajectories generated with different discretization grids (in the time and/or spatial domains), we re-compute objective values using a common baseline of 500 time nodes and 25×25 grid of spatial nodes.

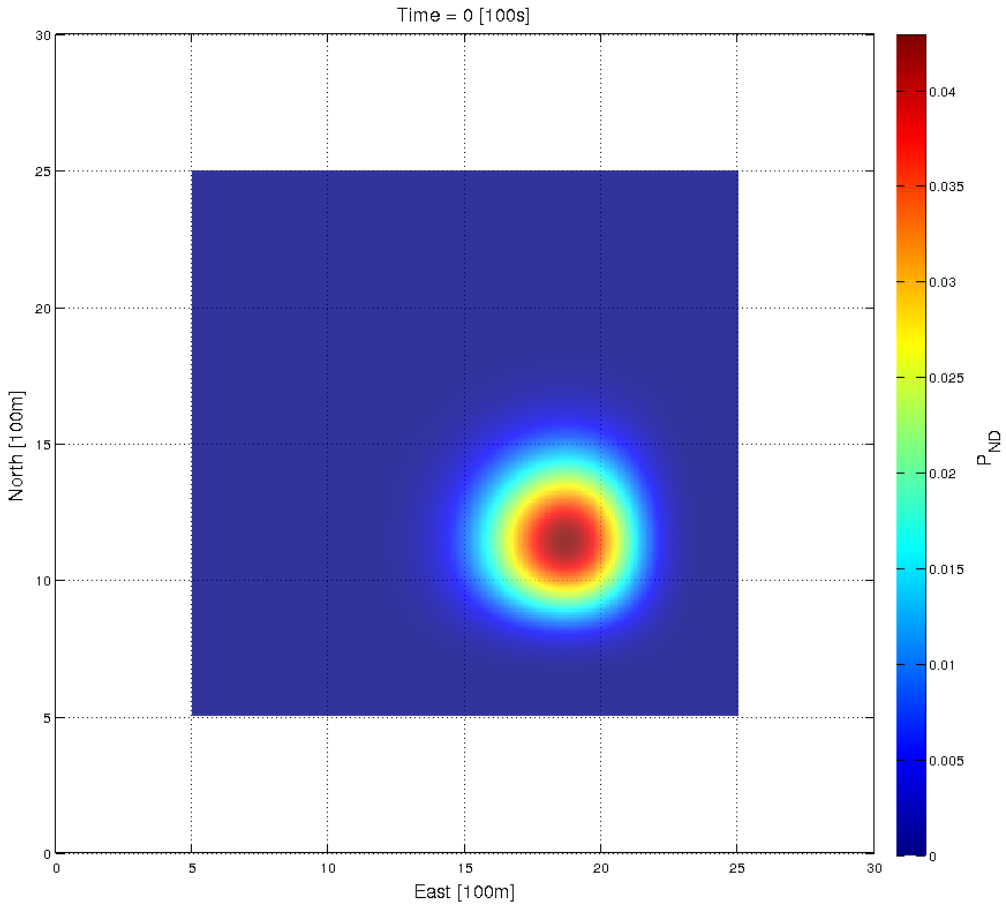

Figure 4.1. Normalized beta distribution for a previously detected target located at [12 DU, 19 DU].

We accomplish this by:

1. Interpolating the solver's control input trajectory onto a fine grid of 500 time nodes.
2. Propagating this finely-gridded control input through the vehicle's EOM, using MATLAB's ode45 solver to generate finely gridded state trajectories.
3. Re-calculating the objective function for the resulting 500-node, dynamically feasible state trajectories.

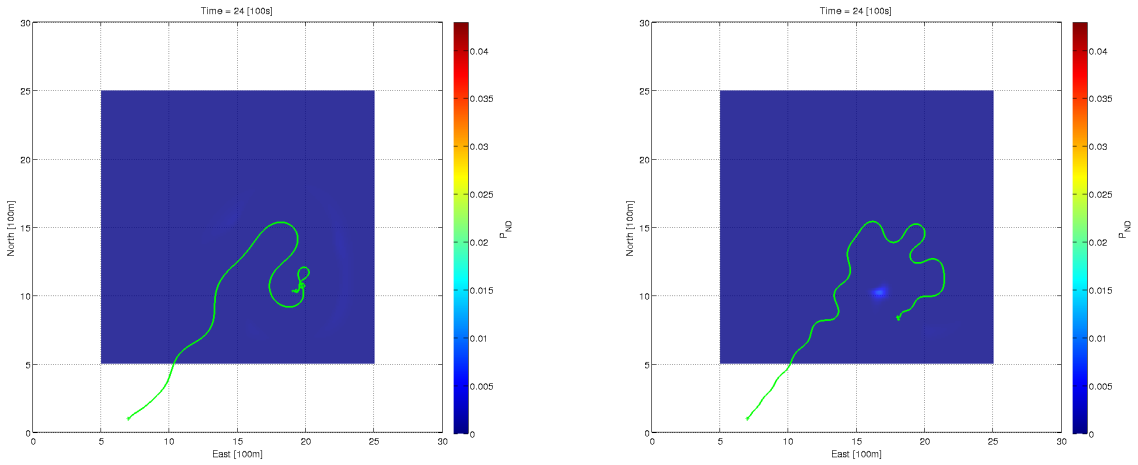

Figure 4.2. Optimal RID trajectories for a REMUS AUV with P450 FLS. Left: $P_{ND} = 0.012$ (20 time nodes). Right: $P_{ND} = 0.001$ (35 time nodes).

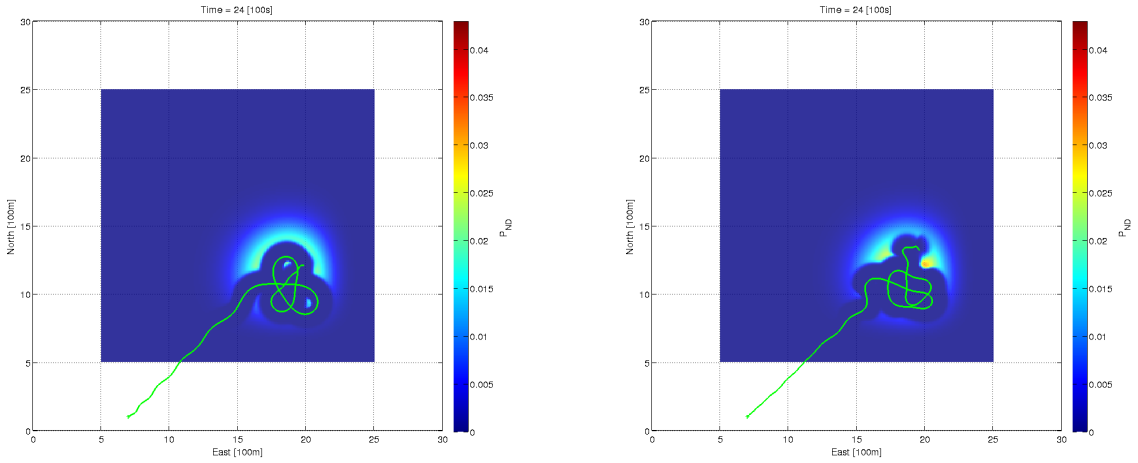

Figure 4.3. Optimal RID trajectories for a REMUS AUV with P900 FLS. Left: $P_{ND} = 0.333$ (30 time nodes). Right: $P_{ND} = 0.305$ (40 time nodes).

The 20-node trajectory in Figure 4.2 (at left) makes two parallel passes over the search area and then loiters over the expected target location for the remainder of the mission. The 35-node trajectory shown at right is more dynamic, approaching the search area from several different headings and almost encircling the expected target location. The 450 kHz blazed

array FLS has a nominal operating range of 200 meters, and an AUV using this sensor for RID missions can reduce the residual risk of non-detection to roughly 1% or less.

If a given mission requires a higher-resolution sonar to achieve positive target identification, the same AUV can deploy a 900 kHz blazed array FLS instead. Example trajectories are provided in Figure 4.3. The 30-node trajectory shown at left executes three symmetric loops over the expected target location, while the 40-node trajectory shown at right sweeps the target area with parallel tracks oriented on two distinct headings. Both solutions achieve a probability of non-detection around 30%, indicating that the 900 kHz sonar is hampered (in coverage) by its 100-meter nominal range. Nevertheless, the GenOC framework produces trajectories that revisit the target area repeatedly until the mission time expires. These solutions have similarities with traditional RID search patterns, which implement partial lawnmower swaths, aligned on different headings, to cover a target from multiple aspect angles for improved classification performance [30]. Results from these simulations are summarized in Table 4.1.

Table 4.1. Optimal time-limited RID trajectories for a REMUS 100 AUV with FLS and $T_f = 2400$ s.

Imaging Sonar	Time Nodes	P_{ND} $500 \times 25 \times 25$	Figure Reference
P450 FLS	20	0.012	Figure 4.2 (left)
	35	0.001	Figure 4.2 (right)
P900 FLS	30	0.333	Figure 4.3 (left)
	40	0.305	Figure 4.3 (right)

4.2 Search with No Prior Information—Mine Survey

In this section, we consider the common MCM problem of planning survey missions to detect MLOs in the absence of prior information about the target distribution. Typically, this involves a labor-intensive process to divide the search area into separate homogeneous regions, and tasking individual MCM assets to cover each region with a deterministic search pattern based on nominal area coverage rates. Various TDAs have been developed to automate aspects of this process, and these information products can be "used by the force

commanders to optimize the employment of naval assets in any particular tactical environment at sea" [56].

Many planning tools, e.g., PATHA, can incorporate sonar performance models and time-based constraints to help mission planners determine the number of assets needed for a given mission [59]. However, these systems do not explicitly consider search vehicle dynamics and their attendant impact on detection performance. The GenOC framework takes this into account, providing a unique capability for planning MCM survey operations. It not only produces time-limited optimal search trajectories that minimize risk for a given vehicle and sensor configuration, but it can also serve as a pre-mission analysis tool to compare the expected performance of different sonar designs or autonomous vehicle teams. The latter refers to the solution of so-called "inverse problems," which is discussed in Chapter 5. The rest of this chapter is focused on the former, and applies the GenOC framework to plan a time-limited MCM survey for the following benchmark problem.

We wish to plan 30-minute MCM survey that achieves 90% probability of detecting a bottom mine hidden anywhere in the 20 DU $\times$ 20 DU search area shown in Figure 4.4, with uniform probability distribution. This corresponds to a risk threshold $P_{ND} \leq 10\%$. For this problem, we assume that the search area has a flat bottom, water depth is 20 meters (e.g., 0.2 DU), and two SeaFox USVs equipped with 200 kHz FLS are available for this operation. We first consider whether a single vehicle can meet the desired risk threshold, and solve an optimal search problem for a SeaFox USV launched from the initial state vector $\vec{x}(0)$ = [1 DU, 7 DU, 0 rad, 0 rad/TU]^T and programmed to operate at constant velocity V = 2.5 m/s = 2.5 VU. A naive, yet feasible initial guess trajectory is provided to the solver using an open loop rudder step function to generate a right turn in the center of the search area.

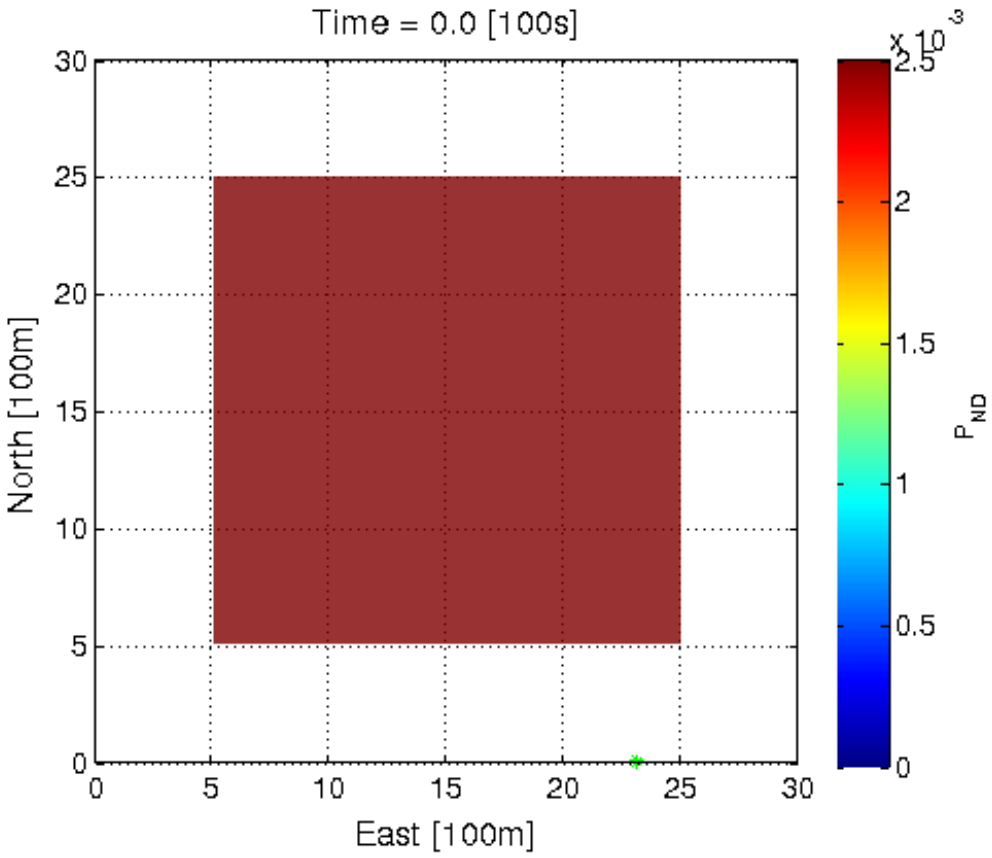

Figure 4.4. Search area with uniform probability distribution, representing no prior target location data.

The optimal time-limited search trajectory is shown in Figure 4.5, which achieves an objective value of $P_{ND} = 0.362$, computed on our $500 \times 25 \times 25$ discretization baseline. This trajectory resembles a box-spiral search pattern, although the limited mission duration does not permit full coverage. Nevertheless, this trajectory represents the best search performance that can be achieved by a single USV launched from the given initial condition. As such, it represents a local minimum, since different initial conditions may yield lower P_{ND} results. Monte Carlo simulation can be employed to determine the most favorable initial condition(s) for exploring a given search area. Due to the symmetry of this problem, however, such solutions are not unique. An initial condition of $\vec{x}(0) = [23 \text{ DU}, 1 \text{ DU}, \pi/2 \text{ rad}, 0 \text{ rad/TU}]^T$ will yield the same result.

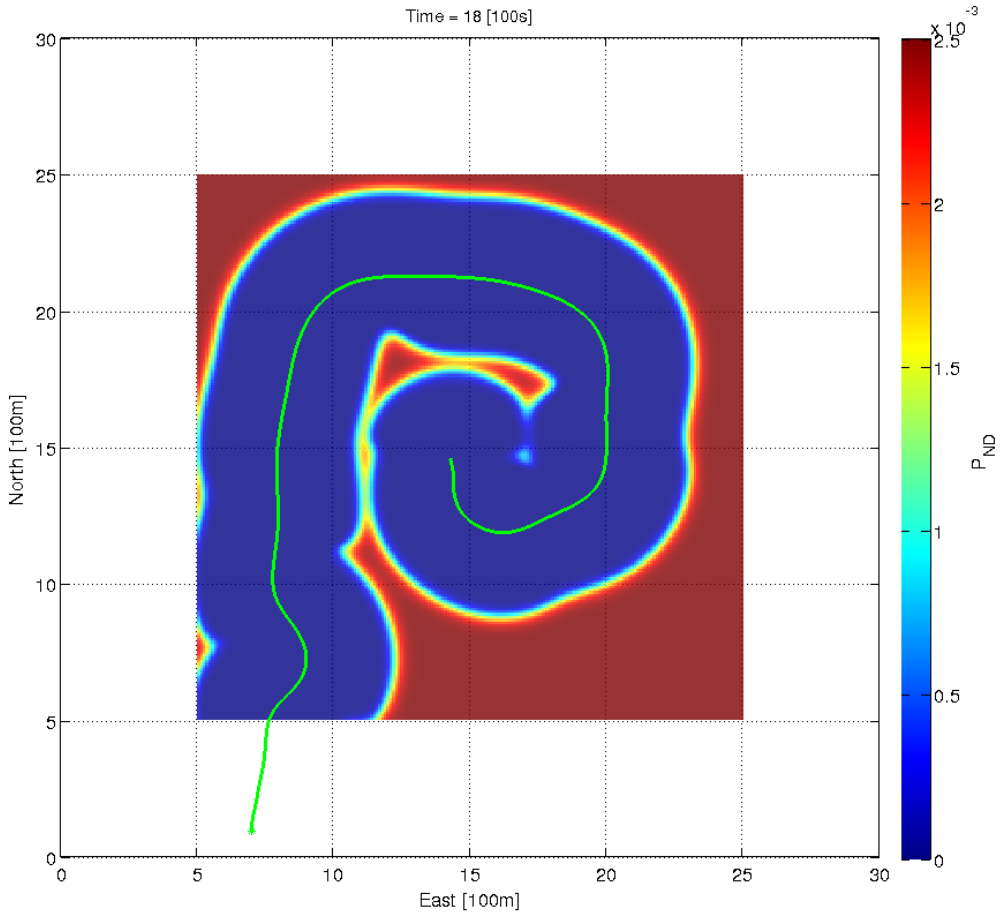

Figure 4.5. Optimal survey trajectory to detect MLOs with a SeaFox USV and 200 kHz FLS in T_f = 30 minutes: $P_{ND} = 0.362$ (30 time nodes).

Since the MCM survey failed to meet the desired risk threshold, the force commander must either increase the mission duration, or deploy additional search assets. Adding a second, identical searcher launched from the initial condition $\vec{x}(0) = [1\text{ DU}, 9\text{ DU}, 0\text{ rad}, 0\text{ rad/TU}]^T$ produces the optimal trajectories shown in Figure 4.6, reducing the risk to $P_{ND} = 0.022$ in the same 30-minute mission. This result suggests that two vehicles can meet the desired risk threshold of $P_{ND} = 0.1$ with a shorter mission duration.

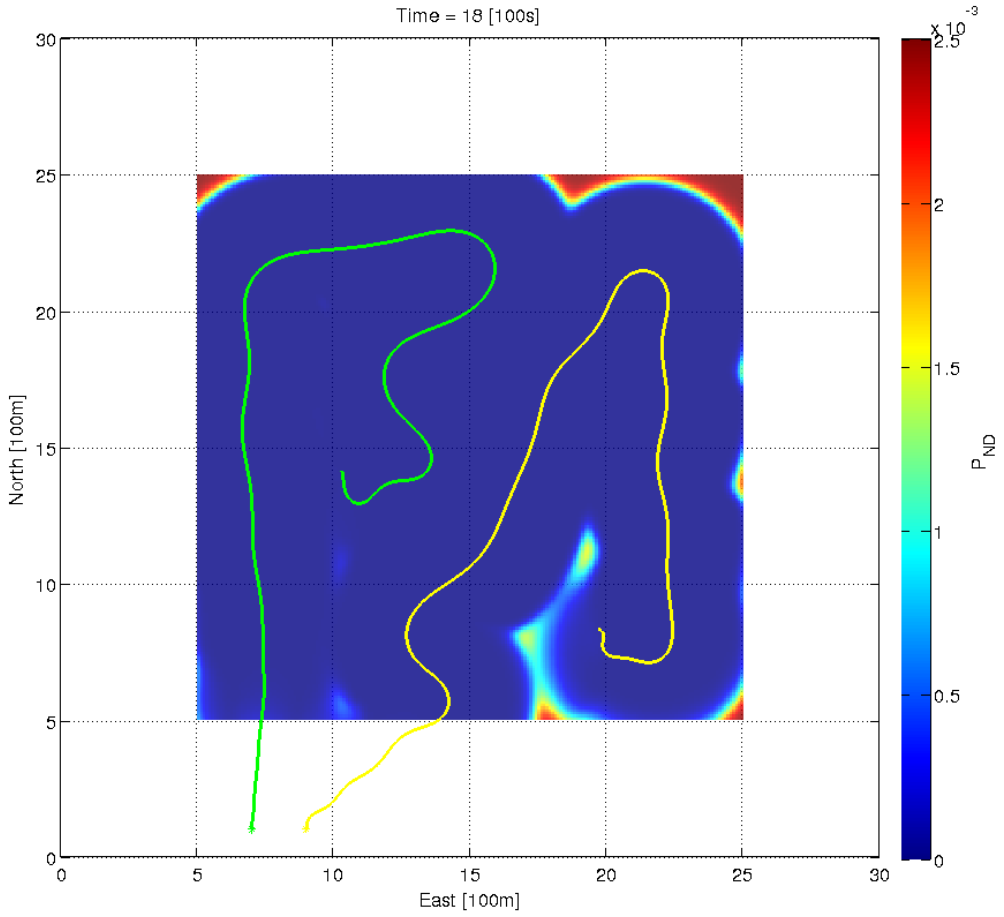

Figure 4.6. Optimal survey trajectories to detect MLOs with two SeaFox USVs and 200 kHz FLS in T_f = 30 minutes: P_{ND} = 0.022 (30 time nodes).

Additional simulations were conducted to determine whether two vehicles could achieve the survey objective in less time. Figure 4.7 shows the optimal trajectories computed for a 20-minute (at left) and 25-minute (at right) mission. The 20-minute mission has time-limited performance $P_{ND} = 0.224$ and fails to meet our objective, while the 25-minute mission achieves $P_{ND} = 0.087$, equivalent to a detection probability $P_D > 91\%$. Results from these simulations are summarized in Table 4.2.

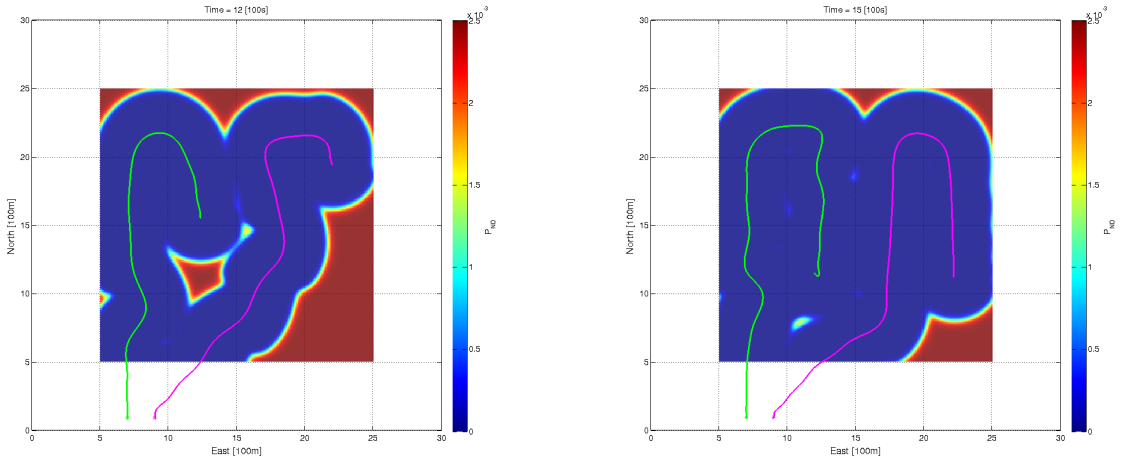

Figure 4.7. Optimal mine detection survey trajectories for two SeaFox USVs with 200 kHz FLS. Left: $P_{ND} = 0.224$ (20 time nodes) in 20 minutes. Right: $P_{ND} = 0.087$ (30 time nodes) in 25 minutes.

Table 4.2. Optimal time-limited trajectories for mine detection using SeaFox USVs and 200 kHz FLS.

Number of USVs	Mission Duration	Time Nodes	P_{ND} $500 \times 25 \times 25$	Figure Reference
1	1800 s	30	0.362	Figure 4.5
2	1200 s	20	0.224	Figure 4.7 (left)
	1500 s	30	0.087	Figure 4.7 (right)
	1800 s	30	0.022	Figure 4.6

4.3 Search Performance vs. Mission Duration

There is an inherent time-dependency of the exponential detection model incorporated into the objective function of Equation (3.11). This model produces diminishing returns on search effort applied to previously visited regions of the operating area. Optimal search can leverage this property to produce motion plans which accomplish both *exploration*, when we wish to acquire information about the environment (Section 4.2); and *exploitation* of all relevant prior information (Section 4.1). We have already seen how mission duration impacts the optimal vehicle trajectories and achievable search performance for a given

mission. While it is intuitively obvious that searching for longer periods of time can lower MCM risk, the ability to rapidly solve *optimal* search problems allows MCM commanders to quantitatively address questions such as:

- What is the residual risk after searching for a fixed duration with a given vehicle and sensor combination?
- How long will it take a search vehicle to reach a desired risk threshold with a given sensor payload?
- How much time savings can be achieved by employing multiple search assets?

Using the GenOC framework, we can conduct several simulated experiments to solve a given optimal search problem for different values of our fixed mission duration. Subsequent Monte Carlo analysis can identify trends in the solution results to help characterize the optimal performance of a given system configuration as a function of time. Note that our current computational framework was written to solve GenOC problems with fixed final time; at present, we rely on Monte Carlo simulations to answer questions regarding the minimum time to reach a given risk threshold, for example. Future work will investigate the use of optimal control software packages like DIDO [141], which can address minimum-time problems directly, for solving this class of GenOC problems.

Meanwhile, we must address two minor complications arising from this approach. First, the numeric solution to a given optimal control problem is repeatable over multiple runs; we must therefore inject random variation into our simulations before we can conduct a meaningful statistical analysis. This is achieved by varying the initial condition; the position and heading angle of each search vehicle at $t = 0$ is randomized prior to each simulation, influencing the initial guess trajectories as well. Second, we must impose a feasibility check on the solver's output so that infeasible solutions can be excluded from the analysis.

It is instructive to compare the search performance vs. mission duration of our optimal search trajectories against well-known deterministic search patterns. For the single-USV survey mission described in Section 4.2, the following sections describe the feasible lawnmower and box-spiral trajectories which provide benchmarks for comparison.

4.3.1 Manually-Specified Lawnmower Pattern

Computing the shortest path for a lawnmower coverage pattern to completely cover a polygonal area has been found to be NP-hard; as a result, approximate algorithms are proposed to plan efficient lawnmower trajectories in [142]. Additional examples are proposed in [66], which minimizes the number of turns along the path, and [143] which suggests that these patterns are time-optimal for a robotic lawnmower.

We wish to generate a benchmark lawnmower trajectory that completely covers the 20 DU $\times$ 20 DU search area shown in Figure 4.4. We do so in the manner that an MCM operator programs a waypoint-based mission for a given sensor sweep width. The 200 kHz FLS used in our example has a nominal range of 400 meters, so we select waypoints that place north/south-aligned track lines with 400 meters track spacing, offset by 200 meters from the search area's east/west boundaries. Whereas a sidescan sonar survey would perform the necessary U-turns outside the search area, we assume that the FLS does not incur a performance penalty for turning motions (i.e., $F_r = 1$). Therefore, the long track lines are connected by short legs offset 200 meters from the search area's north/south boundaries to avoid wasted effort. This waypoint pattern is denoted by green circles in Figure 4.8.

Similarly, we specify an initial condition of $\vec{x}(0) = [1 \text{ DU}, 7 \text{ DU}, 0 \text{ rad}, 0 \text{ rad/TU}]^T$, so the USV begins its mission pre-aligned with the first track line, thereby minimizing unnecessary path length. Finally, we ensure feasibility of this lawnmower pattern by constructing each 90-degree turn with clothoid curves (see Section 3.7) and propagating a control input through the EOM to produce the magenta state trajectory shown in Figure 4.8. This trajectory was used to recalculate P_{ND} on our $500 \times 25 \times 25$ discretization baseline for different values of T_f. These results are plotted as blue crosses in Figure 4.9, where each data point represents an entire mission that completes as much of the lawnmower pattern as possible in the time allotted.

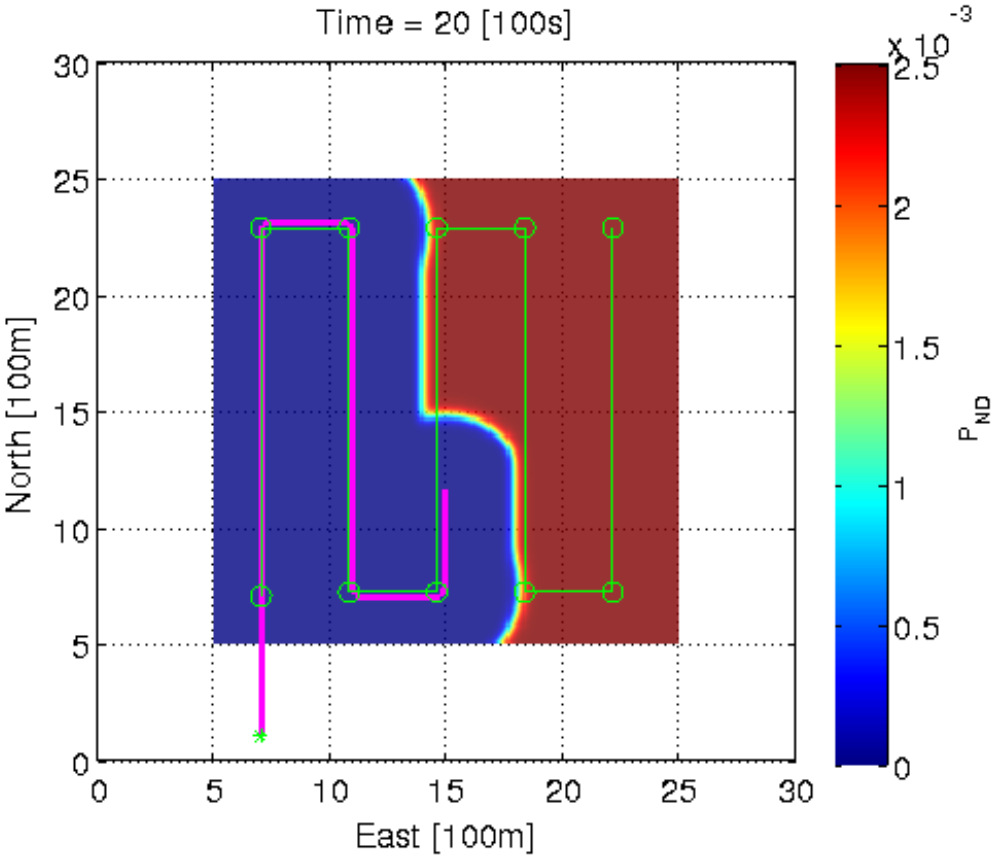

Figure 4.8. Partially completed lawnmower survey for $T_f = 2000$ s.

Figure 4.9 reveals a linear relationship. We note that P_{ND} falls at a constant rate for mission durations up to roughly 3500 seconds, then slows down just before vanishing altogether for missions around 4000 seconds long. The best linear fit to this data is obtained by eliminating data points when $T_f > 3500$ seconds, producing the formula

$$P_{ND} = -0.000253(T_f) + 0.950. \tag{4.1}$$

Equation (4.1) confirms what we would expect: $P_{ND} \approx 1$ for $T_f = 0$ seconds, a trivial mission with no search effort; and $P_{ND} = 0$ for $T_f > 3750$ seconds, which is sufficient time to completely cover the search area.

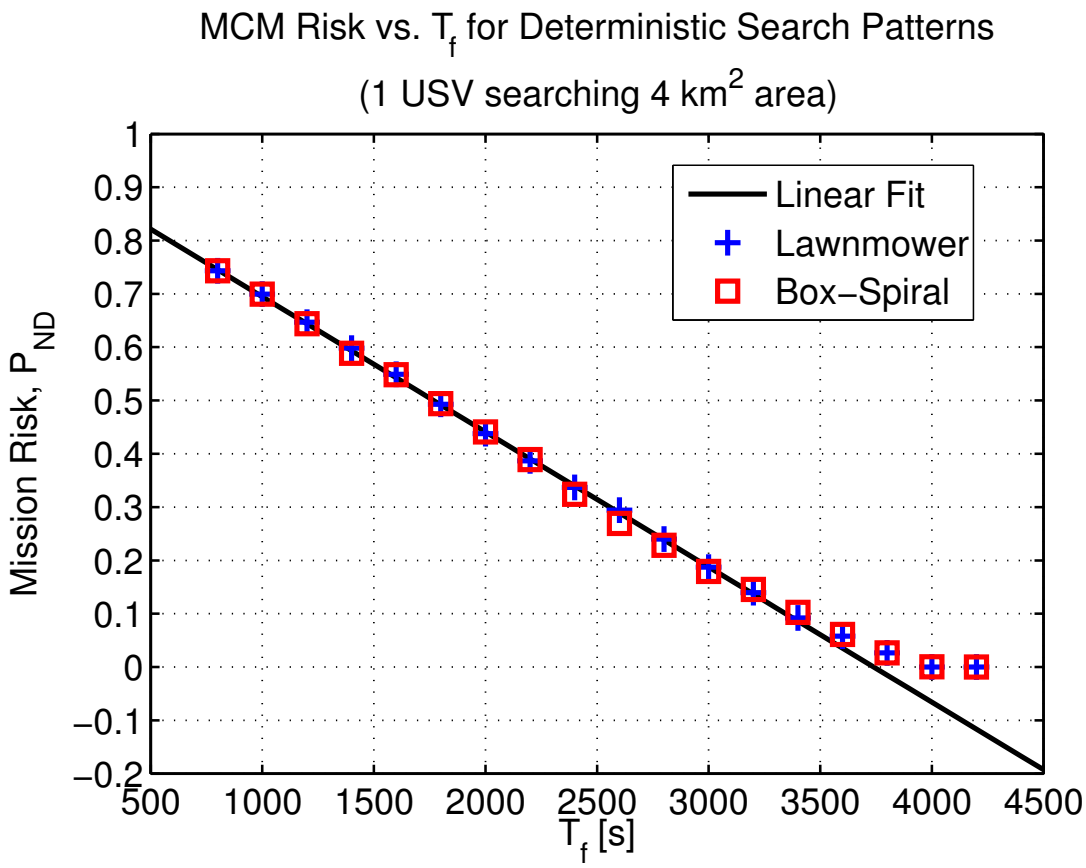

Figure 4.9. Linear fit of lawnmower and box-spiral search performance vs. mission duration.

4.3.2 Manually-Specified Box-Spiral Pattern

Spirals are another popular deterministic search pattern, and box-spirals are very similar to the lawnmower trajectories discussed previously. While both patterns achieve complete coverage, [143] suggests box-spirals as a minimal-energy alternative to time-optimal lawnmower patterns, since box-spirals require less turning effort. Using the same assumptions, waypoint spacing, and initial condition as Section 4.3.1, we generate a benchmark box-spiral trajectory that completely covers the 20 DU $\times$ 20 DU search area of Figure 4.4. The feasible state trajectory for this pattern is the magenta line in Figure 4.10, while the waypoint pattern is denoted by green circles.

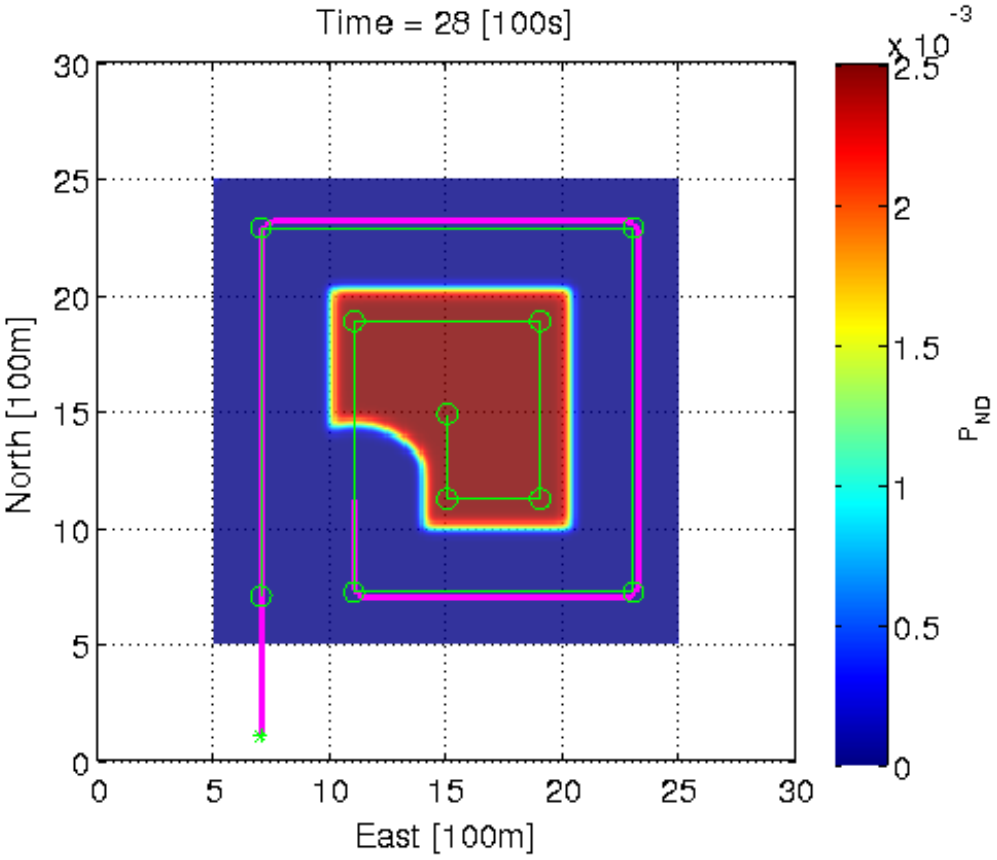

Figure 4.10. Partially completed box-spiral survey pattern for $T_f = 2800$ s.

P_{ND} values, recalculated on our $500 \times 25 \times 25$ discretization baseline, are plotted as red boxes in Figure 4.9 for different values of T_f. As before, each data point represents an entire mission that completes as much of the box-spiral pattern as possible in the time allotted. This data reveals a linear relationship nearly identical to the lawnmower pattern. The best linear fit yields the formula:

$$P_{ND} = -0.000254(T_f) + 0.947. \tag{4.2}$$

The mean of the lawnmower and box-spiral linear fits is depicted by a black line with constant slope in Figure 4.9. A constant slope is expected, since lawnmower and box-spiral trajectories implement "exhaustive search." Recall that exhaustive search with a definite range sensor yields a detection probability P_D equal to the coverage ratio, the fraction of

search area covered by the sensor. Therefore, a "cookie cutter" sensor with sweep width W, mounted on a vehicle moving at constant velocity V, in a search area A, produces a probability of detection $P_D = WVt/A$ that is linear with time [51]. We have simply plotted the complement, $P_{ND} = 1 - P_D$, in Figure 4.9.

4.3.3 Optimal Solution from Solver

Monte Carlo simulations were conducted for the mine survey problem of Section 4.2 to analyze the optimal search performance for a range of mission durations between fifteen minutes and one hour, spaced at two-minute intervals. Ten simulations were conducted for each value of T_f, with initial states drawn from a uniform $\mathcal{U}$(lower, upper) or normal $\mathcal{N}$(mean, std. dev.) probability distribution as follows:

$$\begin{aligned} x(0) &\sim \mathcal{U}(0,10)/DU, \\ y(0) &\sim \mathcal{U}(500,2500)/DU, \text{ and} \\ \psi(0) &\sim \mathcal{N}(0,\pi/12). \end{aligned} \tag{4.3}$$

Initial turn rate $r(0) = 0$. The initial guess is computed from an open loop rudder step input that commands a right turn when $y(0)$ is in the western half of the search area, and commands a left turn when $y(0)$ is in the eastern half of the search area.

The mean objective values of P_{ND} from the ten simulations conducted for each value of T_f are plotted as the blue line in Figure 4.11, while a quadratic curve fit to this data is shown as the dashed magenta line. The mean of the two deterministic search patterns derived previously is shown as a black line for comparison purposes. The plots intersect at roughly $T_f = 3280$ seconds, at an objective value of $P_{ND} = 10\%$. This plot clearly indicates that an optimal search strategy outperforms deterministic, exhaustive search patterns for time-limited missions less than about 55 minutes in duration. However, it also suggests that operators would be better off selecting a deterministic search pattern if there is sufficient time to execute it to completion.

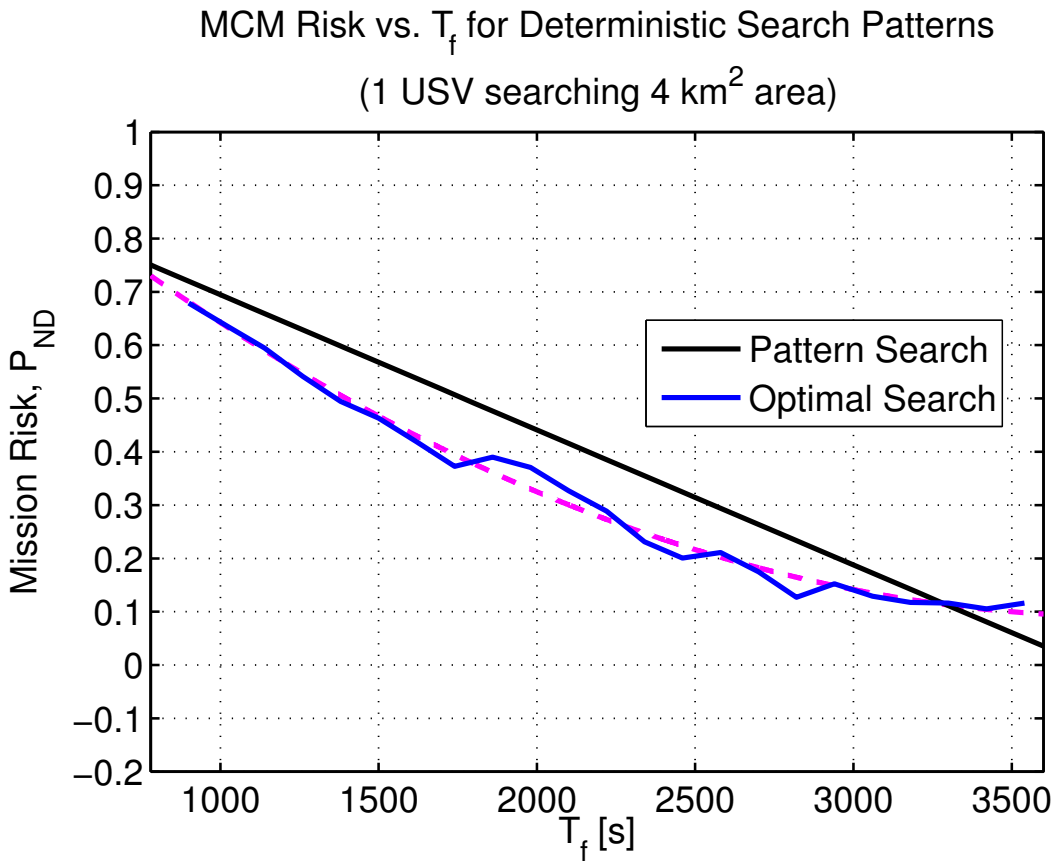

Figure 4.11. Search performance comparison between optimal trajectories and exhaustive search patterns.

The cross-over point may indicate a local minimum that is difficult to overcome with trajectories based on a low number of discrete time nodes. Simulations with excess mission duration are capable of bringing P_{ND} to zero (see RID trajectories in Figure 4.2), albeit with some wasted search effort. In addition, previous simulations conducted using an Euler discretization with hundreds or thousands of time nodes have generated trajectories that more closely resemble lawnmower patterns, but this kind of overkill is computationally prohibitive and not useful for optimal trajectory planning. Futher work is required to investigate optimal search performance when mission duration is roughly equivalent to the time required for exhaustive search.

4.4 Search Performance vs. Time Discretization

One of the most important aspects of motion planning in a computational optimal control framework is the choice of discretization scheme, as this directly impacts accuracy and computational run time. In general, numeric trajectory approximations converge to their continuous counterparts as the number of computational nodes increase [144], [145]. While increasing the number of nodes can improve solution accuracy, designers must balance this accuracy against the computational demands required by high-node discretizations. Moreover, higher-node control trajectory solutions may be infeasible for implementation on an actual vehicle system. A detailed theoretical discussion on this topic is beyond the scope of this dissertation, but an excellent overview on pseudospectral optimal control theory is provided in [4], with convergence and consistency proofs given in [77].

Hurni recommends using "the lowest possible number of nodes for feasible and safe trajectories," and proposes a novel criteria for selecting the number of nodes based on the distance a ground vehicle must travel, and the size of the obstacles it must avoid along the way [74]. We have assumed an obstacle-free environment for MCM search planning. Moreover, we do not require real-time algorithms for dynamic re-planning. Instead, we generate an optimal search strategy for the entire MCM mission, subject to any prior information we possess. The lack of a real-time constraint grants us the luxury of computing multiple solutions with increasingly fine discretization schemes in our search for an optimal, *feasible* search trajectory. Solutions whose feasibility cannot be verified by control trajectory propagation are rejected.

We will demonstrate this concept using the time-limited survey mission described in Section 4.2. Figure 4.12 plots the objective values for ten different optimal solutions, each computed using a different time discretization with N_t time nodes. We observe that as the number of time nodes increase, the numeric solution's objective value converges to $P_{ND} \approx 0.320$. Note, however, that the objective values plotted in Figure 4.12 are the raw solver outputs, calculated directly from the N_t solution trajectory nodes. We denote such objective values by J_{out}.

To support performance comparisons between different numeric solutions, the solution trajectories must first be transferred onto a common discretization scheme. This is achieved by interpolating control trajectories, propagating state variables through the system's ODEs,

and recalculating objective values on our $500 \times 25 \times 25$ discretization baseline. Objective values corresponding to these ODE-propagated state trajectories are designated by J_{ode}. Finally, the propagated trajectories are compared against the solution nodes to assess each solution's feasibility. In this example, all of the numeric solutions with greater than 50 nodes are deemed infeasible. Feasible search trajectories are illustrated in Figure 4.13.

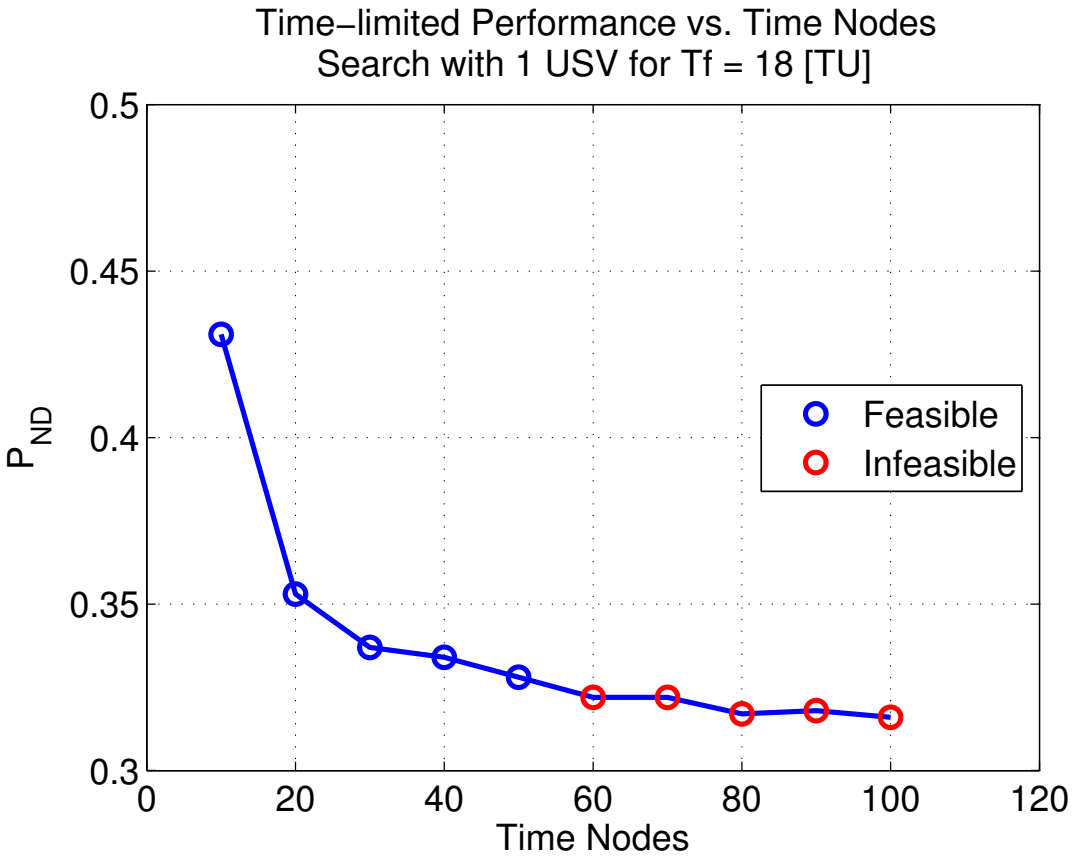

Figure 4.12. Solver-provided objective values vs. the number of discrete time nodes for a single-vehicle, 30-minute survey mission.

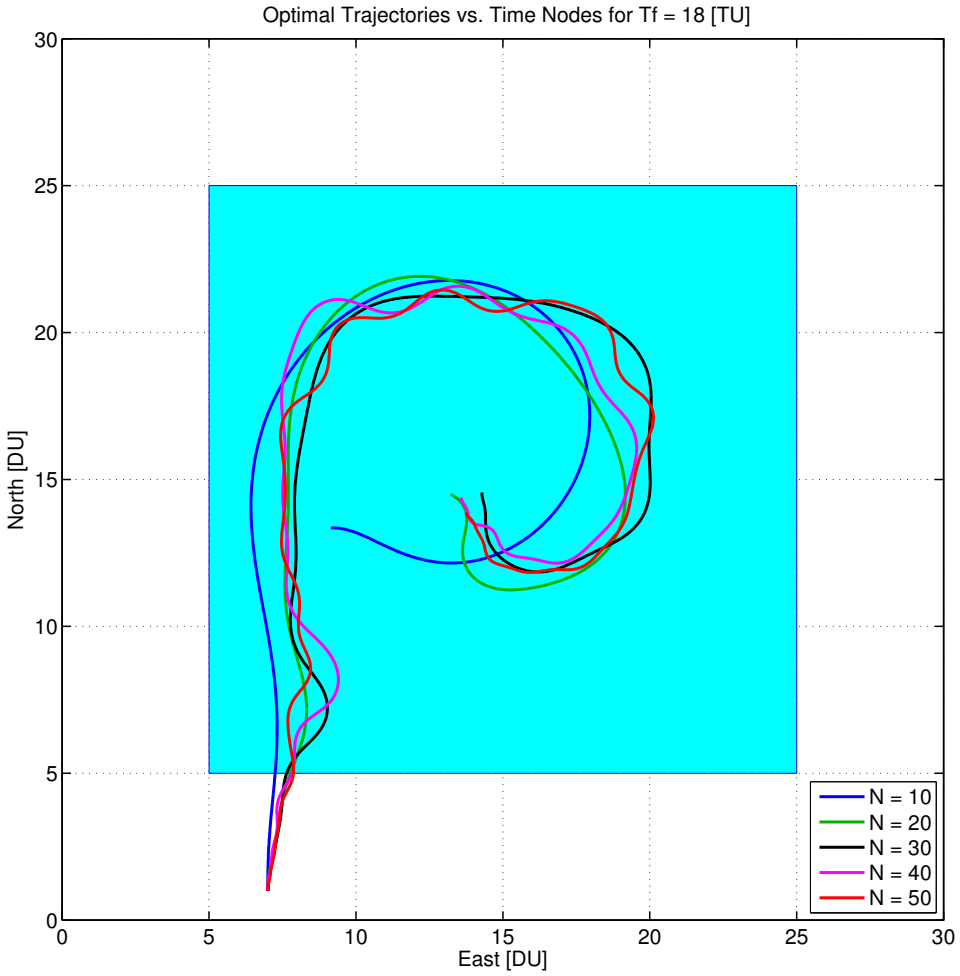

Figure 4.13. Single-vehicle, 30-minute survey trajectories computed for different time discretizations.

Note that higher-node solutions incorporate periodic turning motions in their trajectories. This has the benefit of aiming the vehicle's FLS to cover a larger portion of the search area, reducing the accumulated probability of non-detection. Recall that we have not penalized the detection rate of this FLS for turning motion as we would for a SSS, i.e., the shaping function $F_r(\vec{x}) = 1$ for this problem. This increased complexity yields diminishing returns, however; the optimal trajectories computed using 30 or more time nodes are remarkably

similar, and all of them achieve a P_{ND} within 3% of the 50-node best performer.

Figure 4.14 illustrates the run times required to compute each solution in Figure 4.12 and Figure 4.13 using a 2.30 GHz Xeon CPU (complete processor specifications are listed in [146]). We note that there is a large increase in run time required to compute solutions with more than 40 time nodes, and the 50-node solution takes nearly twice as long as the 30-node solution. Moreover, the 40-node solution takes nearly 5 seconds longer to compute than the 30-node solution, but only decreases P_{ND} by 0.003.

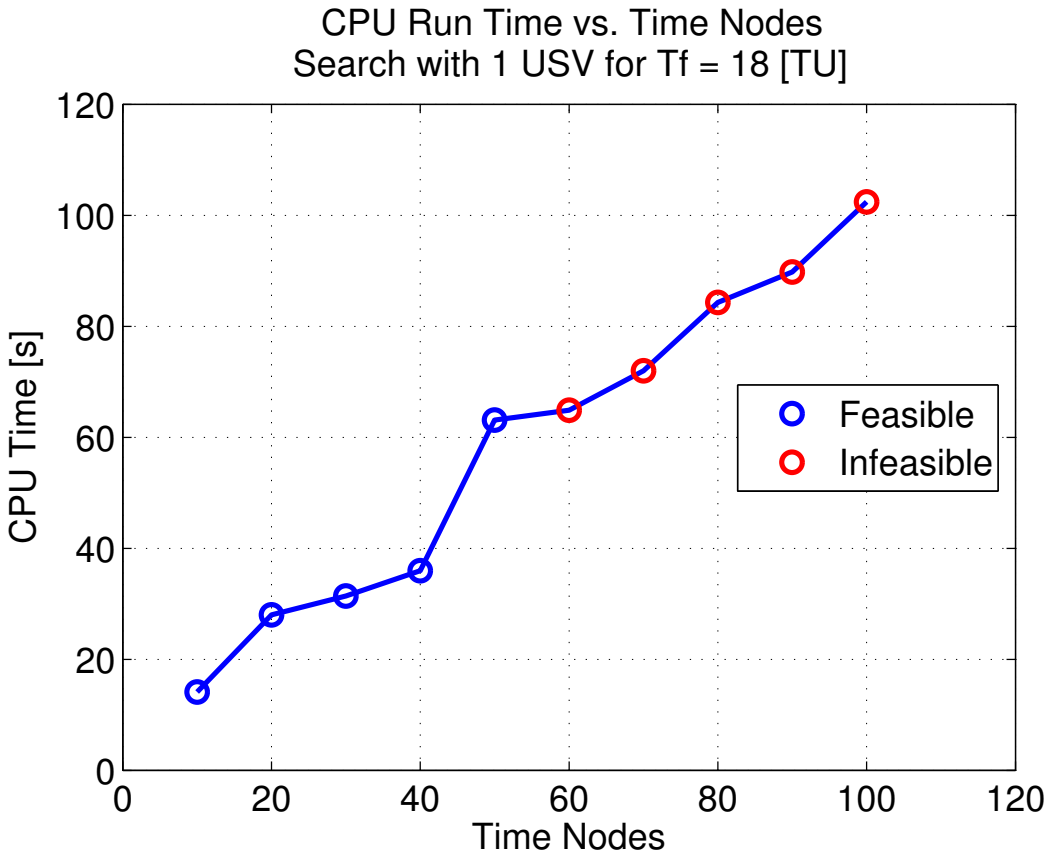

Figure 4.14. Run times vs. the number of discrete time nodes required to compute trajectories for a single-vehicle, 30-minute survey mission.

For this reason, 30-node solutions were selected as an acceptable compromise for the plots presented in Section 4.2. Table 4.3 summarizes the search performance for several one- and two-vehicle mine detection surveys, computed for different mission durations with different

numbers of discrete time nodes. The corresponding two-vehicle trajectories are shown in Figure 4.15 through Figure 4.17.

Table 4.3. Optimal time-limited search performance vs. the number of discrete time nodes for mine detection survey missions.

No. of USVs	Mission Duration	Time Nodes	$J_{out} = P_{ND}$ $N \times 25 \times 25$	$J_{ode} = P_{ND}$ $500 \times 25 \times 25$	CPU Run Time	Figure Reference
1	1800 s	10	0.676	0.431	14.1 s	Figure 4.13
		20	0.443	0.353	28.0 s	
		30	0.358	0.337	31.4 s	
		40	0.342	0.334	36.0 s	
		50	0.328	0.328	63.1 s	
2	1200 s	10	0.453	0.303	47.8 s	Figure 4.15
		20	0.218	0.188	104.7 s	
	1500 s	10	0.428	0.251	47.1 s	Figure 4.16
		20	0.160	0.133	77.5 s	
		30	0.076	0.067	124.5 s	
		40	0.058	0.056	141.5 s	
	1800 s	10	0.459	0.273	46.3 s	Figure 4.17
		20	0.117	0.065	83.7 s	
		30	0.021	0.011	119.5 s	

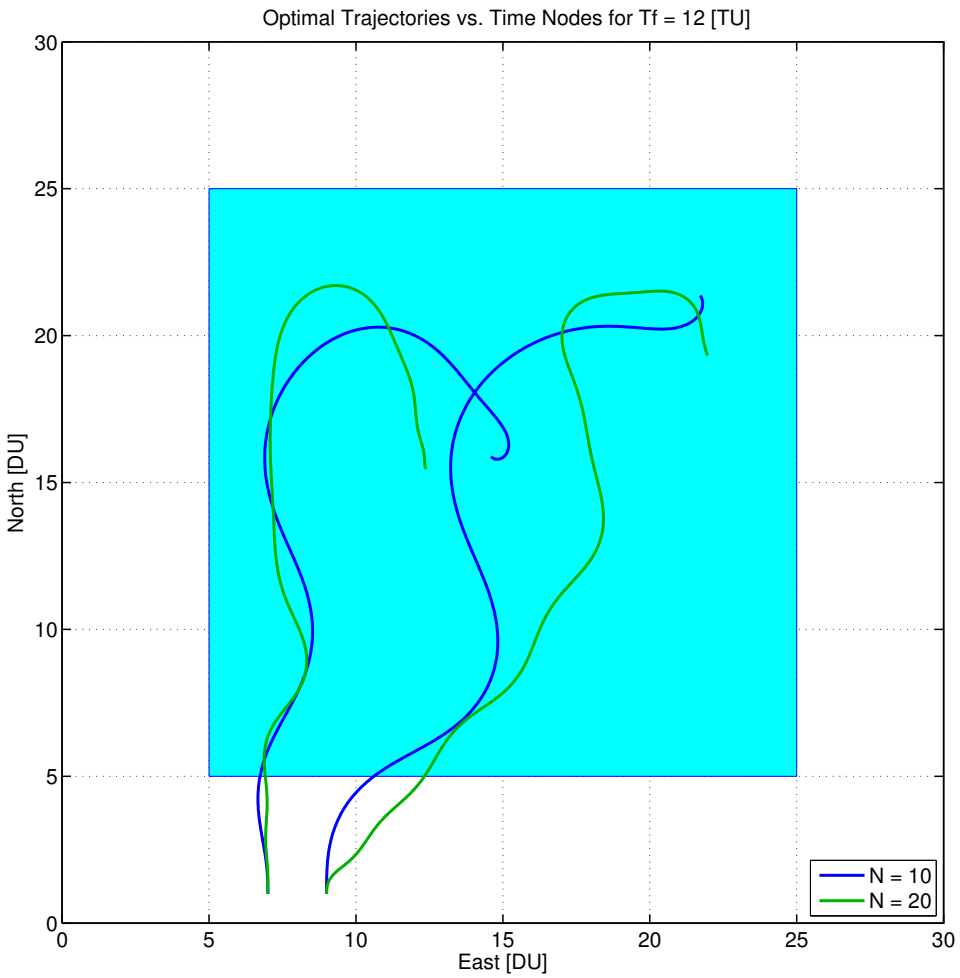

Figure 4.15. Two-vehicle, 20-minute survey trajectories computed for different time discretizations.

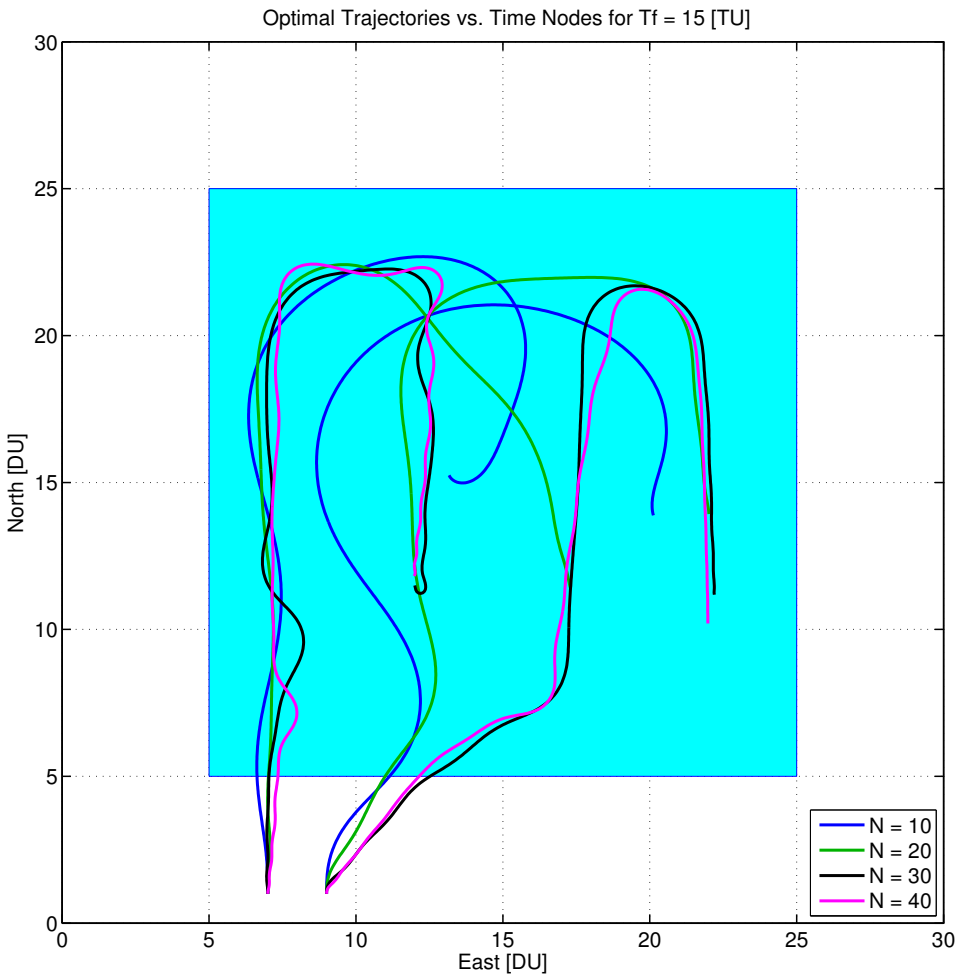

Figure 4.16. Two-vehicle, 25-minute survey trajectories computed for different time discretizations.

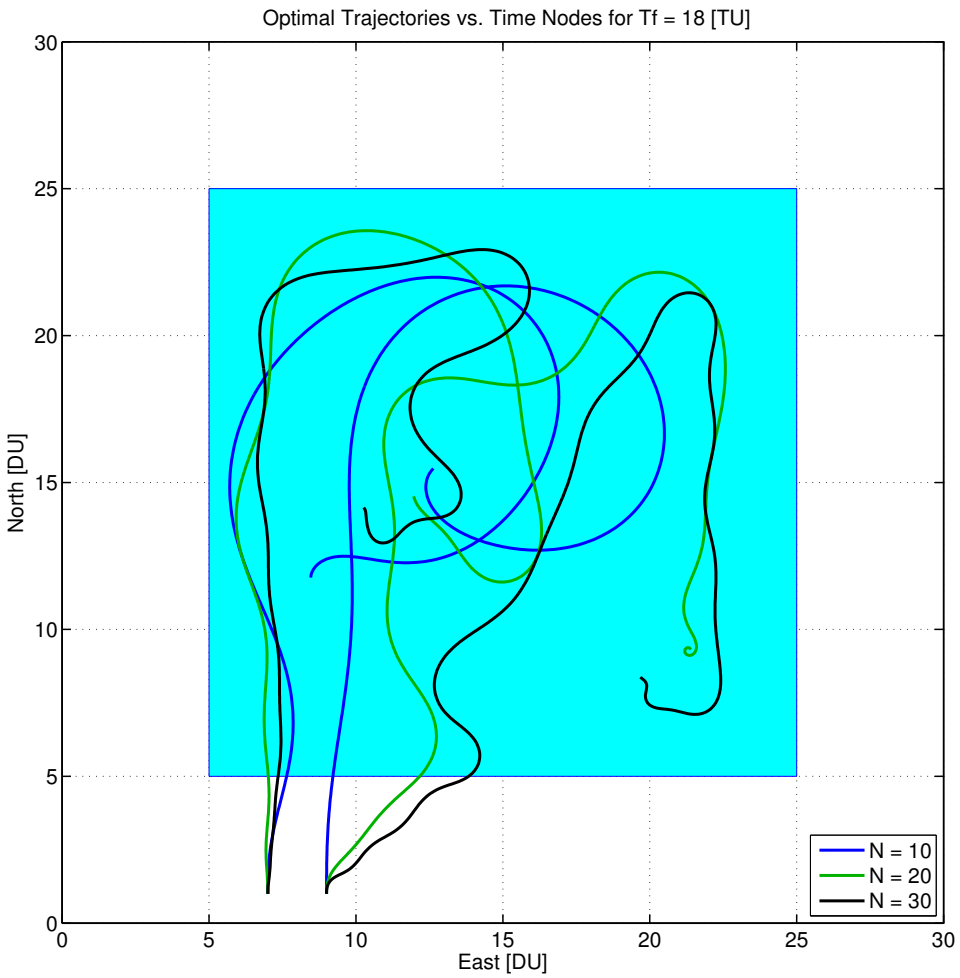

Figure 4.17. Two-vehicle, 30-minute survey trajectories computed for different time discretizations.

CHAPTER 5:
Application: Inverse Problems

The ability to rapidly solve optimal search problems provides a new tool for investigating so-called "inverse" problems related to optimal vehicle and sensor configurations for mine countermeasures (MCM). In Chapter 4, we used the GenOC framework to answer "direct" questions related to sensor-based motion planning for MCM. Typical direct applications involve calculating a feasible trajectory that minimizes the risk of non-detection at the conclusion a wide area survey using a specific sonar; or determining the time required for an autonomous vehicle team to achieve a given performance threshold. Conversely, inverse problems provide engineering insights about the search assets themselves. Such questions include: What is the most effective sonar mounting angle for an optimal search conducted by USVs? Which sonar design parameters have the biggest impact on search performance? How do multiple low-cost systems perform in a given mission, compared against the performance of a single expensive asset?

Over the years, acoustic modeling and simulation have played an increasingly valuable role in the design and evaluation of sonar systems for naval operations. Etter observes:

> Modeling has become the chief mechanism by which researchers and analysts can simulate sonar performance under laboratory conditions. Modeling provides an efficient means to parametrically investigate the performance of hypothetical sonar designs . . . and to estimate the performance of existing sonars in different ocean areas and seasons. [56]

Indeed, the Generic Sonar Model, a predecessor to the USN's current CASS system, was originally "designed to provide sonar system developers with a comprehensive modeling capability for evaluating the performance of sonar systems and . . . permit cost/accuracy trade-offs for specific applications" [147].

This chapter describes a novel approach to solving these kinds of inverse problems, one which recognizes the fact that sonar effectiveness often depends on the vehicles that deploy them. The physics-based sonar models derived in Chapter 2 provide a link between search

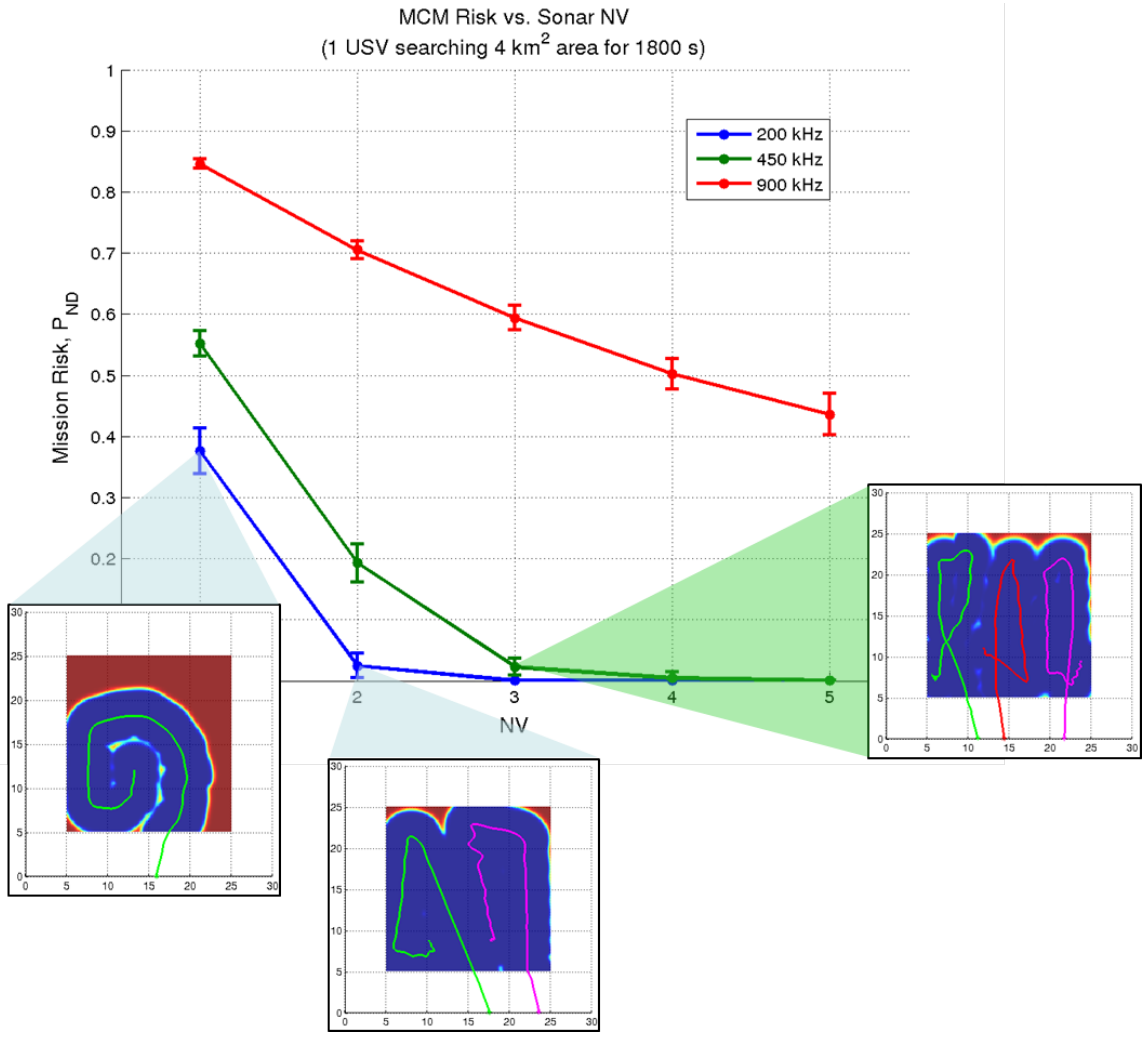

Figure 5.1. Analysis of multi-vehicle search performance with different sonars. Each data point represents several optimal vehicle trajectories.

performance and sonar design parameters, while computational optimal search facilitates the rapid solution of multiple problems required for Monte Carlo analysis. In this way, sonar designers and operational planners can numerically determine the sensitivity of a given optimal search scenario to individual vehicle and/or sonar design parameters. Of course, a beneficial by-product of this analysis is a set of optimal vehicle trajectories linked to a given scenario. This is depicted in Figure 5.1, which emphasizes that each data point in a Monte Carlo analysis is comprised of several optimal trajectories that produced that result.

The Hamming supercomputer, a "hybrid cluster" of computing cores available via the NPS High Performance Computing (HPC) Center [148] was used extensively during the course of this dissertation. Although our computational framework utilizes a sequential optimization algorithm that doesn't lend itself to massive parallelization, several simulations can be launched via the network to run on multiple computing cores simultaneously. This capability was a key enabler for conducting numerous trade studies at once, greatly accelerating the analysis process. Copies of the batch files used to generate the Monte Carlo simulation results for this chapter are provided in Appendix B.

5.1 Sensitivity Analysis

Sensitivity is used to describe the manner in which a desired output variable changes in relation to a change in some other system parameter. Sensitivity analysis provides a measure of robustness in control system design. For our optimal search problem, the desired output is our objective value, the residual MCM risk upon completion of a search operation. To address so-called inverse problems, it is helpful to calculate the sensitivity of MCM risk as a function of sonar/vehicle design parameters or operating characteristics. While our objective function can be expressed analytically, deriving an analytic expression for sensitivity is difficult; it is easier to compute this metric numerically, especially after multiple Monte Carlo simulations have produced ample numerical data to work with. This is the approach taken in this chapter. We note, however, that optimal control offers an elegant method for computing sensitivity via parameter value-function analysis. The Lagrange multiplier for a parameter of interest in an optimal control problem serves as a "sensitivity multiplier." Therefore, it accurately describes the relative impact of this parameter on the objective function [149]. The DIDO software package computes these costates during the solution of an optimal control problem and provides them as outputs, greatly facilitating this type of sensitivity analysis.

5.2 Objective Function Value vs. Time Discretization

As we observed in Section 4.4, the final objective value for optimal solutions computed for an increasing number of time nodes eventually converges, but higher-node solutions are more likely to fail our feasibility criteria. Therefore, it is important to determine the number of time nodes which provides an accurate value for $P_{ND}(T_f)$ yet still produces feasible

trajectories. We accomplish this through a Monte Carlo analysis of several simulations conducted for an array of different time nodes. Once the acceptable number of time nodes has been identified for a given problem, subsequent simulations used to investigate other inverse problems can utilize the same discretization scheme.

The parameter values used for this analysis are listed in Table 5.1, where the bold array notation indicates the range of the independent variable under investigation, i.e., simulations are performed for $N_t = 20, 25, 30, \ldots, 60$. A separate analysis was conducted for each of

Table 5.1. Simulation parameters for N_t analysis (free parameters in bold).

Symbol	Definition	Value
T_f	Mission duration [min]	30
N_{sims}	Number of simulation runs	10
N_v	Number of vehicles	1
N_t	Number of time nodes	**[20:5:60]**
N_ω	Number of parameter nodes	25×25
DU	Canonical distance [m]	100
TU	Canonical time [s]	100
UxV	Vehicle dynamics file	user-selected
FLS	Sonar parameters file	user-selected

the three FLS models derived in Chapter 2. We adopt feasibility criteria similar to the one proposed in [74] to reject infeasible solutions:

$$\mathcal{F} = \sqrt{\sum_{i=1}^{N_t} \left[(x_i - \overline{x}_i)^2 + (y_i - \overline{y}_i)^2 \right]}, \tag{5.1}$$

where $[x_i, y_i]$ is the location of solution node i, and $[\overline{x}_i, \overline{y}_i]$ is the location along the propagated trajectory, interpolated at time t_i. We declare feasibility if $\mathcal{F} < \mathcal{F}_{max}$, where $\mathcal{F}_{max} \in [2, 3]$ provides good rejection criteria for this problem. For each of the N_t values listed in Table 5.1, Figure 5.2 plots the mean and standard deviation (depicted by solid lines and error bars, respectively) for the objective values from ten simulations. Figure 5.3 shows the fraction of these search trajectories which meet our feasibility criteria. Search

performance for the solver output J_{out} and the ODE-propagated solution J_{ode} (recalculated on our $500 \times 25 \times 25$ discretization baseline) are both provided for comparison purposes.

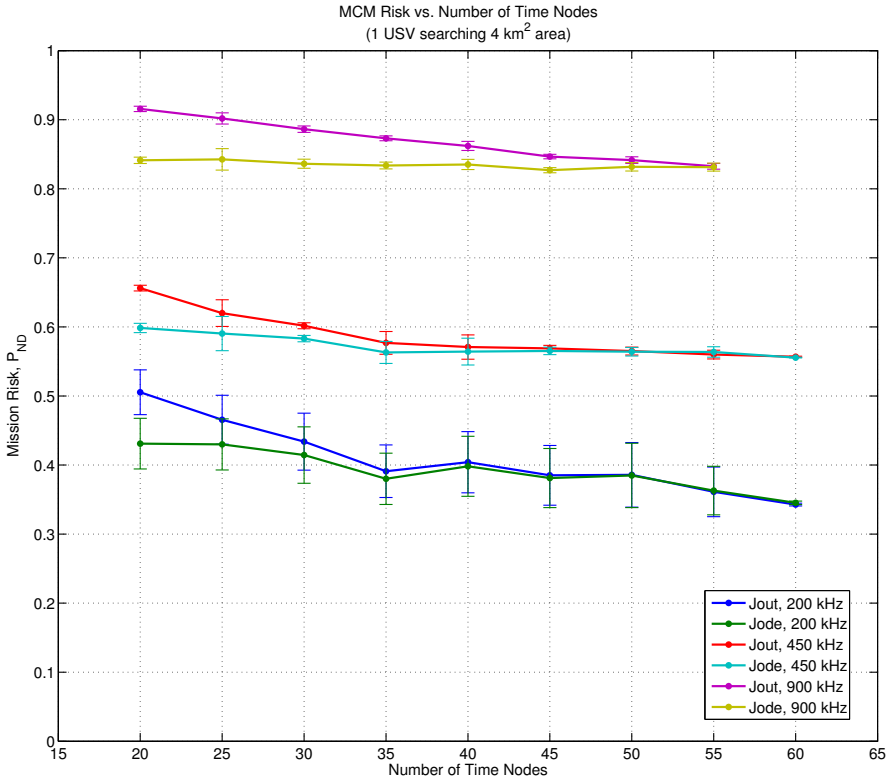

Figure 5.2. Average single-vehicle search performance vs. number of nodes (N_t).

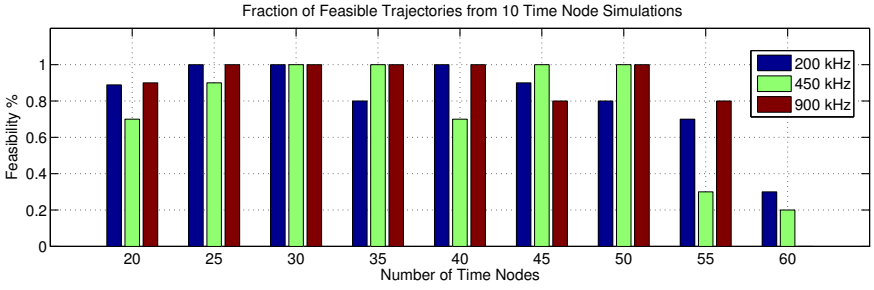

Figure 5.3. Fraction of single-vehicle N_t simulations with feasible trajectories.

These plots illustrate the trade-off between accuracy and feasibility of higher-node solutions. In this problem, all of the 30-node solutions produced feasible search trajectories for all three sonar models, but their objective values have not yet converged to the objective values of their ODE-propagated trajectories. Alternatively, while the 55- and 60-node solutions yield objective values similar to their ODE-propagated trajectories, these higher-node solutions produce fewer *feasible* trajectories. On the basis of these results, therefore, we have elected to use 50 time nodes for the remaining Monte Carlo analyses presented in this chapter.

5.3 Single-Vehicle Search Performance vs. Sonar Design Criteria

We now consider several inverse problems which investigate how individual sonar design parameters influence optimal search performance for a given MCM search asset. This type of analysis can help sonar developers identify promising equipment modifications that could yield large performance benefits. It can also inform system operators about which configurable settings are most effective in a given scenario. Recall from the sonar design discussion in Chapter 2 that several different parameters influence a sonar's detection rate. The operating frequency directly impacts the attenuation coefficient, which determines the propagation losses due to absorption. Frequency also plays a role in computing a sonar array's directivity index and the ambient noise level the sonar must contend with. All of these influences enter the signal excess equations and impact a sonar's instantaneous detection probability. Other parameters, such as the Poisson Scan rate λ contribute directly to the sonar's instantaneous detection rate, the main driver of our objective function. Finally, geometric dependencies based on FOV or sonar mounting angle can make all the difference between an effective search operation, and one in which the residual risk of non detection is too great.

We propose using the GenOC framework to asses the impact of sonar design parameters on search performance. The general approach used for the Monte Carlo analyses in each of the following sections is to hold all parameters constant except the parameter of interest, and conduct multiple optimal search simulations for each set of parameter values. We utilize 50 time nodes for all simulations, based on the analysis in Section 5.2. The proposed approach requires certain choices to be made regarding which values to use for parameters

being held constant in a given simulation. In most cases (e.g., for FOM, Poisson Scan rate λ, and horizontal FOV), we choose the median parameter value from among the three FLS systems. Moreover, we ensure a fair comparison among the different sonar designs by setting the horizontal field of view to 90 degrees for all systems. Lastly, for analyses not directly concerned with a given sonar parameter (e.g., optimal number of search assets), we utilize the actual sonar models listed in Table 2.1.

An exception to this policy is made for the case of a sonar's vertical mounting angle V_{DE}, since initial simulation results that held V_{DE} to a median value for all three sonars unfairly penalized detection performance of the 200 kHz and 900 kHz sonars. In fact, vertical mounting angle V_{DE} plays a critical role in a sonar's effectiveness, particularly when searching for bottom mines with a USV. It is worth identifying other parameters which might be tightly-coupled through either problem geometry or sonar frequency. The FOM, for example, reflects a sonar design's achievable range based on positive signal excess. We expect that this parameter would couple with the sonar's vertical mounting angle, since these two parameters define a trigonometric relationship between the sonar and a bottom target.

Fortunately, we have determined that using the median value of 66 dB for the FOM in certain simulations had only a minor impact on the problem's geometry. Specifically, the noise-limited range for a 200 kHz FLS with nominal FOM = 72 dB decreases by about 81 meters for a FOM of 66 dB. This only changes the optimal V_{DE} from -5.4 to -6.1 degrees, a difference of only -0.7 degrees. Similarly, increasing the nominal FOM for the 900 kHz FLS from 64 dB to 66 dB increases noise-limited detection range by about 5 meters. This changes the optimal V_{DE} for this sensor from -13.1 degrees to -12.4 degrees, a difference of only +0.7 degrees. Therefore, we justify the decision to analyze vertical mounting angle first, and use the optimal V_{DE} values determined from these simulations in all subsequent analyses.

5.3.1 Vertical Mounting Angle

Vertical mounting angle is an important consideration for detecting bottom mines, as this parameter determines the ability of a sonar's beams to cover the sea floor from a vehicle platform's operating altitude. While sophisticated sonar like the ATLAS can electronically steer their beams in the vertical plane, lower-cost systems typically transmit at a fixed

angle. Therefore, these sonars are usually hard-mounted onto a vehicle at a vertical angle that optimizes the sonar imagery collected from the vehicle's customary operating altitude. A custom BlueView P450 FLS system designed for use on the NPS REMUS 100 AUV, for example, was designed with multiple blazed arrays mounted at a permanent tilt angle of $V_{DE} = -10$ degrees (see Figure 5.4).

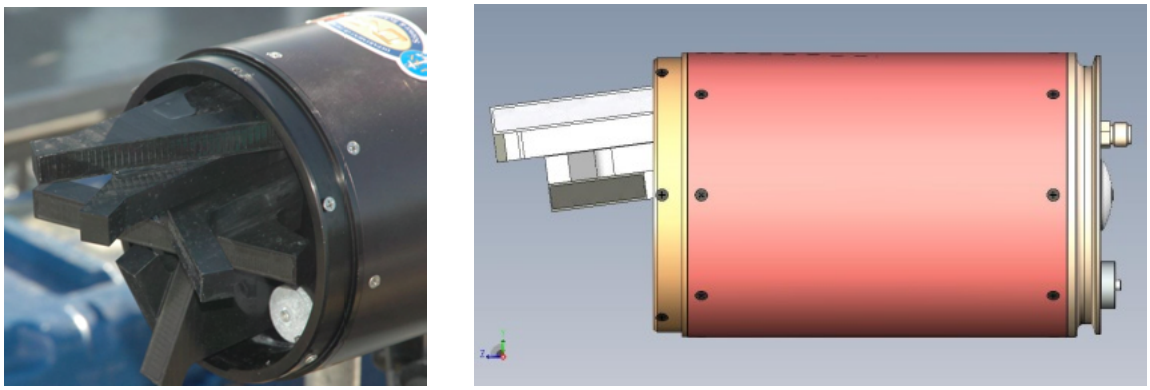

Figure 5.4. Custom BlueView P450 blazed array FLS mounted at -10 degrees.

The parameter values used for this analysis are listed in Table 5.2, where the bold array notation indicates the range of the independent variable under investigation, i.e., simulations are performed for $V_{DE} = -25, -20, -15, \ldots, -5$ degrees. For each of the V_{DE} values listed in Table 5.2, Figure 5.5 plots the mean and standard deviation (depicted by solid lines and error bars, respectively) for the objective values from ten simulations. Figure 5.6 shows the fraction of these search trajectories which meet our feasibility criteria. Search performance for the solver output J_{out} and the ODE-propagated solution J_{ode} (recalculated on our $500 \times 25 \times 25$ discretization baseline) are both provided for comparison purposes.

Not surprisingly, longer-range sonars (i.e., with higher FOM) perform better at small mounting angles, while shorter-range, high-resolution sonars require steeper angles to effectively reach the bottom. From this analysis, we can determine that the optimal mounting angles for detecting bottom mines in 20 meters of water with 200 kHz, 450 kHz, or 900 kHz FLS from on a USV are -6 degrees, -7 degrees, and -11 degrees, respectively. Even so, the 900 kHz FLS is poorly suited for detecting bottom mines from a USV in this benchmark problem's 20-meter water depth.

Table 5.2. Simulation parameters for V_{DE} analysis (free parameters in bold).

Symbol	Definition	Value
T_f	Mission duration [min]	30
N_{sims}	Number of simulation runs	10
N_v	Number of vehicles	1
N_t	Number of time nodes	50
N_ω	Number of parameter nodes	25×25
DU	Canonical distance [m]	100
TU	Canonical time [s]	100
UxV	Vehicle dynamics file	user-selected
f	Sonar operating frequency [kHz]	{200, 450, 900}
FOM	Figure of Merit [dB]	66 (median value)
λ	Poisson Scan rate [scans/s]	0.5 (median value)
σ	Signal excess P_D uncertainty [dB]	9 dB
H_{FOV}	Horizontal field of view [deg]	90 (minimum value)
V_{FOV}	Vertical field of view [deg]	10 (median value)
V_{DE}	Vertical mounting angle [deg]	**[-25:5:-5]**

Additional simulations were conducted to determine the best mounting angles for different FLS deployed from a REMUS 100 AUV operating at 3 meters above the sea floor. An analysis of these results determined that the optimal mounting angles for detecting bottom mines from a survey altitude of 3 meters with the 450 kHz and 900 kHz FLS are -3 degrees and -5 degrees, respectively. The 200 kHz FLS was exempted from this analysis since the REMUS 100 AUV is unable to deploy a sensor of this size. The RID missions presented in Section 4.1 utilized these values for V_{DE}.

Figure 5.6 reveals that simulated survey missions with the 200 kHz FLS at down-tilt angles less than nine degrees produced only a handful of feasible trajectories. Although this may explain the relatively large standard deviation in P_{ND} with these mounting angles (see, e.g., the error bars for $V_{DE} = -6$ and $V_{DE} = -8$), more analysis is needed, perhaps using fewer time nodes, to verify this result. This is especially important since V_{DE} has such a large impact on search performance.

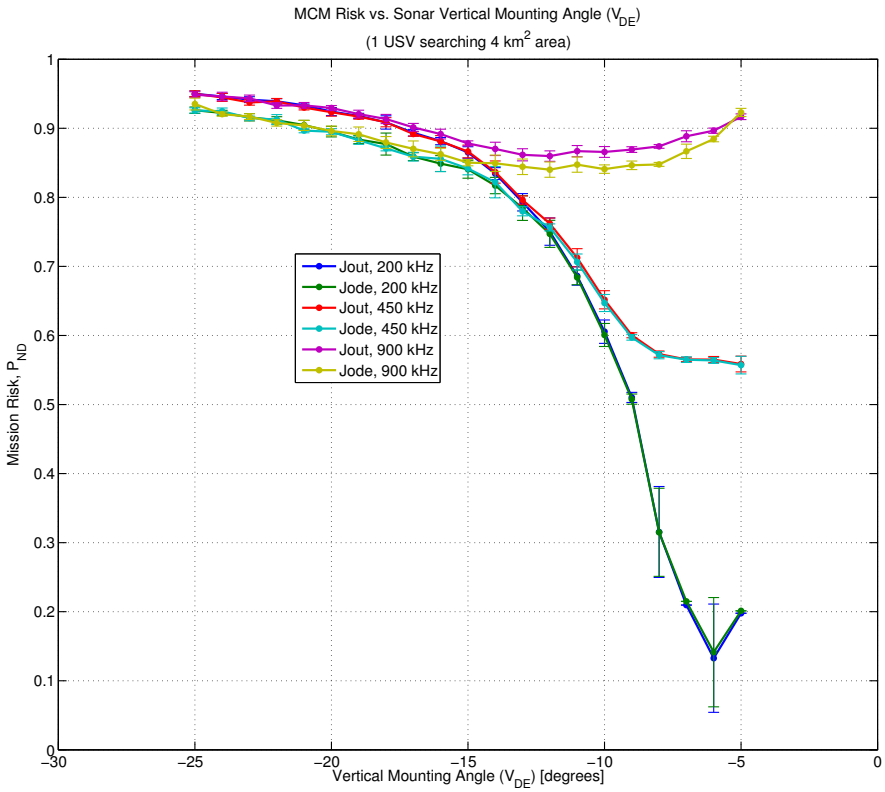

Figure 5.5. Average single-vehicle search performance vs. mounting angle V_{DE}.

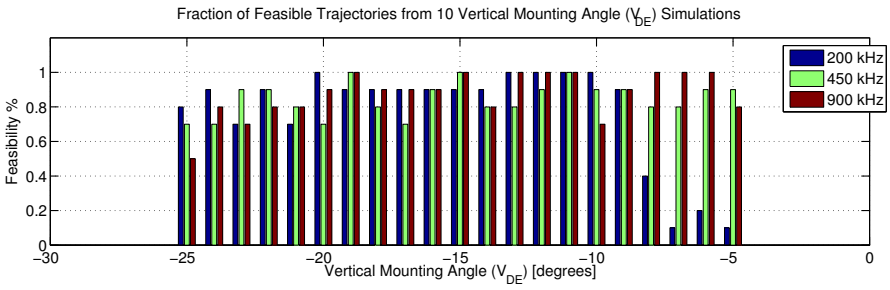

Figure 5.6. Fraction of single-vehicle V_{DE} simulations with feasible trajectories.

5.3.2 Figure of Merit

For each of the three FLS considered in this analysis, V_{DE} was set to the optimal value determined in Section 5.3.1. The other parameter values are listed in Table 5.3, where the bold array notation indicates the range of the independent variable under investigation, i.e., simulations are performed for $FOM = 48, 51, 54, \ldots, 75$ dB. For each of the FOM values listed in Table 5.3, Figure 5.7 plots the mean and standard deviation (depicted by solid lines and error bars, respectively) for the objective values from ten simulations. Figure 5.8 shows the fraction of these search trajectories which meet our feasibility criteria. Search performance for the solver output J_{out} and the ODE-propagated solution J_{ode} (recalculated on our $500 \times 25 \times 25$ discretization baseline) are both provided for comparison purposes.

Table 5.3. Simulation parameters for FOM analysis (free parameters in bold).

Symbol	Definition	Value
T_f	Mission duration [min]	30
N_{sims}	Number of simulation runs	10
N_v	Number of vehicles	1
N_t	Number of time nodes	50
N_ω	Number of parameter nodes	25×25
DU	Canonical distance [m]	100
TU	Canonical time [s]	100
UxV	Vehicle dynamics file	user-selected
f	Sonar operating frequency [kHz]	{200, 450, 900}
FOM	Figure of Merit [dB]	**[48:3:75]**
λ	Poisson Scan rate [scans/s]	0.5 (median value)
σ	Signal excess P_D uncertainty [dB]	9 dB
H_{FOV}	Horizontal field of view [deg]	90 (minimum value)
V_{FOV}	Vertical field of view [deg]	10 (median value)
V_{DE}	Vertical mounting angle [deg]	{-6, -7, -11}

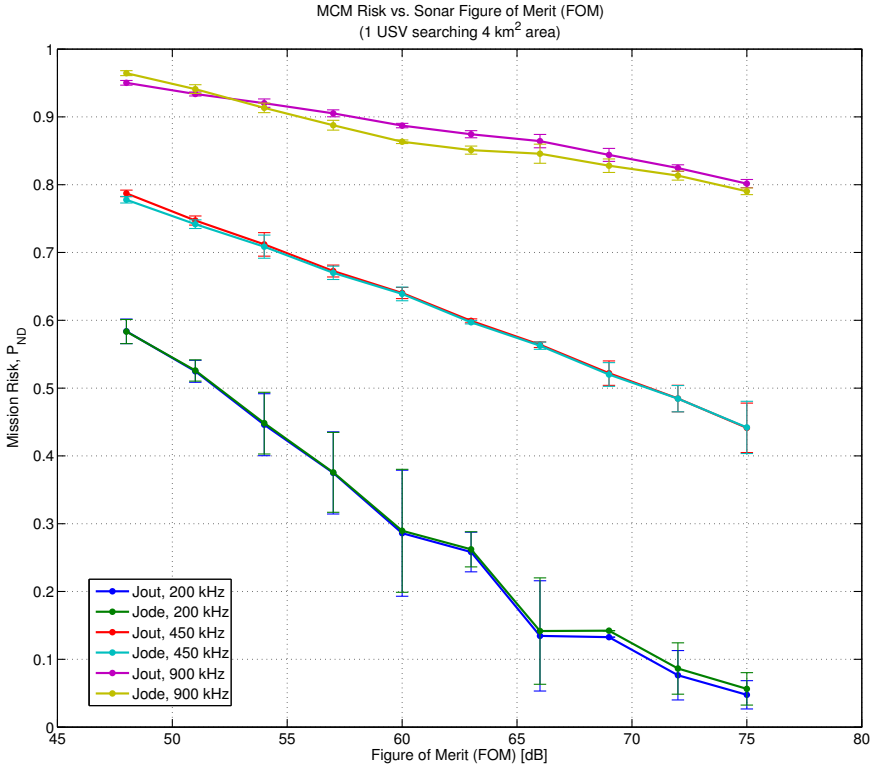

Figure 5.7. Average single-vehicle search performance vs. figure of merit (FOM).

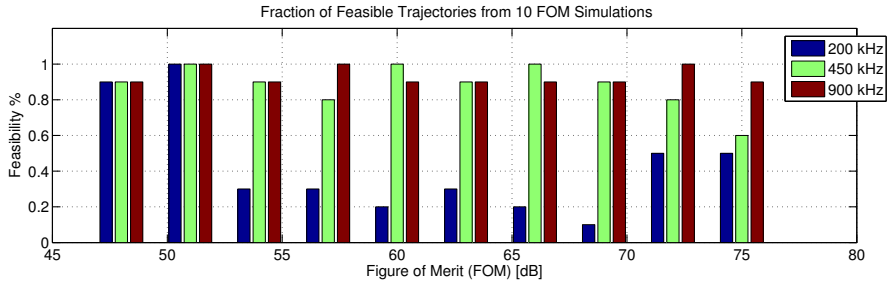

Figure 5.8. Fraction of single-vehicle FOM simulations with feasible trajectories.

As expected, analysis of the FOM parameter for each sonar did not reveal a single optimal value; bigger is better. Since FOM represents the maximum (noise-limited) range at which

echoes are detectable, it makes sense that search performance improves linearly with increasing FOM, especially since propagation losses expressed in dB become linear at long ranges (see Figure 3.1). We observe, however, that the slope of these curves are steeper for the longer-range sonars. This is due to their small mounting angles, which allow the sonar beam to cover more ground before reaching the sea floor. Sonar beams emitted at larger mounting angles reach the sea floor before the sonar can utilize all of the additional detection range produced by the higher FOM .

5.3.3 Poisson Scan Rate

For each of the three FLS considered in this analysis, V_{DE} was set to the optimal value determined in Section 5.3.1. The other parameter values are listed in Table 5.4, where the bold array notation indicates the range of the independent variable under investigation, i.e., simulations are performed for $\lambda = 0.1, 0.2, 0.3, \ldots, 1.0$ scans/second. For each of the λ values listed in Table 5.4, Figure 5.9 plots the mean and standard deviation (depicted by solid lines and error bars, respectively) for the objective values from ten simulations. Figure 5.10 shows the fraction of these search trajectories which meet our feasibility criteria. Search performance for the solver output J_{out} and the ODE-propagated solution J_{ode} (recalculated on our $500 \times 25 \times 25$ discretization baseline) are both provided for comparison purposes.

Table 5.4. Simulation parameters for λ analysis (free parameters in bold).

Symbol	Definition	Value
T_f	Mission duration [min]	30
N_{sims}	Number of simulation runs	10
N_v	Number of vehicles	1
N_t	Number of time nodes	50
N_ω	Number of parameter nodes	25×25
DU	Canonical distance [m]	100
TU	Canonical time [s]	100
UxV	Vehicle dynamics file	user-selected
f	Sonar operating frequency [kHz]	{200, 450, 900}
FOM	Figure of Merit [dB]	66 (median value)
λ	Poisson Scan rate [scans/s]	**[0.1:0.1:1.0]**
σ	Signal excess P_D uncertainty [dB]	9 dB
H_{FOV}	Horizontal field of view [deg]	90 (minimum value)
V_{FOV}	Vertical field of view [deg]	10 (median value)
V_{DE}	Vertical mounting angle [deg]	{-6, -7, -11}

Figure 5.9 reveals the benefit of increasing the number of scans per unit time, but this impact is not as large as expected. Search performance increases rapidly (i.e., P_{ND} decreases) as the Poisson Scan rate λ is increased from its lowest value of 0.1 scans/second to a value of 0.5 scans/second; beyond this value, the benefits of increasing λ begin to diminish. Note that these benefits are greater for the 200 kHz sonar than the higher-frequency models. Figure 5.10 is concerning, however, as more than half of the trajectories produced by this sonar (using 50 time nodes) are infeasible. Additional simulations with fewer time nodes are needed to ascertain the relationship, if any, between higher λ values and infeasible search trajectories for the 200 kHz sonar model.

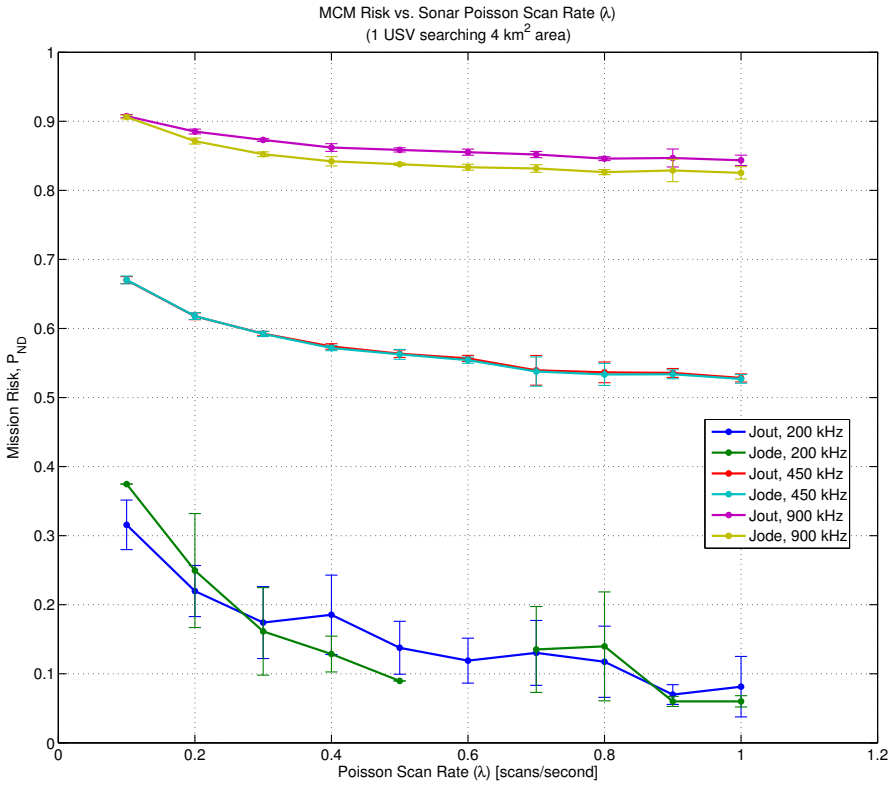

Figure 5.9. Average single-vehicle search performance vs. Poission rate λ.

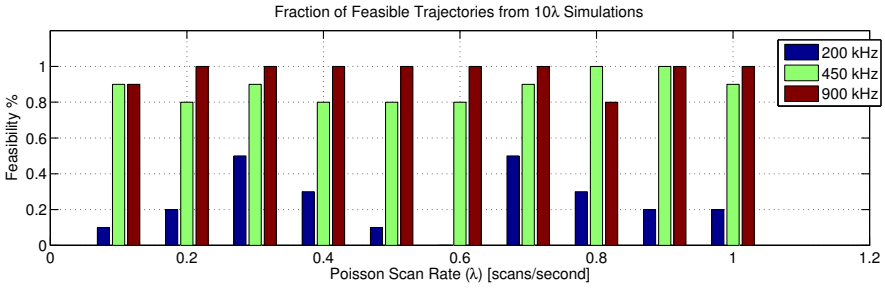

Figure 5.10. Fraction of single-vehicle λ simulations with feasible trajectories.

5.3.4 Horizontal Field of View

For each of the three FLS considered in this analysis, V_{DE} was set to the optimal value determined in Section 5.3.1. The other parameter values are listed in Table 5.5, where the bold array notation indicates the range of the independent variable under investigation, i.e., simulations are performed for $H_{FOV} = 30, 45, 60, \ldots, 165$ degrees. For each of the H_{FOV} values listed, Figure 5.11 plots the mean and standard deviation (depicted by solid lines and error bars, respectively) for the objective values from ten simulations. Figure 5.12 shows the fraction of these search trajectories which meet our feasibility criteria. Search performance for the solver output J_{out} and the ODE-propagated solution J_{ode} (recalculated on our $500 \times 25 \times 25$ discretization baseline) are both provided for comparison purposes.

Table 5.5. Simulation parameters for H_{FOV} analysis (free parameters in bold).

Symbol	Definition	Value
T_f	Mission duration [min]	30
N_{sims}	Number of simulation runs	10
N_v	Number of vehicles	1
N_t	Number of time nodes	50
N_ω	Number of parameter nodes	25×25
DU	Canonical distance [m]	100
TU	Canonical time [s]	100
UxV	Vehicle dynamics file	user-selected
f	Sonar operating frequency [kHz]	{200, 450, 900}
FOM	Figure of Merit [dB]	66 (median value)
λ	Poisson Scan rate [scans/s]	0.5 (median value)
σ	Signal excess P_D uncertainty [dB]	9 dB
H_{FOV}	Horizontal field of view [deg]	**[30:15:165]**
V_{FOV}	Vertical field of view [deg]	10 (median value)
V_{DE}	Vertical mounting angle [deg]	{-6, -7, -11}

Increasing H_{FOV} has a dramatic impact on search performance, effectively increasing the sonar's sweep width and producing faster area coverage rates during a constant velocity survey operation. These benefits can justify the cost of additional staves to increase the

horizontal FOV of a blazed array system. Not coincidentally, maximizing horizontal FOV was a major driver in the design of the ATLAS sonar, which has $H_{FOV} > 180$ degrees.

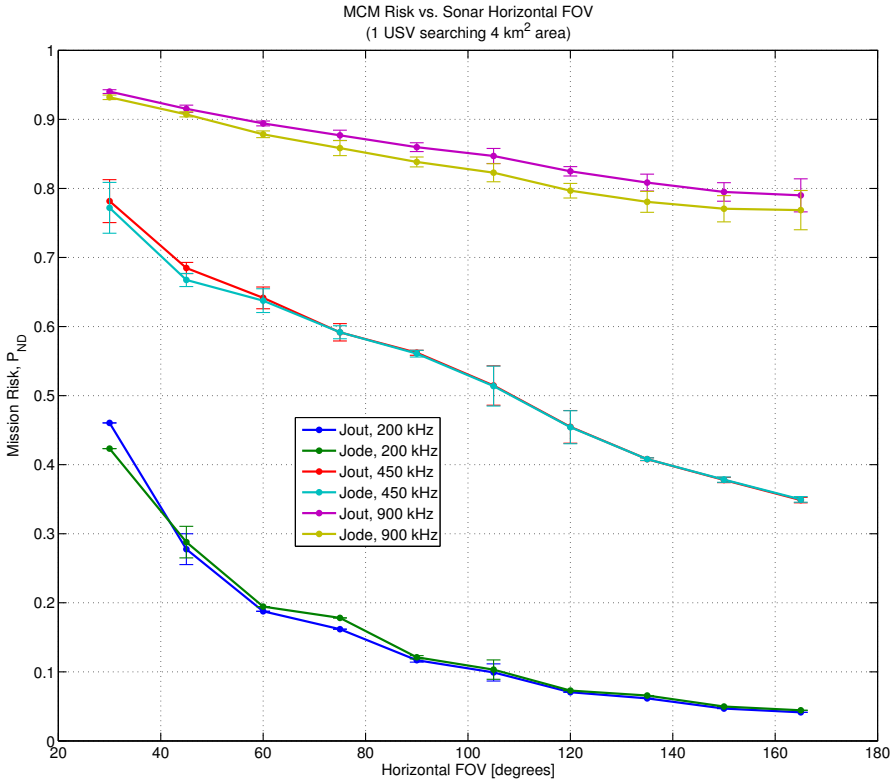

Figure 5.11. Average single-vehicle search performance vs. horizontal field of view (H_{FOV}).

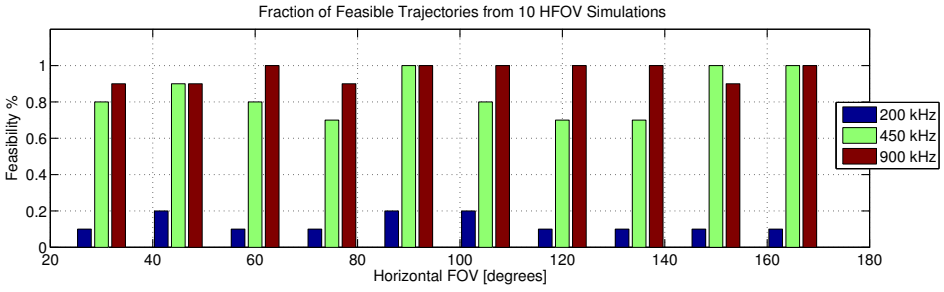

Figure 5.12. Fraction of single-vehicle H_{FOV} simulations with feasible trajectories.

5.4 Multi-Vehicle Search Performance vs. Team Composition

As we have already seen in Section 4.2 it may not be possible to achieve a desired risk threshold with a single search vehicle. If the assets are available, a force commander can simply increase the number of searchers operating in an area. While this solution is straightforward, it may be sub-optimal. Worse yet, this approach can pull needed assets out of another area, slowing the overall MCM operation. Pre-mission analysis can help identify the vehicle and sensor characteristics that produce the best system configuration for a given MCM scenario. The GenOC framework can serve as a pre-mission analysis tool to support these kinds of trade studies. Moreover, the ability to incorporate realistic vehicle and sonar models to optimize mission-specific search objectives can produce more information than planning tools based solely on coverage rates. In this section, we demonstrate our framework's ability to analyze the mission effectiveness of different autonomous vehicle teams conducting the mine detection survey described in Section 4.2. We begin with the simple case of a team comprised of one or more identical search assets, each equipped with the same forward-looking sonar.

5.4.1 Number of Searchers

This analysis compares the search performance for a team of identical SeaFox USVs, all of which are equipped with one of the three different FLS models listed in Table 2.1, where V_{DE} has been set to the optimal value determined in Section 5.3.1. The other parameter values are listed in Table 5.6, where the bold array notation indicates the range of the independent variable under investigation, i.e., simulations are performed for $N_v = 1,2,3,\ldots,5$ search vehicles. For each team configuration listed in Table 5.6, Figure 5.13 depicts the average search performance, while Figure 5.14 shows the number of feasible trajectories produced after ten simulations.

Based on this analysis, me can make the following observations:

- A team of two USVs equipped with the same 450 kHz blazed array FLS outperform a single USV equipped with a 200 kHz cylindrical array FLS. This could realize substantial cost savings, when a commercial off-the-shelf sonar (e.g., a BlueView P450-90) is compared against a developmental sonar like the ATLAS.

Table 5.6. Simulation parameters for multi-USV analysis (free parameters in bold).

Symbol	Definition	Value
T_f	Mission duration [min]	30
N_{sims}	Number of simulation runs	10
N_v	Number of vehicles	**[1:1:5]**
N_t	Number of time nodes	50
N_ω	Number of parameter nodes	25×25
DU	Canonical distance [m]	100
TU	Canonical time [s]	100
UxV	Vehicle dynamics file	user-selected
FLS	Sonar parameters file	user-selected

- Two 200 kHz FLS-equipped searchers are required for complete coverage in the time available, but three 450 kHz FLS-equipped searchers achieve the same search performance. Again, a three-vehicle team using commercial P450-90 sonar may be less expensive to operate than a two-vehicle team using ATLAS-like sonar.
- The 900 kHz sonar performs poorly when mounted on a USV operating in waters this deep. This high-resolution sonar should only be employed by AUVs conducting RID missions, e.g., in Section 4.1.
- Figure 5.14 indicates that optimal solutions for all of the configurations tested produce at least one infeasible trajectory, and the problem is exacerbated as the number of vehicles increase.
- It is important to remember that each data point in a plot like this corresponds to a number of optimal trajectories which can be quickly exploited when needed. This feature of our proposed methodology is emphasized in Figure 5.1.

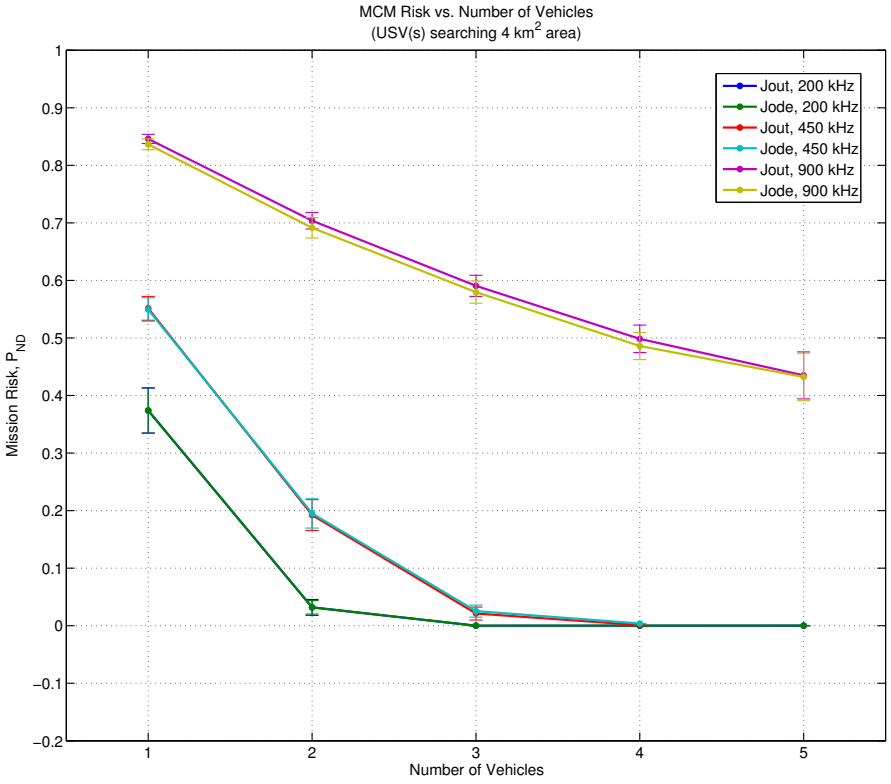

Figure 5.13. Average search performance vs. the number of vehicles on a team.

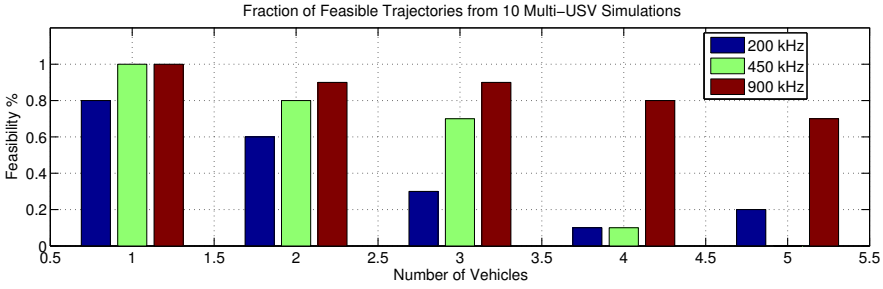

Figure 5.14. Fraction of multi-vehicle simulations that produce feasible trajectories.

CHAPTER 6:
Conclusions and Future Work

6.1 Conclusions

Autonomous vehicles will play an increasingly important role in military operations for the foreseeable future, particularly when danger to personnel is greatest. Mine countermeasures (MCM) is one critical mission area in which these systems have already proven themselves. Driven by the need to detect, identify, and neutralize the threat of underwater mines—in a variety of challenging environments—the U.S. Navy has invested heavily in vehicle and sensor technologies for different MCM missions. This has produced a spectrum of complementary capabilities, most of which have (necessarily) been built around dedicated vehicle platforms or sonar systems. One thrust of current naval research is focused on combining these capabilities via collaborative teams of autonomous vehicles. The goal of this approach is to maximize overall mission effectiveness while overcoming individual system limitations.

Motion planning algorithms for these heterogeneous vehicle teams must consider the capabilities and limitations of each team member. Since many MCM missions involve searching for mines with a specific sonar payload, the current practice is to 1) partition the search area into separate zones according to sensor capabilities, and 2) assign specific vehicle/sonar assets to methodically search each zone using traditional geometric, e.g., lawnmower, coverage patterns. Planning multi-vehicle missions in this manner resembles a scheduling problem in which individual vehicle plans are sequenced and executed according to established area coverage rates. Given sufficient time to conduct a search, these methods do guarantee complete coverage. They are overly conservative, however, and do not exploit the full potential of highly-mobile vehicles to shorten operational timelines or maximize sensor performance. Motivated by new numerical techniques for solving optimal control problems with parameter uncertainty, this dissertation applies these techniques to address sensor-based motion planning for MCM search missions by autonomous vehicle teams.

Optimal control provides a mathematical framework for solving motion planning problems

with dynamic constraints and different performance criteria. Recent advances in numerical solution techniques have made it possible to address parameterized uncertainty in the objective function of an optimal control problem, permitting the direct optimization of search objectives using GenOC. This approach can generate feasible vehicle- and sensor-specific motion trajectories that maximize mine detection probabilities under operational constraints. However, realistic vehicle and sensor models are essential to producing operationally relevant results.

Chapter 2 of this dissertation develops physics-based probabilistic detection models for various mine hunting sonars currently employed for MCM missions. In these models, detection performance is not only a function of the sonar's design criteria but also the three-dimensional trajectory executed by the search vehicle. Although simplifying assumptions are made to facilitate rapid calculations during trajectory optimization, the simulated detection performance of these models agrees with expectations from actual sonar systems. Therefore, they represent a good compromise between the traditional detection models used in search theory, and full-scale acoustic simulators used for sonar design and performance prediction.

In Chapter 3, we describe how various MCM missions can be formulated as optimal search problems in the GenOC framework. Chapter 4 highlights the flexibility of our modular approach by generating motion plans for MCM wide area survey and target reacquisition missions via different combinations of searcher, sensor, and target distribution models. Optimal search techniques are particularly useful for creating sensor-based trajectories which outperform conventional coverage patterns under resource or time constraints. Examples are provided in Chapter 4 that illustrate how optimal solutions can be used to establish new performance benchmarks for a given scenario. This makes GenOC an attractive tool for pre-mission analysis as well.

A novel contribution of this dissertation applies GenOC to investigate inverse problems relating MCM mission performance to specific sonar designs or employment methods. Chapter 5 describes an approach for rapidly solving a range of optimal search problems in this framework to support Monte Carlo analysis of alternative configurations. This approach is used to determine the best discretization level for accurate, yet feasible solutions in a given scenario. Based on this result, additional Monte Carlo experiments are conducted to

analyze search performance relative to various sonar design parameters, highlighting the utility of this approach.

6.2 Recommendations for Future Work

This dissertation represents the first application of GenOC to operationally relevant motion planning problems in mine countermeasures. The derivation of physics-based models that incorporate design characteristics and three-dimensional detection performance of actual sonar systems has opened the door to a wide array of important analysis questions, and this dissertation only scratches the surface. We have demonstrated the utility of the GenOC framework for analyzing several questions of immediate interest to the MCM community, but a number of avenues remain open for future work.

First, additional analysis is needed to investigate test cases from Chapter 5 that produced relatively low fractions of feasible solutions. This was more prevalent in simulations which utilized the 200 kHz FLS model. Repeating these experiments with fewer time nodes may produce more feasible trajectories. Whereas variation was added to these simulations via the initial condition, additional experiments could inject random variation into the "shape" of an initial guess trajectory. This approach may produce more globally optimal solutions by exploring more of the state space during a given Monte Carlo simulation. Another technique worth investigating is a two-step process whereby an optimal trajectory from one simulation is used as the initial guess for a second simulation. We regard all of these suggestions as low-hanging fruit. At a minimum, however, increasing the total number of simulations is recommended in order to produce more statistically-significant analytic results.

As mentioned in Section 4.3, the computational framework used for this dissertation is designed around solving fixed-time optimal control problems. While this problem formulation can address time-limited missions directly, it requires additional effort to analyze explicit questions about time, e.g., how long would it take a team of vehicles to achieve a risk threshold of 5%? Currently, this requires a Monte Carlo analysis of simulations with an array of T_f values to provide an approximate solution. Future work will assess the ability of other optimal control software packages like DIDO to solve minimum-time versions of optimal search problems for MCM. This software can also facilitate a more detailed

sensitivity analysis of inverse problems using the approach referenced in Section 5.1.

This dissertation has presented results highlighting some of the trade-offs associated with selecting a discretization scheme to numerically solve optimal search problems defined in continuous time and space. This has proved especially challenging for the sidescan sonar models developed in Chapter 2, which are characterized by a very high Poisson Scan rate (λ) and a very narrow horizontal field of view (H_{FOV}). Initial simulation results with these sensor models require an exceedingly large number of time nodes to produce accurate area coverage, and this can make numerical solutions intractable for complex motion planning problems. Since SSS is so widely used in underwater search applications, future work will continue to address this modeling challenge.

An interesting avenue for future work is investigating ways to exploit the capabilities of AUVs and FLS to execute three-dimensional trajectories for mine detection. The solution framework readily supports vehicle dynamics with arbitrary degrees of freedom, and the sensor models developed in this dissertation already operate in three-dimensional space. Thus far, however, we have only considered search trajectories in a two-dimensional plane, in keeping with current MCM practices. For this reason, we consider the exploration of three-dimensional search trajectories to be high-risk, high reward, since a rigorous analysis of this approach could potentially improve MCM CONOPS—especially against moored or in-volume mines.

The preceding recommendations can all be addressed with minimal changes by the current GenOC framework. The following suggestions would require significantly more effort, but would make important contributions. Perhaps most egregious to sonar practitioners, our current implementation does not address environmental impacts (beyond propagation losses) on sonar performance. Operational relevance can be greatly improved by incorporating reverberation effects, sea floor characteristics, and sound speed profiles into the sonar detection models. A significant challenge, however, is the computational effort required by this additional complexity, since sonar detection calculations occur in the inner loop of the optimization algorithm. Again, we seek a balance between over-simplified "cookie cutter" detection models, and sonar performance simulations that take hours (or days!) to execute.

Even with the simplified detection models used in this dissertation, current algorithms are not yet practical for real-time trajectory generation by vehicle autopilots. The current ap-

proach is better suited to pre-mission analysis in order to establish performance benchmarks and facilitate CONOPS development. Optimal motion plans generated by the solver are essentially open loop mission profiles that must be implemented separately by each vehicle. Future work to enable real-time computation and periodic re-planning of optimal search trajectories are key to transitioning this technology for use on actual MCM vehicles.

Periodic re-planning would also allow vehicles to perform Bayesian updates on the underlying target distribution model, in response to detection events, and reallocate search effort more efficiently. This capability could be enhanced via wireless radio or acoustic communications between vehicles, allowing MCM teams to conduct survey missions and RID missions concurrently. This could realize significant time savings over current practice, which conducts these MCM operations in sequential phases. It could also pave the way for mission plans which incorporate more complex vehicle interactions, e.g., the rapid transport of AUVs to and from an operating area by USV or helicopter to minimize the time wasted during slow-speed transits.

THIS PAGE INTENTIONALLY LEFT BLANK

APPENDIX A:
Objective Function Gradients

A.1 Objective Function Gradients

The SNOPT numeric optimization package can solve an optimal search problem more quickly and reliably when it is supplied with analytic expressions for the objective function's gradients [99]. For our problem, we must derive gradients with respect to the state variables $\partial J/\partial \vec{x}$ and control inputs $\partial J/\partial \vec{u}$ for the objective function given by Equation (3.11). We encode optimal search problems for SNOPT using a MATLAB interface developed by Claire Walton. This interface, Software for Parameter-uncertainty Optimal Control (SPOC), conveniently allows users to specify separate gradients for the inner, $R(t) = \gamma(\vec{x}(t),\vec{\omega})$, and outer, $G(z) = e^{-z}$, components of a GenOC problem's running cost in Equation (1.2) [79]. Since $\partial G/\partial z$ has the trivial expression $-e^{-z}$, and $\partial\gamma/\partial\vec{u} = 0$ for this problem, the following section derives $\partial R/\partial \vec{x}$ only. These gradients are based on components defined in Chapter 2 for the instantaneous detection rate of Equation (2.22). Note that all variables are assumed to be in canonical, non-dimensional form, but the overline notation used in Section 3.5 is not used here. Likewise, the searcher states' dependence on time is omitted to simplify the notation.

Recall that $\gamma(\vec{x},\vec{\omega}) = \lambda p(\vec{x},\vec{\omega})F_\alpha(\vec{x},\vec{\omega})F_\varepsilon(\vec{x},\vec{\omega})F_r(\vec{x})$. Each term in this equation except the constant Poisson Scan rate λ depends on the state vector $[x, y, \psi, r]^T$. Therefore, the gradient is

$$\frac{\partial R}{\partial \vec{x}} = \frac{\partial \gamma}{\partial \vec{x}} = \begin{bmatrix} \frac{\partial \gamma}{\partial x} & \frac{\partial \gamma}{\partial y} & \frac{\partial \gamma}{\partial \psi} & \frac{\partial \gamma}{\partial r} \end{bmatrix}. \tag{A.1}$$

We can apply the product rule to calculate each element of the objective function gradient:

$$\begin{aligned}
\frac{\partial \gamma}{\partial x} &= \lambda \left(\frac{\partial p}{\partial x} F_\alpha F_\varepsilon F_r + p \frac{\partial F_\alpha}{\partial x} F_\varepsilon F_r + p F_\alpha \frac{\partial F_\varepsilon}{\partial x} F_r + p F_\alpha F_\varepsilon \frac{\partial F_r}{\partial x} \right) \\
\frac{\partial \gamma}{\partial y} &= \lambda \left(\frac{\partial p}{\partial y} F_\alpha F_\varepsilon F_r + p \frac{\partial F_\alpha}{\partial y} F_\varepsilon F_r + p F_\alpha \frac{\partial F_\varepsilon}{\partial y} F_r + p F_\alpha F_\varepsilon \frac{\partial F_r}{\partial y} \right) \\
\frac{\partial \gamma}{\partial \psi} &= \lambda \left(\frac{\partial p}{\partial \psi} F_\alpha F_\varepsilon F_r + p \frac{\partial F_\alpha}{\partial \psi} F_\varepsilon F_r + p F_\alpha \frac{\partial F_\varepsilon}{\partial \psi} F_r + p F_\alpha F_\varepsilon \frac{\partial F_r}{\partial \psi} \right) \\
\frac{\partial \gamma}{\partial r} &= \lambda \left(\frac{\partial p}{\partial r} F_\alpha F_\varepsilon F_r + p \frac{\partial F_\alpha}{\partial r} F_\varepsilon F_r + p F_\alpha \frac{\partial F_\varepsilon}{\partial r} F_r + p F_\alpha F_\varepsilon \frac{\partial F_r}{\partial r} \right).
\end{aligned} \tag{A.2}$$

The following sections derive the expressions for $\partial p/\partial \vec{x}$, $\partial F_\alpha/\partial \vec{x}$, $\partial F_\varepsilon/\partial \vec{x}$, and $\partial F_r/\partial \vec{x}$.

A.2 Gradients for Instantaneous Probability of Detection ($\partial p/\partial \vec{x}$)

Recall from Equation (2.3) that $SE(\vec{x},\vec{\omega}) = FOM - PL\left(D(\vec{x},\vec{\omega})\right)$, where $PL\left(D(\vec{x},\vec{\omega})\right)$ is the propagation loss as a function of the distance between searcher and target, $D(\vec{x},\vec{\omega})$. Substituting into Equation (2.8) yields

$$p(\vec{x},\vec{\omega}) = \Phi\left(\frac{SE\left(\vec{x},\vec{\omega}\right)}{\sigma}\right) = \Phi\left(\frac{FOM - PL\left(D(\vec{x},\vec{\omega})\right)}{\sigma}\right) = \Phi\left(\xi\right). \tag{A.3}$$

Letting $\xi = (FOM - PL)/\sigma$, we can rewrite the cumulative normal distribution function $\Phi(\xi)$ in terms of the *erf* function, which yields

$$\Phi\left(\xi\right) = \frac{1}{2}\left[1 + \operatorname{erf}\left(\frac{\xi}{\sqrt{2}}\right)\right]. \tag{A.4}$$

We can now use the chain rule to derive $\partial p/\partial x$ as

$$\frac{\partial p}{\partial x} = \frac{\partial p}{\partial \xi}\frac{\partial \xi}{\partial PL}\frac{\partial PL}{\partial D}\frac{\partial D}{\partial x}. \tag{A.5}$$

Using the analytic expression for the derivative of the *erf* function, we compute $\partial p/\partial \xi$ as

$$\frac{\partial p}{\partial \xi} = \frac{1}{\sqrt{2\pi}} e^{-\frac{1}{2}\xi^2} = \frac{1}{\sqrt{2\pi}} e^{-\frac{1}{2}\left(\frac{FOM-PL}{\sigma}\right)^2}. \tag{A.6}$$

Meanwhile, using our definition for ξ, we compute:

$$\frac{\partial \xi}{\partial PL} = -\frac{1}{\sigma}. \tag{A.7}$$

Using $D = \|\vec{\omega} - \vec{x}\| = \sqrt{(\omega_x - x)^2 + (\omega_y - y)^2 + (\omega_z - z)^2} = \sqrt{dx^2 + dy^2 + dz^2}$ from Equation (3.22), and $PL = 20\log_{10}(DU) + 20\log_{10}(D) + aD$ from Equation (3.26), we compute $\partial PL/\partial D$ and $\partial D/\partial x$ as follows:

$$\begin{aligned}
\frac{\partial PL}{\partial D} &= \frac{\partial}{\partial D}\left[\cancelto{0}{20\log_{10}(DU)} + 20\log_{10}(D) + aD\right] \\
&= \frac{\partial}{\partial D}\left[20\frac{\ln(D)}{\ln(10)} + aD\right] \\
&= \frac{\partial}{\partial D}\left[\frac{20}{\ln(10)}\ln(D) + aD\right] \\
&= \frac{20}{\ln(10)}\left(\frac{1}{D}\right) + a, \text{ and}
\end{aligned} \tag{A.8}$$

$$\begin{aligned}
\frac{\partial D}{\partial x} &= \frac{\partial}{\partial x}\left(\sqrt{(\omega_x - x)^2 + (\omega_y - y)^2 + (\omega_z - z)^2}\right) \\
&= \frac{1}{2}\frac{2(\omega_x - x)(-1)}{\sqrt{(\omega_x - x)^2 + (\omega_y - y)^2 + (\omega_z - z)^2}} \\
&= -\frac{dx}{D}.
\end{aligned} \tag{A.9}$$

Finally, we substitute Equations (A.6) through (A.9) into Equation (A.5) to obtain

$$\begin{aligned}
\frac{\partial p}{\partial x} &= \frac{dx}{\sigma D\sqrt{2\pi}}\left[\frac{20}{\ln(10)}\left(\frac{1}{D}\right) + a\right] e^{-\frac{1}{2}\left(\frac{F-PL}{\sigma}\right)^2} \\
&= \frac{dx}{\sigma\sqrt{2\pi}}\left[\frac{20 + aD\ln(10)}{D^2\ln(10)}\right] e^{-\frac{1}{2}\left(\frac{F-PL}{\sigma}\right)^2}.
\end{aligned} \tag{A.10}$$

In a similar manner, using $\partial D/\partial y = -dy/D$, we can compute $\partial p/\partial y$ as

$$\frac{\partial p}{\partial y} = \frac{\partial p}{\partial \xi}\frac{\partial \xi}{\partial PL}\frac{\partial PL}{\partial D}\frac{\partial D}{\partial y} = \frac{dy}{\sigma\sqrt{2\pi}}\left[\frac{20 + aD\ln(10)}{D^2\ln(10)}\right] e^{-\frac{1}{2}\left(\frac{F-PL}{\sigma}\right)^2}. \tag{A.11}$$

Moreover, $\partial p/\partial \psi = \partial p/\partial r = 0$ since $p(\vec{x}, \vec{\omega})$ is a function of distance only.

A.3 Gradients for Azimuth Angle Shaping Function $(\partial F_\alpha / \partial \vec{x})$

Recall from Equation (2.15) that $F_\alpha(\vec{x}, \vec{\omega})$ is based on the body-fixed azimuth angle ${}^b\alpha$, which depends upon the states x, y, and ψ as shown in Equations (2.10) through (2.12), but is independent of turn rate r, i.e., $\partial F_\alpha / \partial r = 0$. We can rewrite Equation (2.15) as

$$F_\alpha = F_{\alpha_L} + F_{\alpha_U} - 1, \tag{A.12}$$

where:

$$F_{\alpha_L} = \frac{1}{1 + e^{p_\alpha(\alpha_L - \alpha)}} = \frac{1}{A_L}, \text{ and} \tag{A.13}$$

$$F_{\alpha_U} = \frac{1}{1 + e^{p_\alpha(\alpha - \alpha_U)}} = \frac{1}{A_U}. \tag{A.14}$$

Note that the body-fixed superscript b has been omitted from the azimuth angle α to simplify notation. We can now use the chain rule to derive $\partial F_\alpha / \partial x$ as

$$\frac{\partial F_\alpha}{\partial x} = \frac{\partial F_\alpha}{\partial A_L}\frac{\partial A_L}{\partial \alpha}\frac{\partial \alpha}{\partial x} + \frac{\partial F_\alpha}{\partial A_U}\frac{\partial A_U}{\partial \alpha}\frac{\partial \alpha}{\partial x} = \left(\frac{\partial F_\alpha}{\partial A_L}\frac{\partial A_L}{\partial \alpha} + \frac{\partial F_\alpha}{\partial A_U}\frac{\partial A_U}{\partial \alpha}\right)\frac{\partial \alpha}{\partial x}, \tag{A.15}$$

where:

$$\frac{\partial F_\alpha}{\partial A_L} = -\frac{1}{A_L^2} = -\frac{1}{\left[1 + e^{p_\alpha(\alpha_L - \alpha)}\right]^2}, \tag{A.16}$$

$$\frac{\partial F_\alpha}{\partial A_U} = -\frac{1}{A_U^2} = -\frac{1}{\left[1 + e^{p_\alpha(\alpha - \alpha_U)}\right]^2}, \tag{A.17}$$

$$\frac{\partial A_L}{\partial \alpha} = \frac{\partial}{\partial \alpha}\left[1 + e^{p_\alpha(\alpha_L - \alpha)}\right] = -p_\alpha e^{p_\alpha(\alpha_L - \alpha)}, \tag{A.18}$$

$$\frac{\partial A_U}{\partial \alpha} = \frac{\partial}{\partial \alpha}\left[1 + e^{p_\alpha(\alpha - \alpha_U)}\right] = p_\alpha e^{p_\alpha(\alpha - \alpha_U)}, \tag{A.19}$$

and:

$$\frac{\partial \alpha}{\partial x} = \frac{\partial}{\partial x}\text{atan2}({}^b dy, {}^b dx) = \frac{\partial}{\partial x}\text{atan2}({}^n dy, {}^n dx) = \frac{\partial}{\partial x}\arctan\left(\frac{dy}{dx}\right). \tag{A.20}$$

Letting $\varphi = dy/dx$, we can compute the derivative of the inverse tangent function with respect to x as

$$\frac{\partial}{\partial x}\arctan(\varphi) = \left(\frac{1}{1+\varphi^2}\right)\frac{\partial \varphi}{\partial x} = \left(\frac{dx^2}{dx^2+dy^2}\right)\frac{\partial \varphi}{\partial x}. \tag{A.21}$$

Meanwhile, since $dx = \omega_x - x$, the derivative of φ with respect to x is

$$\frac{\partial \varphi}{\partial x} = \frac{\partial}{\partial x}\left(\frac{dy}{dx}\right) = -\frac{dy}{dx^2}(-1) = \frac{dy}{dx^2}. \tag{A.22}$$

Substituting Equations (A.21) and (A.22) into Equation (A.20) yields

$$\frac{\partial \alpha}{\partial x} = \left(\frac{dx^2}{dx^2+dy^2}\right)\frac{dy}{dx^2} = \frac{dy}{dx^2+dy^2}. \tag{A.23}$$

Letting $E_{\alpha_L} = e^{p_\alpha(\alpha_L - \alpha)}$ and $E_{\alpha_U} = e^{p_\alpha(\alpha - \alpha_U)}$, we substitute Equations (A.16) through (A.19), with Equation (A.23), into Equation (A.15) and obtain

$$\frac{\partial F_\alpha}{\partial x} = \frac{p_\alpha dy}{dx^2+dy^2}\left[\frac{E_{\alpha_L}}{(1+E_{\alpha_L})^2} - \frac{E_{\alpha_U}}{(1+E_{\alpha_U})^2}\right]. \tag{A.24}$$

In a similar manner:

$$\frac{\partial F_\alpha}{\partial y} = \frac{\partial F_\alpha}{\partial A_L}\frac{\partial A_L}{\partial \alpha}\frac{\partial \alpha}{\partial y} + \frac{\partial F_\alpha}{\partial A_U}\frac{\partial A_U}{\partial \alpha}\frac{\partial \alpha}{\partial y} = \left(\frac{\partial F_\alpha}{\partial A_L}\frac{\partial A_L}{\partial \alpha} + \frac{\partial F_\alpha}{\partial A_U}\frac{\partial A_U}{\partial \alpha}\right)\frac{\partial \alpha}{\partial y}, \text{ and} \tag{A.25}$$

$$\frac{\partial \alpha}{\partial y} = \frac{\partial}{\partial y}\text{atan2}({}^b dy, {}^b dx) = \frac{\partial}{\partial y}\text{atan2}({}^n dy, {}^n dx) = \frac{\partial}{\partial y}\arctan\left(\frac{dy}{dx}\right). \tag{A.26}$$

Once again, we let $\varphi = dy/dx$ and compute the derivative of the inverse tangent function with respect to y as

$$\frac{\partial}{\partial y}\arctan(\varphi) = \left(\frac{1}{1+\varphi^2}\right)\frac{\partial \varphi}{\partial y} = \left(\frac{dx^2}{dx^2+dy^2}\right)\frac{\partial \varphi}{\partial y}. \tag{A.27}$$

Meanwhile, since $dy = \omega_y - y$, the derivative of φ with respect to y is

$$\frac{\partial \varphi}{\partial y} = \frac{\partial}{\partial y}\left(\frac{dy}{dx}\right) = \frac{1}{dx}(-1) = -\frac{1}{dx}. \tag{A.28}$$

Substituting Equations (A.27) and (A.28) into Equation (A.26) yields

$$\frac{\partial \alpha}{\partial y} = \left(\frac{dx^2}{dx^2 + dy^2}\right)\left(-\frac{1}{dx}\right) = -\frac{dx}{dx^2 + dy^2}. \tag{A.29}$$

Using the same definitions for E_{α_L} and E_{α_U}, we substitute Equations (A.16) through (A.19), with Equation (A.29), into Equation (A.25) and obtain

$$\frac{\partial F_\alpha}{\partial y} = -\frac{p_\alpha dx}{dx^2 + dy^2}\left[\frac{E_{\alpha_L}}{(1 + E_{\alpha_L})^2} - \frac{E_{\alpha_U}}{(1 + E_{\alpha_U})^2}\right]. \tag{A.30}$$

The derivation of $\partial F_\alpha / \partial \psi$ proceeds similarly, as follows:

$$\frac{\partial F_\alpha}{\partial \psi} = \frac{\partial F_\alpha}{\partial A_L}\frac{\partial A_L}{\partial \alpha}\frac{\partial \alpha}{\partial \psi} + \frac{\partial F_\alpha}{\partial A_U}\frac{\partial A_U}{\partial \alpha}\frac{\partial \alpha}{\partial \psi} = \left(\frac{\partial F_\alpha}{\partial A_L}\frac{\partial A_L}{\partial \alpha} + \frac{\partial F_\alpha}{\partial A_U}\frac{\partial A_U}{\partial \alpha}\right)\frac{\partial \alpha}{\partial \psi}. \tag{A.31}$$

However, note that $\partial^b \alpha / \partial \psi \neq \partial^n \alpha / \partial \psi$, and we must use the azimuth angle resolved in body-fixed coordinates, which is given by

$$\frac{\partial^b \alpha}{\partial \psi} = \frac{\partial}{\partial \psi}\text{atan2}({}^b dy, {}^b dx) = \frac{\partial}{\partial \psi}\arctan\left(\frac{{}^b dy}{{}^b dx}\right). \tag{A.32}$$

Referencing Figure 2.8, we can expose this function's dependence on ψ by letting

$$\beta(\psi) = \frac{{}^b dy}{{}^b dx} = \frac{{}^n dy\cos(\psi) \; - \; {}^n dx\sin(\psi)}{{}^n dx\cos(\psi) \; + \; {}^n dy\sin(\psi)}. \tag{A.33}$$

Using the chain rule, Equation (A.32) becomes

$$\frac{\partial^b \alpha}{\partial \psi} = \frac{\partial}{\partial \psi}\arctan\left(\beta(\psi)\right) = \frac{\partial}{\partial \beta}\arctan(\beta)\frac{\partial \beta}{\partial \psi}. \tag{A.34}$$

The derivative of the inverse tangent function is

$$\frac{\partial}{\partial \beta} \arctan(\beta) = \frac{1}{1+\beta^2} = \frac{\left[{}^{n}dx\cos(\psi) \;+\; {}^{n}dy\sin(\psi)\right]^2}{{}^{n}dx^2 \;+\; {}^{n}dy^2}, \tag{A.35}$$

while the derivative of its argument β is

$$\begin{aligned}
\frac{\partial \beta}{\partial \psi} &= \frac{\partial}{\partial \psi}\left[\frac{{}^{n}dy\cos(\psi) \;-\; {}^{n}dx\sin(\psi)}{{}^{n}dx\cos(\psi) \;+\; {}^{n}dy\sin(\psi)}\right] \\
&= \frac{\left[{}^{n}dy\cos(\psi) \;-\; {}^{n}dx\sin(\psi)\right]\left[-\,{}^{n}dx\sin(\psi) \;+\; {}^{n}dy\cos(\psi)\right]}{\left[\,{}^{n}dx\cos(\psi) \;+\; {}^{n}dy\sin(\psi)\right]^2} \\
&\quad + \frac{\left[-\,{}^{n}dy\sin(\psi) \;-\; {}^{n}dx\cos(\psi)\right]\left[\,{}^{n}dx\cos(\psi) \;+\; {}^{n}dy\sin(\psi)\right]}{\left[{}^{n}dx\cos(\psi) \;+\; {}^{n}dy\sin(\psi)\right]^2} \\
&= -\frac{\left[\,{}^{n}dy\cos(\psi) \;-\; {}^{n}dx\sin(\psi)\right]^2 + \left[\,{}^{n}dx\cos(\psi) \;+\; {}^{n}dy\sin(\psi)\right]^2}{\left[{}^{n}dx\cos(\psi) \;+\; {}^{n}dy\sin(\psi)\right]^2} \\
&= -\frac{{}^{n}dy^2\cos^2(\psi) \;+\; {}^{n}dx^2\sin^2(\psi) + {}^{n}dx^2\cos^2(\psi) \;+\; {}^{n}dy^2\sin^2(\psi)}{\left[{}^{n}dx\cos(\psi) \;+\; {}^{n}dy\sin(\psi)\right]^2} \\
&= -\frac{{}^{n}dx^2\left[\cos^2(\psi)+\sin^2(\psi)\right] \;+\; {}^{n}dy^2\left[\cos^2(\psi)+\sin^2(\psi)\right]}{\left[{}^{n}dx\cos(\psi) \;+\; {}^{n}dy\sin(\psi)\right]^2} \\
&= -\frac{{}^{n}dx^2 \;+\; {}^{n}dy^2}{\left[{}^{n}dx\cos(\psi) \;+\; {}^{n}dy\sin(\psi)\right]^2}.
\end{aligned} \tag{A.36}$$

When we combine Equation (A.35) and Equation (A.36) under the chain rule in Equation (A.34), the partial derivative of azimuth angle with respect to heading angle ψ simplifies to

$$\frac{\partial^b \alpha}{\partial \psi} = -\frac{\left[{}^{n}dx\cos(\psi) \;+\; {}^{n}dy\sin(\psi)\right]^2}{{}^{n}dx^2 \;+\; {}^{n}dy^2} \cdot \frac{{}^{n}dx^2 \;+\; {}^{n}dy^2}{\left[{}^{n}dx\cos(\psi) \;+\; {}^{n}dy\sin(\psi)\right]^2} = -1. \tag{A.37}$$

Since the z-axes of the inertial and body-fixed reference frames are parallel, azimuth angles in both coordinate systems can be related by ${}^{b}\alpha \;=\; {}^{n}\alpha - \psi$, as shown in Figure 2.8. From this relation, $\partial^b \alpha / \partial \psi = -1$, which is consistent with Equation (A.37). The gradient $\partial F_\alpha / \partial \psi$ in Equation (A.31) therefore simplifies to

$$\frac{\partial F_\alpha}{\partial \psi} = -p_\alpha \left[\frac{E_{\alpha_L}}{\left(1+E_{\alpha_L}\right)^2} - \frac{E_{\alpha_U}}{\left(1+E_{\alpha_U}\right)^2}\right]. \tag{A.38}$$

A.4 Gradients for Elevation Angle Shaping Function $(\partial F_\varepsilon / \partial \vec{x})$

Recall from equation Equation (2.16) that $F_\varepsilon(\vec{x}, \vec{\omega})$ is based on the elevation angle ε, which depends upon the states x and y as shown in Equation (2.14), but is independent of heading ψ and turn rate r, i.e., $\partial F_\varepsilon / \partial \psi = \partial F_\varepsilon / \partial r = 0$. We can rewrite Equation (2.16) as

$$F_\varepsilon = F_{\varepsilon_L} + F_{\varepsilon_U} - 1, \tag{A.39}$$

where:

$$F_{\varepsilon_L} = \frac{1}{1 + e^{p_\varepsilon(\varepsilon_L - \varepsilon)}} = \frac{1}{E_L}, \text{ and} \tag{A.40}$$

$$F_{\varepsilon_U} = \frac{1}{1 + e^{p_\varepsilon(\varepsilon - \varepsilon_U)}} = \frac{1}{E_U}. \tag{A.41}$$

Note that elevation angle ε is identical in both the inertial and body-fixed reference frames, so superscripts are omitted to simplify notation. We can now use the chain rule to derive $\partial F_\varepsilon / \partial x$ as follows:

$$\frac{\partial F_\varepsilon}{\partial x} = \frac{\partial F_\varepsilon}{\partial E_L}\frac{\partial E_L}{\partial \varepsilon}\frac{\partial \varepsilon}{\partial x} + \frac{\partial F_\varepsilon}{\partial E_U}\frac{\partial E_U}{\partial \varepsilon}\frac{\partial \varepsilon}{\partial x} = \left(\frac{\partial F_\varepsilon}{\partial E_L}\frac{\partial E_L}{\partial \varepsilon} + \frac{\partial F_\varepsilon}{\partial E_U}\frac{\partial E_U}{\partial \varepsilon}\right)\frac{\partial \varepsilon}{\partial x}, \tag{A.42}$$

where:

$$\frac{\partial F_\varepsilon}{\partial E_L} = -\frac{1}{E_L^2} = -\frac{1}{\left[1 + e^{p_\varepsilon(\varepsilon_L - \varepsilon)}\right]^2}, \tag{A.43}$$

$$\frac{\partial F_\varepsilon}{\partial E_U} = -\frac{1}{E_U^2} = -\frac{1}{\left[1 + e^{p_\varepsilon(\varepsilon - \varepsilon_U)}\right]^2}, \tag{A.44}$$

$$\frac{\partial E_L}{\partial \varepsilon} = \frac{\partial}{\partial \varepsilon}\left[1 + e^{p_\varepsilon(\varepsilon_L - \varepsilon)}\right] = -p_\varepsilon e^{p_\varepsilon(\varepsilon_L - \varepsilon)}, \tag{A.45}$$

$$\frac{\partial E_U}{\partial \varepsilon} = \frac{\partial}{\partial \varepsilon}\left[1 + e^{p_\varepsilon(\varepsilon - \varepsilon_U)}\right] = p_\varepsilon e^{p_\varepsilon(\varepsilon - \varepsilon_U)}, \text{ and} \tag{A.46}$$

$$\frac{\partial \varepsilon}{\partial x} = \frac{\partial}{\partial x}\arctan\left(\frac{-dz}{\sqrt{dx^2 + dy^2}}\right). \tag{A.47}$$

Letting $\zeta = -dz/\sqrt{dx^2 + dy^2}$, we can compute the derivative of the inverse tangent function with respect to x as

$$\frac{\partial}{\partial x}\arctan(\zeta) = \left(\frac{1}{1+\zeta^2}\right)\frac{\partial \zeta}{\partial x} = \left(\frac{dx^2+dy^2}{dx^2+dy^2+dz^2}\right)\frac{\partial \zeta}{\partial x} = \left(\frac{dx^2+dy^2}{D^2}\right)\frac{\partial \zeta}{\partial x}. \tag{A.48}$$

Meanwhile, since $dx = \omega_x - x$, the derivative of ζ with respect to x is

$$\frac{\partial \zeta}{\partial x} = \frac{\partial}{\partial x}\left(\frac{-dz}{\sqrt{dx^2+dy^2}}\right) = \frac{1}{2}\frac{2dxdz}{\left(dx^2+dy^2\right)^{3/2}}(-1) = -\frac{dxdz}{\left(dx^2+dy^2\right)^{3/2}}. \tag{A.49}$$

Substituting Equations (A.48) and (A.49) into Equation (A.47) yields

$$\frac{\partial \varepsilon}{\partial x} = -\left(\frac{dx^2+dy^2}{D^2}\right)\frac{dxdz}{\left(dx^2+dy^2\right)^{3/2}} = -\frac{dxdz}{D^2\sqrt{dx^2+dy^2}}. \tag{A.50}$$

Letting $E_{\varepsilon_L} = e^{p_\varepsilon(\varepsilon_L - \varepsilon)}$ and $E_{\varepsilon_U} = e^{p_\varepsilon(\varepsilon - \varepsilon_U)}$, we substitute Equations (A.43) through (A.46), with Equation (A.50), into Equation (A.42) and obtain

$$\frac{\partial F_\varepsilon}{\partial x} = -\frac{p_\varepsilon dxdz}{(D^2)\sqrt{dx^2+dy^2}}\left[\frac{E_{\varepsilon_L}}{\left(1+E_{\varepsilon_L}\right)^2} - \frac{E_{\varepsilon_U}}{\left(1+E_{\varepsilon_U}\right)^2}\right]. \tag{A.51}$$

In a similar manner:

$$\frac{\partial F_\varepsilon}{\partial y} = \frac{\partial F_\varepsilon}{\partial E_L}\frac{\partial E_L}{\partial \varepsilon}\frac{\partial \varepsilon}{\partial y} + \frac{\partial F_\varepsilon}{\partial E_U}\frac{\partial E_U}{\partial \varepsilon}\frac{\partial \varepsilon}{\partial y} = \left(\frac{\partial F_\varepsilon}{\partial E_L}\frac{\partial E_L}{\partial \varepsilon} + \frac{\partial F_\varepsilon}{\partial E_U}\frac{\partial E_U}{\partial \varepsilon}\right)\frac{\partial \varepsilon}{\partial y}, \text{ and} \tag{A.52}$$

$$\frac{\partial \varepsilon}{\partial y} = \frac{\partial}{\partial y}\arctan\left(\frac{-dz}{\sqrt{dx^2+dy^2}}\right). \tag{A.53}$$

Once again,we let $\zeta = -dz/\sqrt{dx^2+dy^2}$ and compute the derivative of the inverse tangent function with respect to y as

$$\frac{\partial}{\partial y}\arctan(\zeta) = \left(\frac{1}{1+\zeta^2}\right)\frac{\partial \zeta}{\partial y} = \left(\frac{dx^2+dy^2}{dx^2+dy^2+dz^2}\right)\frac{\partial \zeta}{\partial y} = \left(\frac{dx^2+dy^2}{D^2}\right)\frac{\partial \zeta}{\partial y}. \tag{A.54}$$

Meanwhile, since $dy = \omega_y - y$, the derivative of ζ with respect to y is

$$\frac{\partial \zeta}{\partial y} = \frac{\partial}{\partial y}\left(\frac{-dz}{\sqrt{dx^2 + dy^2}}\right) = \frac{1}{2}\frac{2dydz}{\left(dx^2 + dy^2\right)^{3/2}}(-1) = -\frac{dydz}{\left(dx^2 + dy^2\right)^{3/2}}. \tag{A.55}$$

Substituting Equations (A.54) and (A.55) into Equation (A.53) yields

$$\frac{\partial \varepsilon}{\partial y} = -\left(\frac{dx^2 + dy^2}{D^2}\right)\frac{dydz}{\left(dx^2 + dy^2\right)^{3/2}} = -\frac{dydz}{(D^2)\ \sqrt{dx^2 + dy^2}}. \tag{A.56}$$

Using the same definitions for E_{ε_L} and E_{ε_L}, we substitute Equations (A.43) through (A.46), with Equation (A.56), into Equation (A.52) and obtain

$$\frac{\partial F_\varepsilon}{\partial y} = -\frac{p_\varepsilon dydz}{(D^2)\ \sqrt{dx^2 + dy^2}}\left[\frac{E_{\varepsilon_L}}{\left(1 + E_{\varepsilon_L}\right)^2} - \frac{E_{\varepsilon_U}}{\left(1 + E_{\varepsilon_U}\right)^2}\right]. \tag{A.57}$$

A.5 Gradients for Turn Rate Shaping Function $(\partial F_r / \partial \vec{x})$

Recall from Equation (2.20) that $F_r(\vec{x})$ depends only on the searcher vehicle's turn rate r. Therefore, the gradients with respect to all other state variables are zero, i.e., $\partial F_r/\partial x = \partial F_r/\partial y = F_r/\partial \psi = 0$. The derivative of F_r with respect to r is simply

$$\frac{\partial F_r}{\partial r} = \frac{\partial}{\partial r} e^{-\frac{1}{2}[r/\sigma_r]^2} = -\frac{r}{{\sigma_r}^2} e^{-\frac{1}{2}[r/\sigma_r]^2}. \tag{A.58}$$

A.6 Gradients for Instantaneous Detection Rate $(\partial\gamma/\partial\vec{x})$

We can now substitute the gradients derived in Sections A.2 through A.5 into the objective function gradients of Equation (A.2):

$$\frac{\partial\gamma}{\partial x} = \lambda\left(\frac{\partial p}{\partial x}F_\alpha F_\varepsilon F_r + p\frac{\partial F_\alpha}{\partial x}F_\varepsilon F_r + pF_\alpha\frac{\partial F_\varepsilon}{\partial x}F_r + pF_\alpha F_\varepsilon\cancelto{0}{\frac{\partial F_r}{\partial x}}\right),$$

$$\frac{\partial\gamma}{\partial y} = \lambda\left(\frac{\partial p}{\partial y}F_\alpha F_\varepsilon F_r + p\frac{\partial F_\alpha}{\partial y}F_\varepsilon F_r + pF_\alpha\frac{\partial F_\varepsilon}{\partial y}F_r + pF_\alpha F_\varepsilon\cancelto{0}{\frac{\partial F_r}{\partial y}}\right),$$

$$\frac{\partial\gamma}{\partial\psi} = \lambda\left(\cancelto{0}{\frac{\partial p}{\partial\psi}}F_\alpha F_\varepsilon F_r + p\frac{\partial F_\alpha}{\partial\psi}F_\varepsilon F_r + pF_\alpha\cancelto{0}{\frac{\partial F_\varepsilon}{\partial\psi}}F_r + pF_\alpha F_\varepsilon\cancelto{0}{\frac{\partial F_r}{\partial\psi}}\right), \text{ and}$$

$$\frac{\partial\gamma}{\partial r} = \lambda\left(\cancelto{0}{\frac{\partial p}{\partial r}}F_\alpha F_\varepsilon F_r + p\cancelto{0}{\frac{\partial F_\alpha}{\partial r}}F_\varepsilon F_r + pF_\alpha\cancelto{0}{\frac{\partial F_\varepsilon}{\partial r}}F_r + pF_\alpha F_\varepsilon\frac{\partial F_r}{\partial r}\right).$$

Thus, the gradients of the inner component of the objective function's running cost are

$$\frac{\partial\gamma}{\partial x} = \lambda\left(\frac{\partial p}{\partial x}F_\alpha F_\varepsilon F_r + p\frac{\partial F_\alpha}{\partial x}F_\varepsilon F_r + pF_\alpha\frac{\partial F_\varepsilon}{\partial x}F_r\right), \tag{A.59}$$

$$\frac{\partial\gamma}{\partial y} = \lambda\left(\frac{\partial p}{\partial y}F_\alpha F_\varepsilon F_r + p\frac{\partial F_\alpha}{\partial y}F_\varepsilon F_r + pF_\alpha\frac{\partial F_\varepsilon}{\partial y}F_r\right), \tag{A.60}$$

$$\frac{\partial\gamma}{\partial\psi} = \lambda\left(p\frac{\partial F_\alpha}{\partial\psi}F_\varepsilon F_r\right), \text{ and} \tag{A.61}$$

$$\frac{\partial\gamma}{\partial r} = \lambda\left(pF_\alpha F_\varepsilon\frac{\partial F_r}{\partial r}\right). \tag{A.62}$$

THIS PAGE INTENTIONALLY LEFT BLANK

APPENDIX B:
Hamming Cluster Batch Scripts

The Hamming supercomputer, a "hybrid cluster" of computing cores available via the NPS HPC Center [148] was used extensively during the course of this dissertation. Although our optimal control framework utilizes a sequential optimization algorithm that doesn't lend itself to massive parallelization, several simulations can be launched via the network to run on multiple computing cores simultaneously. This capability was a key enabler for conducting numerous trade studies at once, greatly accelerating the analysis process.

Hamming jobs are managed by Simple Linux Utility for Resource Management (SLURM), an open source "cluster management and job scheduling system" [150]. In order to use this resource effectively, a generalized MATLAB routine was developed to accept pertinent simulation parameters via SLURM environment variables. Next, batch scripts were created to execute this MATLAB routine on multiple computing nodes. These scripts leverage SLURM's job array mechanism, whereby each job consists of multiple computing tasks, each indexed by a taskID value. The batch scripts specify a range of values for the parameter of interest in a Monte Carlo simulation run, and convert these values into environment variables via the taskID. These environment variables are accessible by the MATLAB routine, regardless of the computing node it has been assigned to run on. A separate input argument determines the number of simulations to run for a given parameter configuration. Upon completion, SLURM sends an email notification with a listing of all generated output files. These files are then downloaded from Hamming via the network and subsequently analyzed in MATLAB.

B.1 SLURM Batch Files

B.1.1 Launch file-based simulations

```
#!/bin/bash
#
# Calling syntax is
#
#     sbatch --array=<indVar range>
#            -o $OUTFILE_PREFIX.o%A_%a -J
#            <8-char job name> multiUxVsonarFile.sbatch
#
# Request hamming resources...
#
#SBATCH --ntasks=1
#SBATCH --cpu-freq=high
#SBATCH --constraint=intel
#SBATCH --time=72:00:00
#SBATCH --mail-user=spkragel@nps.edu
#SBATCH --mail-type=END

export OMP_NUM_THREADS=1

echo "Args..."
echo outfilePrefix: ${OUTFILE_PREFIX}
echo Nv: ${SPOC_ARG_NV}
echo Tf: ${SPOC_ARG_TF}
echo Nt: ${SPOC_ARG_NT}
echo Nw: ${SPOC_ARG_NW}
echo Method: ${SPOC_ARG_METHOD}
echo DU: ${SPOC_ARG_DU}
echo TU: ${SPOC_ARG_TU}
echo UxVparams: ${SPOC_ARG_PARAMS}
echo SonarFile: ${SPOC_ARG_SONAR}
```

```
echo numSims: ${SPOC_ARG_N_SIMS}

if [[ -z "${SPOC_ARG_NV}" ]]; then
    SPOC_ARG_NV=${SLURM_ARRAY_TASK_ID}
    echo "Nv from task:" ${SPOC_ARG_NV}
elif [[ -z "${SPOC_ARG_NT}" ]]; then
    SPOC_ARG_NT=${SLURM_ARRAY_TASK_ID}
    echo "Nt from task:" ${SPOC_ARG_NT}
elif [[ -z "${SPOC_ARG_TF}" ]]; then
    SPOC_ARG_TF=
    $( echo "scale=0; ${SLURM_ARRAY_TASK_ID}*10" | bc)
    echo "Tf from task:" ${SPOC_ARG_TF}
else
    echo "All variables provided by user."
fi

if [[ -z "${SPOC_ARG_N_SIMS}" ]]; then
    SPOC_SPOC_ARG_TFARG_N_SIMS=1
fi
echo "Running" ${SPOC_ARG_N_SIMS} "MATLAB sims per task."

echo "Submitted as:" ${SLURM_JOB_NAME} "with ID:"
      ${SLURM_ARRAY_JOB_ID}"_"${SLURM_ARRAY_TASK_ID}

# Load MATLAB module
source /etc/profile
module load app/matlab
#
# cd to directory where job was submitted from
cd $SLURM_SUBMIT_DIR

# Run MATLAB
if [[ -n "${SPOC_ARG_TF}" ]]; then
```

```
    echo "Matlab script started on"
    date
    matlab -singleCompThread -nodesktop -nosplash -nojvm
    "cd ../GoodMultiRobotConstVelScaledMultiFLS; pwd;
         -r runHeadless(${SPOC_ARG_NV},${SPOC_ARG_TF},
                ${SPOC_ARG_NT}, ${SPOC_ARG_NW},
                '${SPOC_ARG_METHOD}',${SPOC_ARG_DU},
                ${SPOC_ARG_TU},'${SPOC_ARG_PARAMS}',
                '${SPOC_ARG_SONAR}',${SPOC_ARG_N_SIMS},
                '${OUTFILE_PREFIX}',${SLURM_ARRAY_JOB_ID},
                ${SLURM_ARRAY_TASK_ID}); quit"
    echo "Matlab script completed on"
    date
else
    echo "ERROR! runHeadless has missing argument(s)!"
fi
```

B.1.2 Launch parameter-based simulations

```
#!/bin/bash
#
# Calling syntax is
#     sbatch --array=<indVar range>
#            -o $OUTFILE_PREFIX.o%A_%a -J
#            <8-char job name> multiUxVsonar.sbatch
#
# Request hamming resources...
#
#SBATCH --ntasks=1
#SBATCH --cpu-freq=high
#SBATCH --constraint=intel
#SBATCH --time=12:00:00
#SBATCH --mail-user=spkragel@nps.edu
#SBATCH --mail-type=END

export OMP_NUM_THREADS=1

echo "Args..."
echo outfilePrefix: ${OUTFILE_PREFIX}
echo Nv: ${SPOC_ARG_NV}
echo Tf: ${SPOC_ARG_TF}
echo Nt: ${SPOC_ARG_NT}
echo Nw: ${SPOC_ARG_NW}
echo Method: ${SPOC_ARG_METHOD}
echo DU: ${SPOC_ARG_DU}
echo TU: ${SPOC_ARG_TU}
echo UxVparams: ${SPOC_ARG_PARAMS}
echo f: ${SPOC_ARG_FREQ}
echo FOM: ${SPOC_ARG_FOM}
echo Lamda: ${SPOC_ARG_LAMDA}
echo Sigma: ${SPOC_ARG_SIGMA}
```

```
echo Hfov: ${SPOC_ARG_HFOV}
echo Vfov: ${SPOC_ARG_VFOV}
echo Vde: ${SPOC_ARG_VDE}
echo numSims: ${SPOC_ARG_N_SIMS}

if [[ -z "${SPOC_ARG_FOM}" ]]; then
    SPOC_ARG_FOM=${SLURM_ARRAY_TASK_ID}
    echo "FOM from task:" ${SPOC_ARG_FOM}
elif [[ -z "${SPOC_ARG_LAMDA}" ]]; then
    SPOC_ARG_LAMDA=
    $( echo "scale=0; ${SLURM_ARRAY_TASK_ID}*10" | bc)
    echo "LAMDA from task:" ${SPOC_ARG_LAMDA}
elif [[ -z "${SPOC_ARG_HFOV}" ]]; then
    SPOC_ARG_HFOV=${SLURM_ARRAY_TASK_ID}
    echo "Hfov from task:" ${SPOC_ARG_HFOV}
elif [[ -z "${SPOC_ARG_VDE}" ]]; then
    SPOC_ARG_VDE=-${SLURM_ARRAY_TASK_ID}
    echo "Vde from task:" ${SPOC_ARG_VDE}
else
    echo "All variables provided by user."
fi

if [[ -z "${SPOC_ARG_N_SIMS}" ]]; then
    SPOC_ARG_N_SIMS=1
fi
echo "Running" ${SPOC_ARG_N_SIMS} "MATLAB sims per task."

echo "Submitted as:" ${SLURM_JOB_NAME} "with ID:"
     ${SLURM_ARRAY_JOB_ID}"_"${SLURM_ARRAY_TASK_ID}

# Load MATLAB module
source /etc/profile
module load app/matlab
```

```
#
# cd to directory where job was submitted from
cd $SLURM_SUBMIT_DIR

# Run MATLAB
if [[ -n "${SPOC_ARG_TF}" ]]; then
    echo "Matlab script started on"
    date
    matlab -singleCompThread -nodesktop -nosplash -nojvm
    "cd ../GoodMultiRobotConstVelScaledMultiFLS; pwd;
        -r runHeadless(${SPOC_ARG_NV},${SPOC_ARG_TF},
                ${SPOC_ARG_NT}, ${SPOC_ARG_NW},
                '${SPOC_ARG_METHOD}',${SPOC_ARG_DU},
                ${SPOC_ARG_TU},'${SPOC_ARG_PARAMS}',
                ${SPOC_ARG_FREQ},${SPOC_ARG_FOM},
                ${SPOC_ARG_LAMDA},${SPOC_ARG_SIGMA},
                ${SPOC_ARG_HFOV},${SPOC_ARG_VFOV},
                ${SPOC_ARG_VDE},${SPOC_ARG_N_SIMS},
                '${OUTFILE_PREFIX}',${SLURM_ARRAY_JOB_ID},
                ${SLURM_ARRAY_TASK_ID}); quit"
    echo "Matlab script completed on"
    date
else
    echo "ERROR! runHeadless has missing argument(s)!"
fi
```

B.2 SLURM Job Arrays

B.2.1 Mission Duration

```
#!/bin/bash
#
# Master script for passing variables into slurm
# batch scriptas environment variables
#
# Calling syntax is
#  launch_PvsTf.slurm <OUTFILE_PREFIX> <SonarFile> <N_SIMS>
#
#
export OUTFILE_PREFIX=$1

export SPOC_ARG_NV=1                # number of UxVs
export SPOC_ARG_TF=                 # final time [s]
export SPOC_ARG_NT=50               # time nodes
export SPOC_ARG_NW=25               # spatial nodes
export SPOC_ARG_METHOD="PEE"        # P)seudospectral or E)uler
export SPOC_ARG_DU=100              # dist canonical unit [m]
export SPOC_ARG_TU=100              # time canonical unit [s]
export SPOC_ARG_PARAMS="SeaFox" # file of dynamic params
export SPOC_ARG_SONAR=$2            # sonar params file
export SPOC_ARG_N_SIMS=$3           # number of sims to run

sbatch --array=90-366:12 --output=$OUTFILE_PREFIX.o%A_%a
       --job-name=TF$2 multiUxVsonarFile.sbatch
```

B.2.2 Time Discretization

```
#!/bin/bash
#
# Master script for passing variables into slurm
# batch script as environment variables
#
# Calling syntax is
#  launch_PvsNT.slurm <OUTFILE_PREFIX> <SonarFile> <N_SIMS>
#
#
export OUTFILE_PREFIX=$1

export SPOC_ARG_NV=1                # number of UxVs
export SPOC_ARG_TF=1800             # final time [s]
export SPOC_ARG_NT=                 # time nodes
export SPOC_ARG_NW=25               # spatial nodes
export SPOC_ARG_METHOD="PEE"        # P)seudospectral or E)uler
export SPOC_ARG_DU=100              # dist canonical unit [m]
export SPOC_ARG_TU=100              # time canonical unit [s]
export SPOC_ARG_PARAMS="REMUS"      # file of dynamic params
export SPOC_ARG_SONAR=$2            # sonar params file
export SPOC_ARG_N_SIMS=$3           # number of sims to run

sbatch --array=20-60:5 --output=$OUTFILE_PREFIX.o%A_%a
       --job-name=NT$2 multiUxVsonarFile.sbatch
```

B.2.3 Vertical Mounting Angle

```
#!/bin/bash
#
# Master script for passing variables into slurm
# batch script as environment variables
#
# Calling syntax is
#  launch_PvsVDE.slurm <OUTFILE_PREFIX> <F_KHZ> <N_SIMS>
#
#
export OUTFILE_PREFIX=$1

export SPOC_ARG_NV=1                # number of UxVs
export SPOC_ARG_TF=1800             # final time [s]
export SPOC_ARG_NT=50               # time nodes
export SPOC_ARG_NW=25               # spatial nodes
export SPOC_ARG_METHOD="PEE"        # P)seudospectral or E)uler
export SPOC_ARG_DU=100              # dist canonical unit [m]
export SPOC_ARG_TU=100              # time canonical unit [s]
export SPOC_ARG_PARAMS="REMUS"      # file of dynamic params
export SPOC_ARG_FREQ=$2             # sonar frequency [kHz]
export SPOC_ARG_FOM=66              # figure of merit [dB]
export SPOC_ARG_LAMDA=0.5           # Poisson rate [1/s]
export SPOC_ARG_SIGMA=9             # uncertainty [dB]
export SPOC_ARG_HFOV=90             # horizontal FOV [deg]
export SPOC_ARG_VFOV=10             # vertical FOV [deg]
export SPOC_ARG_VDE=                # sonar mount angle [deg]
export SPOC_ARG_N_SIMS=$3           # number of sims to run

sbatch --array=5-25:5 --output=$OUTFILE_PREFIX.o%A_%a
       --job-name=PvVDE$2 multiUxVsonar.sbatch
```

B.2.4 Figure of Merit

```
#!/bin/bash
#
# Master script for passing variables into slurm
# batch script as environment variables
#
# Calling syntax is
#  launch_PvsFOM.slurm <OUTFILE_PREFIX> <F_KHZ> <N_SIMS>
#
#
export OUTFILE_PREFIX=$1

export SPOC_ARG_NV=1                # number of UxVs
export SPOC_ARG_TF=1800             # final time [s]
export SPOC_ARG_NT=50               # time nodes
export SPOC_ARG_NW=25               # spatial nodes
export SPOC_ARG_METHOD="PEE"        # P)seudospectral or E)uler
export SPOC_ARG_DU=100              # dist canonical unit [m]
export SPOC_ARG_TU=100              # time canonical unit [s]
export SPOC_ARG_PARAMS="SeaFox" # file of dynamic params
export SPOC_ARG_FREQ=$2             # sonar frequency [kHz]
export SPOC_ARG_FOM                 # figure of merit [dB]
export SPOC_ARG_LAMDA=0.5           # Poisson rate [1/s]
export SPOC_ARG_SIGMA=9             # uncertainty [dB]
export SPOC_ARG_HFOV=90             # horizontal FOV [deg]
export SPOC_ARG_VFOV=10             # vertical FOV [deg]
export SPOC_ARG_VDE=-11             # sonar mount angle [deg]
export SPOC_ARG_N_SIMS=$3           # number of sims to run

sbatch --array=48-75:3 --output=$OUTFILE_PREFIX.o%A_%a
       --job-name=PvFOM$2 multiUxVsonar.sbatch
```

B.2.5 Poisson Scan Rate

```
#!/bin/bash
#
# Master script for passing variables into slurm
# batch script as environment variables
#
# Calling syntax is
#  launch_PvsLAM.slurm <OUTFILE_PREFIX> <F_KHZ> <N_SIMS>
#
#
export OUTFILE_PREFIX=$1

export SPOC_ARG_NV=1                # number of UxVs
export SPOC_ARG_TF=1800             # final time [s]
export SPOC_ARG_NT=50               # time nodes
export SPOC_ARG_NW=25               # spatial nodes
export SPOC_ARG_METHOD="PEE"        # P)seudospectral or E)uler
export SPOC_ARG_DU=100              # dist canonical unit [m]
export SPOC_ARG_TU=100              # time canonical unit [s]
export SPOC_ARG_PARAMS="SeaFox" # file of dynamic params
export SPOC_ARG_FREQ=$2             # sonar frequency [kHz]
export SPOC_ARG_FOM=66              # figure of merit [dB]
export SPOC_ARG_LAMDA               # Poisson rate [1/s]
export SPOC_ARG_SIGMA=9             # uncertainty [dB]
export SPOC_ARG_HFOV=90             # horizontal FOV [deg]
export SPOC_ARG_VFOV=10             # vertical FOV [deg]
export SPOC_ARG_VDE=-11             # sonar mount angle [deg]
export SPOC_ARG_N_SIMS=$3           # number of sims to run

sbatch --array=1-10 --output=$OUTFILE_PREFIX.o%A_%a
       --job-name=PvLAM$2 multiUxVsonar.sbatch
```

B.2.6 Horizontal Field of View

```
#!/bin/bash
#
# Master script for passing variables into slurm
# batch script as environment variables
#
# Calling syntax is
#  launch_PvsHFOV.slurm <OUTFILE_PREFIX> <F_KHZ> <N_SIMS>
#
#
export OUTFILE_PREFIX=$1

export SPOC_ARG_NV=1                # number of UxVs
export SPOC_ARG_TF=1800             # final time [s]
export SPOC_ARG_NT=50               # time nodes
export SPOC_ARG_NW=25               # spatial nodes
export SPOC_ARG_METHOD="PEE"        # P)seudospectral or E)uler
export SPOC_ARG_DU=100              # dist canonical unit [m]
export SPOC_ARG_TU=100              # time canonical unit [s]
export SPOC_ARG_PARAMS="SeaFox" # file of dynamic params
export SPOC_ARG_FREQ=$2             # sonar frequency [kHz]
export SPOC_ARG_FOM=66              # figure of merit [dB]
export SPOC_ARG_LAMDA=0.5           # Poisson rate [1/s]
export SPOC_ARG_SIGMA=9             # uncertainty [dB]
export SPOC_ARG_HFOV                # horizontal FOV [deg]
export SPOC_ARG_VFOV=10             # vertical FOV [deg]
export SPOC_ARG_VDE=-6              # sonar mount angle [deg]
export SPOC_ARG_N_SIMS=$3           # number of sims to run

sbatch --array=30-165:15 --output=$OUTFILE_PREFIX.o%A_%a
       --job-name=PvHFOV$2 multiUxVsonar.sbatch
```

B.2.7 Number of Searchers

```
#!/bin/bash
#
# Master script for passing variables into slurm
# batch script as environment variables
#
# Calling syntax is
#  launch_PvsNV.slurm <OUTFILE_PREFIX> <SonarFile> <N_SIMS>
#
#
export OUTFILE_PREFIX=$1

export SPOC_ARG_NV                  # number of UxVs
export SPOC_ARG_TF=1800             # final time [s]
export SPOC_ARG_NT=50               # time nodes
export SPOC_ARG_NW=25               # spatial nodes
export SPOC_ARG_METHOD="PPP"        # P)seudospectral or E)uler
export SPOC_ARG_DU=100              # dist canonical unit [m]
export SPOC_ARG_TU=100              # time canonical unit [s]
export SPOC_ARG_PARAMS="SeaFox" # file of dynamic params
export SPOC_ARG_SONAR=$2            # sonar params file
export SPOC_ARG_N_SIMS=$3           # number of sims to run

sbatch --array=1-5 --output=$OUTFILE_PREFIX.o%A_%a
       --job-name=NV$2 multiUxVsonarFile.sbatch
```

B.2.8 Type of Searchers

```
#!/bin/bash
#
# Master script for passing variables into slurm
# batch script as environment variables
#
# Calling syntax is
#  launch_PvsNV.slurm <NV> <UxvTeamStr> <SonarTeamStr>
#                     <N_SIMS> <OutFilePrefix>
#
#
export OUTFILE_PREFIX=$5

export SPOC_ARG_NV=$1              # number of UxVs
export SPOC_ARG_TF=1800            # final time [s]
export SPOC_ARG_NT=                # time nodes
export SPOC_ARG_NW=25              # spatial nodes
export SPOC_ARG_METHOD="PEE"       # P)seudospectral or E)uler
export SPOC_ARG_DU=100             # dist canonical unit [m]
export SPOC_ARG_TU=100             # time canonical unit [s]
export SPOC_ARG_PARAMS=$2          # file of dynamic params
export SPOC_ARG_SONAR=$3           # sonar params file
export SPOC_ARG_N_SIMS=$4          # number of sims to run

sbatch --array=10-45:5 --output=$OUTFILE_PREFIX.o%A_%a
       --job-name=$2$3 multiUxVsonarFile.sbatch
```

B.3 MATLAB Run Script

```
function Results = runHeadless(varargin)
%% New 11/18/16 for Heterogeneous Teams
% 7 mandatory inputs:
%   Nv: number of UxVs
%   (ex: 'SRR' for 3-vehicle team with 1 SeaFox and 2 REMUS)
%   Tf: final mission time [seconds]
%   Nt: number of time nodes
%   Nw: number of parameter nodes
%   MethodString: 3 chars for TSS,
%                 either P for PS, E for Euler (ex: PEE)
%   DU: distance canonical unit [in meters]
%   TU: time canonical unit [in seconds]
%
%   vehicle params
%   EITHER:
%       Veh: characters denoting team composition,
%            S for SeaFox, R for Remus
%   OR: (need all 3; these are applied to all Nv vehicles)
%       V: constant velocity [m/s]
%       T: Nomoto T [s]
%       K: Nomoto K [1/s]
%
%   sonar params
%   EITHER:
%       Son: characters denoting sonar model
%       (ex: '249' for 200kHz on UxV#1,
%             450kHz on UxV#2, 900kHz on UxV#3)
%   OR: (need all 7; these are applied to all Nv vehicles)
%       f:   design frequency [kHz]
%       FOM: figure of merit [dB]
%       LAMDA: Poisson rate [1/s]
%       SIGMA: cum. detection uncertainty [dB]
```

```
%       HFOV: horizontal field of view [degrees]
%       VFOV: vertical field of view [degrees]
%       VDE: vertical mounting angle [degrees]
%            (negative is down)
%
%   Nsims: number of simulations
%   <outfile prefix>: prepends results file name
%   jobID: the slurm array job ID
%   taskID: the slurm array element ID
%
%
% This launches multiple SPOC simulations.
% SPOC, by CLAIRE WALTON (2013). Some Rights Reserved.
%=========================================================
...
for s=1:Nsims

    disp(['*** Running Simulation ', num2str(s), '/', ...
                num2str(numSims), ' ***']);

    CONSTANTS.cpuInfo = cpuinfo;
    CONSTANTS.Start.Time = now;
    CONSTANTS.Start.Date = datestr(CONSTANTS.Start.Time);

    Results = SPOC(gMultiCvScaledMultiFLS,...
                    Discretization, Methods)

    CONSTANTS.Stop.Time = now;
    CONSTANTS.Stop.Date = datestr(CONSTANTS.Stop.Time);
...
    save(filename, 'Results');
    disp(['Results file is: ' filename]);
end;
```

THIS PAGE INTENTIONALLY LEFT BLANK

List of References

[1] I. M. Ross, *A Primer on Pontryagin's Principle in Optimal Control*. Collegiate Publishers, 2009.

[2] I. M. Ross, "Astrodynamic Optimization," class notes for AE4850, Dept. of Mech. and Aero. Eng., Naval Postgraduate School, Monterey, CA, fall 2010.

[3] Q. Gong, W. Kang, and I. M. Ross, "A pseudospectral method for the optimal control of constrained feedback linearizable systems," *IEEE Transactions on Automatic Control*, vol. 51, no. 7, pp. 1115–1129, July 2006.

[4] I. M. Ross and M. Karpenko, "A review of pseudospectral optimal control: From theory to flight," *Annual Reviews in Control*, vol. 36, no. 2, Dec. 2012.

[5] C. Phelps, Q. Gong, J. O. Royset, C. Walton, and I. Kaminer, "Consistent approximation of a nonlinear optimal control problem with uncertain parameters," *Automatica*, vol. 50, no. 12, pp. 2987–2997, Dec. 2014.

[6] J. Foraker, J. O. Royset, and I. Kaminer, "Search-trajectory optimization: Part I, formulation and theory," *Journal of Optimization Theory and Applications*, vol. 169, no. 2, pp. 530–549, June 2015.

[7] J. Foraker, J. O. Royset, and I. Kaminer, "Search-trajectory optimization: Part II, algorithms and computations," *Journal of Optimization Theory and Applications*, vol. 169, no. 2, pp. 550–567, June 2015.

[8] I. M. Ross, M. Karpenko, and R. J. Proulx, "A Lebesgue-Stieltjes framework for optimal control and allocation," in *2015 American Control Conference (ACC)*, 2015, pp. 5599–5604.

[9] I. M. Ross, M. Karpenko, and R. J. Proulx, "Path constraints in tychastic and unscented optimal control: Theory, application and experimental results," in *2016 American Control Conference (ACC)*, 2016, pp. 2918–2923.

[10] C. Walton, C. Phelps, Q. Gong, and I. Kaminer, "A numerical algorithm for optimal control of systems with parameter uncertainty," in *10th IFAC Symposium on Nonlinear Control Systems (NOLCOS)*, Monterey, CA, 2016.

[11] C. L. Walton, Q. Gong, I. Kaminer, and J. O. Royset, "Optimal motion planning for searching for uncertain targets," *IFAC Proceedings Volumes*, vol. 47, no. 3, pp. 8977–8982, 2014.

[12] E. Pinto, F. Marques, R. Mendonça, A. Lourenço, P. Santana, and J. Barata, "An autonomous surface-aerial marsupial robotic team for riverine environmental monitoring: Benefiting from coordinated aerial, underwater, and surface level perception," in *2014 IEEE International Conference on Robotics and Biomimetics (ROBIO 2014)*, 2014, pp. 443–450.

[13] D. Sternlicht, J. Fernandez, R. Holtzapple, D. Kucik, T. Montgomery, and C. Loeffler, "Advanced sonar technologies for autonomous mine countermeasures," in *OCEANS'11 MTS/IEEE KONA*, 2011, pp. 1–5.

[14] J. Keller. (2013, Jun. 2). Raytheon, Applied Physical Sciences to develop Navy unmanned mine-hunting technology. *Military & Aerospace Electronics*. [Online]. Available: http://www.militaryaerospace.com/articles/2013/06/mine-hunting-USV.html

[15] USV payloads for single sortie detect to engage (SS-DTE) mine counter measures. [Online]. Available: http://www.onr.navy.mil/~/media/Files/Funding-Announcements/BAA/2012/12-018.ashx. Accessed Nov. 29, 2016.

[16] M. Bays, "Recent advances in mine countermeasure and mine warfare autonomy at NSWC PCD," presented at May 2014 CRUSER monthly meeting, Naval Postgraduate School, Monterey, CA, May 2014. Available: https://my.nps.edu/documents/105302057/105304198/2014_05_Bays.pdf/67755b75-3b72-4992-9563-ea070bfac4c1

[17] V. Djapic and D. Nad, "Using collaborative autonomous vehicles in mine countermeasures," in *OCEANS 2010 IEEE - Sydney*, 2010, pp. 1–7.

[18] D. Nad, N. Miskovic, V. Djapic, and Z. Vukic, "Sonar aided navigation and control of small UUVs," in *2011 19th Mediterranean Conference on Control Automation (MED)*, 2011, pp. 418–423.

[19] H. Choset and J. Burdick, "Sensor based motion planning: The hierarchical generalized Voronoi graph," in *Workshop on Algorithmic Foundations of Robotics*, 1996.

[20] C. Cai and S. Ferrari, "Information-driven sensor path planning by approximate cell decomposition," *IEEE Transactions on Systems, Man, and Cybernetics, Part B (Cybernetics)*, vol. 39, no. 3, pp. 672–689, 2013.

[21] L. Paull, S. Saeedi, H. Li, and V. Myers, "An information gain based adaptive path planning method for an autonomous underwater vehicle using sidescan sonar," in *2010 IEEE International Conference on Automation Science and Engineering*, 2010, pp. 835–840.

[22] L. Paull, S. Saeedi, M. Seto, and H. Li, "Sensor-driven online coverage planning for autonomous underwater vehicles," *IEEE/ASME Transactions on Mechatronics*, vol. 18, no. 6, pp. 1827–1838, Dec. 2013.

[23] A. Washburn and M. Kress, *Combat Modeling* (International Series in Operations Research & Management Science 134). Boston, MA: Springer, 2009.

[24] Program Executive Office, Littoral and Mine Warfare, Expeditionary Warfare Directorate, *21st century U.S. Navy mine warfare : Ensuring global access and commerce*. Washington, DC: U.S. Navy, 2009.

[25] J. Bachkosky, T. Brancati, D. Conley, J. Douglass, P. Gale, D. Held, L. Hettche, J. Luyten, I. Peden, R. Rumpf, A. Salkind, J. Sinnett, and G. Whistler, Jr., "Unmanned vehicles (uv) in mine countermeasures," Naval Research Advisory Committee, Arlington, VA, Tech. Rep. NRAC-2000-03, 2000. Available: http://www.nrac.navy.mil/docs/2000_rpt_unmanned_vehicles_mine_countermeasures.pdf

[26] N. Abreu and A. Matos, "Minehunting mission planning for autonomous underwater systems using evolutionary algorithms," *Unmanned Systems*, vol. 02, no. 04, pp. 323–349, Oct. 2014.

[27] B. Nguyen, D. Hopkin, and H. Yip, "Autonomous underwater vehicles: A transformation in mine counter-measure operations," *Defense & Security Analysis*, vol. 24, no. 3, pp. 247–266, Sep. 2008.

[28] M. J. Bays, "Stochastic motion planning for applications in sbsea survey and area protection," Ph.D. dissertation, Dept. Mech. Eng., Virginia Polytechnic Institute and State University, 2012.

[29] J. C. Hyland and C. M. Smith, "Automated area segmentation for ocean bottom surveys," in *Proc. SPIE 9454, Detection and Sensing of Mines, Explosive Objects, and Obscured Targets*, 2015, vol. 9454.

[30] M. J. Bays, A. Shende, D. J. Stilwell, and S. A. Redfield, "Theory and experimental results for the multiple aspect coverage problem," *Ocean Engineering*, vol. 54, pp. 51–60, Nov. 2012.

[31] B. Nguyen, M. J. Bays, A. Shende, and D. J. Stilwell, "An approach to subsea survey for safe naval transit," in *OCEANS'11 MTS/IEEE KONA*, 2011, pp. 1–6.

[32] H. Johannsson, T. Thorhallsson, and H. Hafsteinsson, "An efficient method of combining detection and identification of seafloor objects using Gavia AUV," in *OCEANS 2006*, 2006, pp. 1–6.

[33] S. Sariel, T. Balch, and N. Erdogan, "Naval Mine Countermeasure Missions," *IEEE Robotics Automation Magazine*, vol. 15, no. 1, pp. 45–52, Mar. 2008.

[34] M. J. Bays, R. D. Tatum, L. Cofer, and J. R. Perkins, "Automated scheduling and mission visualization for mine countermeasure operations," in *OCEANS 2015 - MTS/IEEE Washington*, Washington DC, 2015.

[35] A. Shafer, M. Benjamin, J. Leonard, and J. Curcio, "Autonomous cooperation of heterogeneous platforms for sea-based search tasks," in *OCEANS 2008*, 2008, pp. 1–10.

[36] B. O. Koopman, *Search and Screening*. Washington, DC: Operations Evaluation Group, Office of the Chief of Naval Operations, Navy Dept., 1946.

[37] B. O. Koopman, *Search and Screening : General Principles with Historical Applications*. Elmsford, NY: Pergamon Press, 1980.

[38] *U.S. Coast Guard Addendum to the United States National Search and Rescue Supplement (NSS) to the International Aeronautical and Maritime Search and Rescue Manual (IAMSAR)*, COMDTINST M16130.2F, U.S. Department of Homeland Security, United States Coast Guard, Washington, DC, Jan. 2013. Available: https://www.uscg.mil/hq/cg5/cg534/manuals/COMDTINSTM16130.2F.pdf

[39] J. Frost, "The theory of search: A simplified explanation," Soza & Company, Ltd. and Office of Search and Rescue, U.S. Coast Guard, Fairfax, VA, Tech. Rep., 1998. Available: http://www.navcen.uscg.gov/pdf/Theory_of_Search.pdf

[40] L. D. Stone, *Theory of Optimal Search*, 2nd ed. Arlington, Va: Military Applications Section, Operations Research Society of America, 1989.

[41] L. D. Stone, "Brief overview of search theory and applications," in *Search Theory and Applications* (NATO Conference Series 8), K. B. Haley and L. D. Stone, Eds. New York, NY: Plenum Press, 1980, pp. 1–7.

[42] L. D. Stone, "Search theory: A mathematical theory for finding lost objects," *Mathematics Magazine*, vol. 50, no. 5, pp. 248–256, Nov. 1977.

[43] L. D. Stone and J. A. Stanshine, "Optimal Search Using Uninterrupted Contact Investigation," *SIAM Journal on Applied Mathematics*, vol. 20, no. 2, pp. 241–263, Mar. 1971.

[44] M. Kress, K. Y. Lin, and R. Szechtman, "Optimal discrete search with imperfect specificity," *Mathematical Methods of Operations Research*, vol. 68, no. 3, pp. 539–549, Dec. 2008.

[45] S. J. Benkoski, M. G. Monticino, and J. R. Weisinger, "A survey of the search theory literature," *Naval Research Logistics (NRL)*, vol. 38, no. 4, pp. 469–494, Aug. 1991.

[46] T. H. Chung, G. A. Hollinger, and V. Isler, "Search and pursuit-evasion in mobile robotics," *Autonomous Robots*, vol. 31, no. 4, pp. 299–316, July 2011.

[47] L. D. Stone, J. O. Royset, and A. R. Washburn, *Optimal Search for Moving Targets* (International Series in Operations Research & Management Science 237). New York, NY: Springer, 2016.

[48] G. A. Hollinger, S. Yerramalli, S. Singh, U. Mitra, and G. S. Sukhatme, "Distributed coordination and data fusion for underwater search," in *Proceedings 2011 IEEE International Conference on Robotics and Automation (ICRA)*, 2011, pp. 349–355.

[49] G. A. Hollinger, S. Yerramalli, S. Singh, U. Mitra, and G. S. Sukhatme, "Distributed Data Fusion for Multirobot Search," *IEEE Transactions on Robotics*, vol. 31, no. 1, pp. 55–66, Feb. 2015.

[50] J. G. Baylog and T. A. Wettergren, "Multiple pass collaborative search in the presence of false alarms," in *Proc. SPIE 9454, Detection and Sensing of Mines, Explosive Objects, and Obscured Targets XX, 94541G*, 2015, vol. 9454.

[51] A. R. Washburn, *Search and Detection*, 4th ed. Linthicum, MD: Institute for Operations Research and the Management Sciences, 2002.

[52] R. E. Hansen, "Introduction to sonar," course materiel to INF-GEO4310, Dept. of Informatics, University of Oslo, Oslo, Norway, fall 2012. Available: http://www.uio.no/studier/emner/matnat/ifi/INF-GEO4310/h09/undervisningsmateriale/sonar_introduction_2009.pdf

[53] R. J. Urick, *Principles of Underwater Sound*, 3rd ed. Los Altos, CA: Peninsula Publishing, 1996.

[54] A. D. Waite, *Sonar for Practising Engineers*, 3rd ed. Chichester, UK: Wiley, 2002.

[55] M. Ainslie, *Principles of Sonar Performance Modelling*. Berlin, Germany: Springer, 2010.

[56] P. Etter, *Underwater Acoustic Modeling and Simulation*, 4th ed. Boca Raton, FL: Taylor & Francis, 2013.

[57] P. C. Chu, C. Cintron, S. D. Haeger, and R. E. Keenan, "Acoustic mine detection using the Navy's CASS/GRAB model," in *Journal of Counter-Ordnance Technology (Fifth International Symposium on Technology and Mine Problem)*, Monterey, CA, 2002. Available: http://www.dtic.mil/cgi-bin/GetTRDoc?Location=U2&doc=GetTRDoc.pdf&AD=ADA478751

[58] P. C. Chu, N. A. Vares, and R. E. Keenan, "Uncertainty in acoustic mine detection due to environmental variability," in *Journal of Counter-Ordnance Technology (Sixth International Symposium on Technology and Mine Problem)*, Monterey, CA, 2004. Available: http://www.dtic.mil/cgi-bin/GetTRDoc?Location=U2&doc=GetTRDoc.pdf&AD=ADA482282

[59] A. Percival and M. Stoddard, "PATHA: A Planning Aid for Tasking Heterogeneous Assets for route survey or mine countermeasures operations," in *OCEANS 2010 MTS/IEEE SEATTLE*, 2010, pp. 1–8.

[60] D. Folds and N. Anderson, "High resolution sonar simulation techniques," in *Acoustics, Speech, and Signal Processing, IEEE International Conference on ICASSP '77.*, 1977, vol. 2, pp. 840–844.

[61] K. J. DeMarco, M. E. West, and A. M. Howard, "A computationally-efficient 2D imaging sonar model for underwater robotics simulations in Gazebo," in *OCEANS 2015 - MTS/IEEE Washington*, 2015, pp. 1–7.

[62] H. Saç, K. LeblebicioğLu, and G. BozdağI Akar, "2D high-frequency forward-looking sonar simulator based on continuous surfaces approach," *Turkish Journal of Electrical Engineering & Computer Sciences*, vol. 23, no. Sup.1, pp. 2289–2303, 2015. Available: http://journals.tubitak.gov.tr/elektrik/issues/elk-15-23-sup.1/elk-23-sup.1-21-1305-188.pdf

[63] H. Choset, "Coverage for robotics – A survey of recent results," *Annals of Mathematics and Artificial Intelligence*, vol. 31, no. 1, pp. 113–126, Oct. 2001.

[64] H. Choset and P. Pignon, "Coverage path planning: The boustrophedon decomposition," in *International Conference on Field and Service Robotics*, 1997.

[65] D. T. Latimer, S. Srinivasa, V. L. Shue, S. Sonne, H. Choset, and A. Hurst, "Towards sensor based coverage with robot teams," in *Proceedings 2002 IEEE International Conference on Robotics and Automation (ICRA)*, 2002, vol. 1, pp. 961–967.

[66] W. H. Huang, "Optimal line-sweep-based decompositions for coverage algorithms," in *Proceedings 2001 IEEE International Conference on Robotics and Automation (ICRA)*, 2001, vol. 1, pp. 27–32.

[67] E. Galceran, R. Campos, N. Palomeras, D. Ribas, M. Carreras, and P. Ridao, "Coverage path planning with real-time replanning and surface reconstruction for inspection of three-dimensional underwater structures using autonomous underwater vehicles," *Journal of Field Robotics*, vol. 32, no. 7, pp. 952–983, Nov. 2015.

[68] E. Galceran and M. Carreras, "Planning coverage paths on bathymetric maps for in-detail inspection of the ocean floor," in *Proceedings 2013 IEEE International Conference on Robotics and Automation (ICRA)*, 2013, pp. 4159–4164.

[69] D. P. Williams, "On optimal AUV track-spacing for underwater mine detection," in *Proceedings 2010 IEEE International Conference on Robotics and Automation (ICRA)*, 2010, pp. 4755–4762.

[70] H. Yetkin, C. Lutz, and D. Stilwell, "Utility-based adaptive path planning for subsea search," in *OCEANS 2015 - MTS/IEEE Washington*, 2015.

[71] E. U. Acar, H. Choset, Y. Zhang, and M. Schervish, "Path planning for robotic demining: Robust sensor-based coverage of unstructured environments and probabilistic methods," *The International Journal of Robotics Research*, vol. 22, no. 7-8, pp. 441–466, July 2003.

[72] A. J. Healey and J. Kim, "Bugs: Robot control, UXO and minefield clearance," Mechanical Engineering Department, Naval Postgraduate School, Monterey, CA, Tech. Rep. NPS-ME-96-005, Dec. 1996. Available: http://calhoun.nps.edu/bitstream/handle/10945/24446/NPS-ME-96-005.pdf?sequence=1&isAllowed=y

[73] S. M. LaValle, *Planning Algorithms*. New York, NY: Cambridge University Press, 2006.

[74] M. A. Hurni, "An information-centric approach to autonomous trajectory planning utilizing optimal control techniques," Ph.D. dissertation, Dept. of Mech. and Aero. Eng., Naval Postgraduate School, Monterey, CA, 2009.

[75] I. M. Ross and F. Fahroo, *Legendre pseudospectral approximations of optimal control problems* (Lecture Notes in Control and Information Sciences 295). Berlin, Germany: Springer, 2003, pp. 327–342.

[76] I. M. Ross, "A roadmap for optimal control: The right way to commute," *Annals of the New York Academy of Sciences*, vol. 1065, no. 1, pp. 210–231, Dec. 2005.

[77] Q. Gong, I. M. Ross, W. Kang, and F. Fahroo, "Connections between the covector mapping theorem and convergence of pseudospectral methods for optimal control," *Computational Optimization and Applications*, vol. 41, no. 3, pp. 307–335, Dec. 2008.

[78] J. C. Foraker, "Optimal search for moving targets in continuous time and space using consistent approximations," Ph.D. dissertation, Dept. Ops. Research, Naval Postgraduate School, Monterey, CA, 2011.

[79] C. L. Walton, "The design and implementation of motion planning problems given parameter uncertainty," Ph.D. dissertation, Dept. Appl. Math. & Stat., University of California, Santa Cruz, CA, 2015.

[80] I. M. Ross, R. J. Proulx, M. Karpenko, and Q. Gong, "Riemann–Stieltjes optimal control problems for uncertain dynamic systems," *Journal of Guidance, Control, and Dynamics*, vol. 38, no. 7, pp. 1251–1263, 2015.

[81] C. Phelps, Q. Gong, J. Royset, and I. Kaminer, "Consistent approximation of an optimal search problem," in *Proceedings 2012 IEEE Conference on Decision and Control (CDC)*, 2012, pp. 630–637.

[82] R. Stokey, T. Austin, B. Allen, N. Forrester, E. Gifford, R. Goldsborough, G. Packard, M. Purcell, and C. von Alt, "Very shallow water mine countermeasures using the REMUS AUV: A practical approach yielding accurate results," in *OCEANS 2001 MTS/IEEE Conference and Exhibition*, 2001, vol. 1, pp. 149–156.

[83] B. O. Koopman, "The theory of search – II. Target detection," *Operations Research*, vol. 4, no. 5, pp. 503–531, Oct. 1956.

[84] D. H. Wagner, W. C. Mylander, and T. J. Sanders, Eds., *Naval Operations Analysis*, 3rd ed. Annapolis, MD: Naval Institute Press, 1999.

[85] REMUS 100 for defense applications. (n.d.). [Online]. Available: http://www.hydroid.com/remus-100-defense. Accessed Nov. 29, 2016.

[86] K. M. Kim, S. H. Lee, and J. N. Eagle, "Approximating the poisson scan and $(\lambda - \sigma)$ acoustic detection model with a random search formula," in *Proceedings 40th International Conference on Computers and Industrial Engineering (CIE)*, 2010, pp. 1–7.

[87] R. E. Keenan, "An introduction to GRAB eigenrays and CASS reverberation and signal excess," in *OCEANS 2000 MTS/IEEE Conference and Exhibition*, 2000, vol. 2, pp. 1065–1070.

[88] H. Weinberg, R. Deavenport, E. McCarthy, and C. Anderson, "Comprehensive Acoustic System Simulation (CASS) reference guide," NUWC, Tech. Rep. NUWC-NPT TM 01-016, Mar. 2001.

[89] S. B. Dasinger, B. I. Incze, and T. A. Holz, "A concept for efficient signal excess calculation for multistatic operations analysis," in *OCEANS 2006 – Asia Pacific*, 2006, pp. 1–6.

[90] E. Tucholski. Underwater acoustics and sonar. Dept. of Physics, United States Naval Academy. Annapolis, MD. handouts for SP411. Available: https://www.usna.edu/Users/physics/ejtuchol/teaching/SP411.php. Accessed Nov. 29, 2016.

[91] PSeries 2D imaging sonar. (n.d.). [Online]. Available: http://www.blueview.com/products/2d-imaging-sonar/pseries-archives/. Accessed Nov. 29, 2016.

[92] Sea Scan SSPC AUV system. (n.d.). [Online]. Available: http://www.marinesonic.com/products/seascanSSPCAUV.html. Accessed Nov. 29, 2016.

[93] EdgeTech Customer & Technical Support Resource Center. (n.d.). [Online]. Available: http://www.edgetech.com/underwater-technology-support/#resource-center. Accessed Nov. 29, 2016.

[94] Hansen, Roy Edgar, "Introduction to synthetic aperture sonar," in *Sonar Systems*, N. Kolev, Ed. Rijeka, Croatia: InTech, 2011. Available: http://www.intechopen.com/books/sonar-systems/introduction-to-synthetic-aperture-sonar

[95] Logistic function. (n.d.). *Wikipedia*. [Online]. Available: https://en.wikipedia.org/w/index.php?title=Logistic_function&oldid=744524090. Accessed Nov. 29, 2016.

[96] E. W. Weisstein. Sigmoid Function. From *MathWorld*–A Wolfram Web Resource. [Online]. Available: http://mathworld.wolfram.com/SigmoidFunction.html. Accessed Nov. 29, 2016.

[97] P. Blondel, *The Handbook of Sidescan Sonar*. Berlin, Germany: Springer, 2009.

[98] S. D. Anstee, "The effects of towfish motion on sidescan sonar images," DSTO Materials Research Laboratory, Victoria, Australia, Tech. Rep. MRL-RR-1-94, 1994. Available: http://digext6.defence.gov.au/dspace/handle/1947/9915

[99] P. E. Gill, W. Murray, and M. A. Saunders, *User's guide for SNOPT version 6: A Fortran package for large-scale nonlinear programming*, University of California, San Diego and Stanford University, 2002. Available: http://www.cam.ucsd.edu/~peg/papers/sndoc6.pdf

[100] C. Loeffler. (n.d.). Sonar and AUV technology. Office of Ocean Exploration and Research, National Oceanic and Atmospheric Administration. [Online]. Available: http://oceanexplorer.noaa.gov/explorations/10thunderbay/background/sonar/sonar.html. Accessed Nov. 29, 2016.

[101] L. Moreavek and T. Brudner, "USS Asheville leads the way in high frequency sonar," *Undersea Warfare*, vol. 1, no. 3, 1999. Available: http://www.public.navy.mil/subfor/underseawarfaremagazine/Issues/Archives/issue_03/uss_asheville.htm

[102] R. L. Thompson, J. Seawall, and T. Josserand, "Two dimensional and three dimensional imaging results using blazed arrays," in *OCEANS 2001 MTS/IEEE Conference and Exhibition*, 2001, vol. 2, pp. 985–988.

[103] N. A. McChesney, "Three-dimensional feature reconstruction with dual forward looking sonars for unmanned underwater vehicle navigation," Master's thesis, Dept. of Elect. Eng., Naval Postgraduate School, Monterey, CA, 2009.

[104] *Multibeam Sonar Theory of Operation*, L3 Communications SeaBeam Instruments, East Walpole, MA, 2000. Available: https://www.ldeo.columbia.edu/res/pi/MB-System/sonarfunction/SeaBeamMultibeamTheoryOperation.pdf

[105] S. T. Bachelor, R. L. Thompson, and J. Seawall, "Systems and methods implementing frequency-steered acoustic arrays for 2D and 3D imaging," U.S. Patent 7 606 114, Oct. 20, 2009. Available: http://patft.uspto.gov/netacgi/nph-Parser?Sect1=PTO2&Sect2=HITOFF&p=1&u=%2Fnetahtml%2FPTO%2Fsearch-bool.html&r=5&f=G&l=50&co1=AND&d=PTXT&s1=7606114&OS=7606114&RS=7606114

[106] C. Jones, "Teledyne blueview p-series sonar maximum source level analysis - white paper," Teledyne BlueView, Tech. Rep., Nov. 2012. Available: http://www.blueview.com/assets/Uploads/Support-Document-Library/P-Series-Max-Source-Level-Analysis-White-Paper-Teledyne-BlueView.pdf

[107] T. E. Wilcox and B. Fletcher, "High frequency side scan sonar for target reacquisition and identification," in *OCEANS 2003 MTS/IEEE Conference and Exhibition*, 2003, vol. 4, pp. 1882–1887.

[108] D. Sternlicht, J. Fernandez, J. Prater, J. Weaver, J. Isaccs, T. Montgomery, C. Loeffler, and M. Purcell, "Advanced sonar technologies for high clearance rate mine countermeasures," in *OCEANS 2016 - MTS/IEEE Monterey*, 2016, pp. 1–5.

[109] Little USV, big applications. (2004, Apr.). *MarineLink*. [Online]. Available: http://www.marinelink.com/news/applications-little-big323082

[110] D. Richman. (2008, Nov. 12). Seattle firm builds boats with a mission: Navy and Coast Guard use remote-controlled Sea Fox. *Seattle Post-Intelligencer*. Seattle, WA. [Online]. Available: http://www.seattlepi.com/business/article/Seattle-company-builds-boats-with-a-mission-1291322.php

[111] A. Gadre, S. Kragelund, T. Masek, D. Stilwell, C. Woolsey, and D. Horner, "Subsurface and surface sensing for autonomous navigation in a riverine environment," in *Proceedings Association of Unmanned Vehicle Systems International (AUVSI) Unmanned Systems North America Convention*, 2009, vol. 2, pp. 1192–1208.

[112] O. A. Yakimenko and S. P. Kragelund, "Real-time optimal guidance and obstacle avoidance for UMVs," in *Autonomous Underwater Vehicles*, N. A. Cruz, Ed. Rijeka, Croatia: InTech, 2011. Available: http://www.intechopen.com/books/autonomous-underwater-vehicles/real-time-optimal-guidance-and-obstacle-avoidance-for-umvs

[113] S. Kragelund, V. Dobrokhodov, A. Monarrez, M. Hurban, and C. Khol, "Adaptive speed control for autonomous surface vessels," in *OCEANS 2013 - MTS/IEEE San Diego*, 2013, pp. 1–10.

[114] S. Terjesen, "Navigation system design and state estimation for a small rigid hull inflatable boat (RHIB)," Master's thesis, Dept. of Mech. and Aero. Eng., Naval Postgraduate School, Monterey, CA, 2014.

[115] T. I. Fossen, *Marine Control Systems Guidance, Navigation, and Control of Ships, Rigs and Underwater Vehicles*. Trondheim, Norway: Marine Cybernetics, 2002.

[116] L. Moreira, T. I. Fossen, and C. G. Soares, "Modeling, Guidance and Control of *Esso Osaka* Model," *IFAC Proceedings Volumes*, vol. 38, no. 1, pp. 85–90, 2005.

[117] J. Journee, "A Simple Method for Determining the Manoeuvring Indices K and T from Zigzag Trial Data," Delft University of Technology, Ship Hydromechanics Laboratory, Delft, Tech. Rep. 267, June 1970. Available: http://shipmotions.nl/DUT/PapersReports/

[118] D. Clarke, "The foundations of steering and maneuvering," in *Proceedings of Sixth Conference on Maneuvering and Control of Marine Crafts (MCMC 2003), Girona, Spain*, 2003, pp. 2–16.

[119] C. Sonnenburg, A. Gadre, D. Horner, S. Kragelund, A. Marcus, D. J. Stilwell, and C. A. Woolsey, "Control-oriented planar motion modeling of unmanned surface vehicles," Virginia Center for Autonomous Systems, Tech. Rep. VACAS-2010-01, 2010. Available: http://www.unmanned.vt.edu/discovery/reports/VaCAS_2010_01.pdf

[120] C. von Alt, B. Allen, T. Austin, and R. Stokey, "Remote environmental measuring units," in *Proceedings of the 1994 Symposium on Autonomous Underwater Vehicle Technology*, 1994, pp. 13–19.

[121] C. von Alt, B. Allen, T. Austin, N. Forrester, R. Goldsborough, M. Purcell, and R. Stokey, "Hunting for mines with REMUS: a high performance, affordable, free swimming underwater robot," in *OCEANS 2001 MTS/IEEE Conference and Exhibition*, 2001, vol. 1, pp. 117–122.

[122] REMUS. (n.d.). Oceanographic Systems Lab, Woods Hole Oceanographic Institution. [Online]. Available: http://www.whoi.edu/main/remus. Accessed Nov. 29, 2016.

[123] Mine Countermeasure Applications. (n.d.). [Online]. Available: http://www.hydroid.com/product-applications/12/mine-countermeasures. Accessed Nov. 29, 2016.

[124] D. Horner, A. Healey, and S. Kragelund, "AUV experiments in obstacle avoidance," in *OCEANS 2005 MTS/IEEE Conference and Exhibition*, 2005, vol. 2, pp. 1464–1470.

[125] D. Horner and O. Yakimenko, "Recent developments for an obstacle avoidance system for a small AUV," *IFAC Proceedings Volumes*, vol. 40, no. 17, pp. 19–25, 2007.

[126] D. Horner, N. McChesney, T. Masek, and S. Kragelund, "3D reconstruction with an AUV mounted forward-looking sonar," in *Proceedings of the International Symposium on Unmanned Untethered Submersible Technology (UUST09)*, Durham, NH, 2009.

[127] D. Sgarioto, "Control system design and development for the REMUS autonomous underwater vehicle," Defence Technology Agency, Auckland, New Zealand, Tech. Rep. DTA Report 240, May 2007.

[128] Beta distribution. (n.d.). MathWorks. [Online]. Available: https://www.mathworks.com/help/stats/beta-distribution.html. Accessed Nov. 29, 2016.

[129] A. E. Bryson, *Applied Optimal Control: Optimization, Estimation and Control*. Washington, DC: Hemisphere Pub. Corp., 1975.

[130] T. L. Vincent and W. J. Grantham, *Nonlinear and Optimal Control Systems*, 1st ed. New York, NY: John Wiley & Sons, Inc., 1999.

[131] A. L. Peressini, F. E. Sullivan, and J. J. J. Uhl, *The Mathematics of Nonlinear Programming*. New York, NY: Springer, June 1993.

[132] T. Eiter and H. Mannila, "Computing discrete Fréchet distance," Technische Universität Wien, Vienna, Austria, Tech. Rep. CD-TR 94/64, 1994, accessed Nov. 29, 2016. Available: http://www.kr.tuwien.ac.at/staff/eiter/et-archive/cdtr9464.pdf

[133] H. Alt and L. Scharf, "Computing the Hausdorff distance between curved objects," *International Journal of Computational Geometry & Applications*, vol. 18, no. 4, pp. 307–320, 2008.

[134] V. Ablavsky and M. Snorrason, "Optimal search for a moving target - A geometric approach," in *AIAA Guidance, Navigation, and Control (GNC) Conference*, 2000.

[135] M. Dille and S. Singh, "Efficient aerial coverage search in road networks," in *AIAA Guidance, Navigation, and Control (GNC) Conference*, 2013.

[136] A. Sriraman and M. Bays, "Efficient reacquire and identify path planning over large areas," in *Oceans 2014 - St. John's*, 2014, pp. 1–7.

[137] J. Haugen, "Guidance algorithms for planar path-based motion control scenarios," Masters, Dept. of. Eng. Cybern., Norwegian University of Science and Technology, Trondheim, Norway, 2010.

[138] E. Galceran and M. Carreras, "A survey on coverage path planning for robotics," *Robotics and Autonomous Systems*, vol. 61, no. 12, pp. 1258–1276, 2013.

[139] P. Cheng, J. Keller, and V. Kumar, "Time-optimal UAV trajectory planning for 3D urban structure coverage," in *2008 IEEE/RSJ International Conference on Intelligent Robots and Systems (IROS)*, 2008, pp. 2750–2757.

[140] J. R. Stack and C. M. Smith, "Combining random and data-driven coverage planning for underwater mine detection," in *OCEANS 2003 MTS/IEEE Conference and Exhibition*, 2003, vol. 5, pp. 2463–2468.

[141] I. M. Ross, "A beginner's guide to DIDO: A MATLAB application package for solving optimal control problems," Elissar (www.elissarglobal.com), Carmel, CA, Tech. Rep. TR-711, 2007.

[142] E. M. Arkin, S. P. Fekete, and J. S. B. Mitchell, "Approximation algorithms for lawn mowing and milling," *Computational Geometry*, vol. 17, no. 1, pp. 25–50, Oct. 2000.

[143] P.-M. Hsu and C.-L. Lin, "Optimal planner for lawn mowers," in *IEEE 9th International Conference on Cybernetic Intelligent Systems (CIS)*, 2010, pp. 1–7.

[144] G. T. Huntington, D. Benson, A. V. Rao, and others, "A comparison of accuracy and computational efficiency of three pseudospectral methods," in *AIAA Guidance, Navigation, and Control (GNC) Conference*, 2007.

[145] L. Trefethen, *Spectral Methods in MATLAB* (Software, Environments and Tools). Philadelphia, PA: Society for Industrial and Applied Mathematics, 2000.

[146] Intel® Xeon® processor specifications. (n.d.). Intel. Santa Clara, CA. [Online]. Available: http://ark.intel.com/products/81060/Intel-Xeon-Processor-E5-2698-v3-40M-Cache-2_30-GHz. Accessed Nov. 29, 2016.

[147] H. Weinberg, "Generic Sonar Model," in *OCEANS 1982 - MTS/IEEE Washington*, 1982, pp. 201–205.

[148] Home - High Performance Computing - NPS Wiki. [Online]. Available: https://wiki.nps.edu/pages/viewpage.action?title=Home&spaceKey=HPC. Accessed Nov. 29, 2016.

[149] S. B. Josselyn and I. M. Ross, "Sensitivity analysis for rapid prototyping of entry vehicles," *Journal of Spacecraft and Rockets*, vol. 43, no. 4, pp. 836–841, 2006.

[150] Slurm workload manager. (n.d.). SchedMD. California. [Online]. Available: http://slurm.schedmd.com/overview.html. Accessed Nov. 29, 2016.

Initial Distribution List

1. Defense Technical Information Center
   Ft. Belvoir, Virginia

2. Dudley Knox Library
   Naval Postgraduate School
   Monterey, California